DISSERTATION

MORPHOLOGY AND ELECTRONIC STRUCTURE OF AROMATIC MOLECULES ADSORBED ON Au(111)

Submitted By
C. Brian France
Department of Chemistry

In Partial fulfillment of the requirements
for the Degree of Doctor of Philosophy
Colorado State University
Fort Collins, Colorado
Fall 2003

COLORADO STATE UNIVERSITY

August 11, 2003

WE HEREBY RECOMMEND THAT THE DISSERTATION PREPARED UNDER OUR SUPERVISION BY C. BRIAN FRANCE ENTITLED MORPHOLOGY AND ELECTRONIC STRUCTURE OF AROMATIC MOLECULES ADSORBED ON Au(111) BE ACCEPTED AS FULLFILING IN PART REQUIREMENTS FOR THE DEGREE OF DOCTOR OF PHILOSOPHY.

Committee on Graduate Work

Debbie Crans

Peter Dorhout

Michael Elliott

Carl Wilmsen

Adviser – Bruce Parkinson

Department Head

ABSTRACT OF DISSERTATION

MORPHOLOGY AND ELECTRONIC STRUCTURE OF AROMATIC MOLECULES ADSORBED ON Au(111)

Organic semiconducting thin films of pentacene, *p*-sexiphenyl and naphtho[2,3-a]pyrene were characterized on a Au(111) substrate. The morphology of the organic adsorbates on Au(111) have been investigated with STM. Coverage-dependent structures have been found with pentacene on Au(111). Four different low coverage structures as well as multiple one-dimensional rows, with coverage-dependent separation, have been imaged. Annealed pentacene films have revealed the monolayer structure. Complex multilayer polymorphs have also been observed and modeled in high-coverage films. An unusual alternating *p*-sexiphenyl domain has been observed with a herringbone unit cell similar to that found in the bulk. High-resolution images have shown a single molecular enantiomer making up chiral domains of naphtho[2,3-a]pyrene on Au(111).

The binding environments of the organic semiconductor molecules on Au(111) have been determined utilizing temperature programmed desorption. Multiple binding energy environments have been observed for several of the organic films. These differing environments have been attributed to the stronger interactions of the molecules in direct contact with the Au(111) compared with the molecules in the multilayer.

XPS and UPS have been used to characterize the energetics of the immediate interface at the metal/organic heterojunction. XPS has been used to ensure no chemical reaction of the organic on the metal. UPS He I has measured the work function shift of the interface to determine the magnitude of the interface dipole. Large dipoles of up to 1eV have been determined at these interfaces. These work function shifts are completed after deposition of approximately one monolayer. He II spectra have been used to monitor the growth of valence states in the organic with increasing film thickness.

C. Brian France
Department of Chemistry
Colorado State University
Fort Collins, CO 80523
Fall 2003

Acknowledgments

I would like to offer a special thanks to all of the support given to me by my family during my graduate studies. In particular, I would like to thank my wife, Melissa, whose patience, emotional and financial support made it possible for me to continue my education. Special thanks to my parents, Richard and Betty, for believing in me and showing me how to reach my goals. John and Jane Bonfoey are acknowledged for all of their assistance, helpful guidance and willingness to go on long bicycle rides.

P. G. Schroeder is acknowledged for his assistance with the UHV system, moving to the new lab, as well as his team work with the pentacene / gold system. J. C. Forsythe is acknowledged for his work on the instrumentation of the temperature programmed desorption. My advisor, Professor Bruce A. Parkinson is thanked for his guidance and leadership pertaining to this work. The reset of the Parkinson group is acknowledged for their useful thoughts and ideas, conversations and friendship.

I would also like to acknowledge my Chemistry Professers at University of Southern Colorado, who encouraged my interest in Chemistry and have offered unconditional support as a student and while I continue with my career. They are the best teachers I have encountered in my educational career. In particular I would like to thank my undergraduate advisor Kristina Proctor. Furthermore, I would like to acknowledge C. M. Elliott for allowing me work in his lab prior to the start of the graduate program.

Table of Contents

Index of Figures

Index of Tables

List of Acronyms

AES: Auger Electron Spectroscopy

AFM: Atomic Force Microscopy

Alq_3: *tris*-(8-hydroxyquinoline) aluminum

BN: Boron Nitride

22BPY: 2,2'-bipryidine

eD: Interface Dipole

E_{be}: Electron Injection Barrier

E_{bg}: Band Gap Energy

E_{bh}: Hole Injection Barrier

E_F: Fermi Level Energy

E_{ion}: Ionization Energy

E_{vac}: Vacuum Level Energy

FEF: Field Effect Transistor

FIM: Field Ion Microscopy

FWHM: Full Width Half Maximum

HBEC: High Binding Energy Cutoff

HOMO: Highest Occupied Molecular Orbital

IR: Infrared

ITO: Indium Tin Oxide

LED: Light Emitting Diode

LEED: Low Energy Electron Diffraction

LUMO: Lowest Unoccupied Molecular Orbital

MLE: Monolayer Equivalent

MOSFET: Metal Oxide Semiconductor Field Effect Transistor

NP: Naphtho[2,3-a]pyrene

OFET: Organic Field Effect Transistor

OLED: Organic Light Emitting Device

OTFT: Organic Thin Film Transistor

PES: Photoemission Spectroscopy

Acronyms *continued...*

PTCDA: 3,4,9,10-Perylenetetracarboxylic acid dianhydride

p-6p: p-Sexiphenyl

QCM: Quartz Crystal Microbalance

RGA: Residual Gas Analysis

SAM: Scanning Auger Microscopy

SEM: Secondary Electron Microscopy

SHG: Second Harmonic Generation

SMW: Single Molecular Width

STM: Scanning Tunneling Microscopy

TPD: Temperature Programmed Desorption

UHV: Ultra-High Vacuum

UPS: Ultraviolet Photoelectron Spectroscopy

VT-STM: Variable Temperature Scanning Tunneling Microscopy

WSP: Widely Spaced Periodic

XPS: X-ray Photoelectron Spectroscopy

ϕ: Work Function

Objectives:

The continuing development of devices and technologies that utilized organic semiconducting materials has reached a point that some commercially available products are on the market. These organic materials are being used in organic light emitting devices (OLED) and organic thin film transistors (OTFT). It can be envisioned that continued development of these organic devices would lead to the production of large area flexible displays, inexpensive displays for hand held and house hold appliances, so called 'smart' cards and inexpensive memory and logic elements. While these are exciting prospects, unresolved aspects of the devices remain that need to be understood to optimize there functionality.

One of the common interfaces used in OLED and OTFT technology is the contact of metals to the organic semiconductor materials.[*1, 2*] In OTFT devices, two of these interfaces are present in the device. Recent studies by Baldo and Forrest have shown that charge transport in organic semiconductors is influenced by the localization of electronic states in the metal / organic interface.[*3*] A new model has been proposed to fit experimental measurements in which hopping through interface states is the rate limiting step in charge injection. This work demonstrates the significance of this interface and the importance in understanding its fundamental properties.

Gold contacts in particular are commonly used in these devices because of its chemical stability, availability and ease of use. A model gold surface has been used in these experiments to simulate a gold contact. A Au(111) film has been grown on mica to produce a flat clean surface that is congenial for analysis. We have worked toward understanding the morphological, chemical, and electronic properties of several gold / organic semiconductor interfaces.

Three different organic semiconductor materials have been investigated. Each of them has application in different devices. Pentacene is an organic thin film transistor material with a high charge carrier mobility.[2] *p*-Sexiphenyl has found use as a transport material in organic light emitting devices.[*4-6*] Naphtho[2,3-a]pyrene is a molecule with similar electronic characteristics, however it has a low degree of symmetry and will become two-dimensionally chiral when adsorbed onto a surface. This system in particular is of fundamental interest for sensor and catalysis applications.

In this research, we have studied the morphology of sub-monolayer and monolayer organic films using scanning tunneling microscopy (STM). Coverage-dependent studies have been performed to understand the growth and substrate-adsorbate interactions. We have attempted to correlate the observed structures with the electronic properties of the thin film. These electronic characteristics have been measured with photoemission spectroscopy. X-ray photoelectron spectroscopy has measured core level

states of the interface while ultraviolet photoelectron spectroscopy determines the valence states, including the workfunction of the interface. The binding environment of the organic materials has also be determined utilizing temperature programmed desorption. The culmination of these experiments has shed some light on the fact that these interfaces are more complex than first anticipated and contain a rich amount of structural diversity.

References:

[1] C. W. Tang, S. A. VanSlyke, Appl. Phys. Lett. **51**, 913-915 (1987).

[2] C. D. Dimitrakopoulos, S. Purushothaman, J. Kymissis, A. Callegari, J. M. Shaw, Science **283**, 822 (1999).

[3] M. A. Baldo, S. R. Forrest, Phys. Rev. B **64**, 85201 (2001).

[4] H. Yanagi, T. Ohara, T. Morikawa, Adv. Mater. **13**, 1452 (2001).

[5] H. E. Katz, Z. Bao, J. Phys. Chem. B **104**, 671 (2000).

[6] E. Ito, H. Oji, M. Furuta, H. Ishii, K. Oichi, Y. Ouchi, K. Seki, Synth. Met. **101**, 654 (1999).

Chapter 1: Background to Organic-Based Electronic Materials

1.1 Organic Electronic Materials and Devices

Organic electronic materials have been investigated for use in light emitting diodes (LEDs) and field effect transistors (FEFs). Traditionally, these devices have been the domian of silicon and III-V based inorganic semiconductors. However, the goal of low cost fabrication through straightforward processing and the infinite number of usable compounds for color and energy level variation are some advantages to organic based devices. Organic light emitting devices (OLEDs) allow a wider viewing angle, sharper contrast, faster pixel response time and greater potential for scaling up to larger displays compared to currently used liquid crystal displays. Several commercially available devices utilizing OLED display technology are now on the market, these include automobile stereos consoles and cellular phones displays. Organic field effect transistors

(OFETs) have demonstrated the potential to be used as pixel drivers for OLEDs, organic solar cells and so called "smart" cards.

Electroluminescence of aromatic molecules has been known for some time. Single crystals of anthracene or crystals doped with tetracene have produced light under an electrical bias that could be seen in a dimly lit room.[*1*] In the case of the anthracene crystal, the luminescence was from of anthracene fluorescence; for the tetracene doped crystal, it was that of tetracene. The efficiency of these early devices was quite poor and electroluminescence required the application of over 400V. Efficiencies did not improve much until the development of the bilayer electroluminescent cell by Tang and VanSlyke.[*2*] This cell used an organic heterojunction within the device that was produced by interfacing a diamine hole transport layer and an electroluminescent electron transport layer, *tris*-(8-hydroxyquinoline) aluminum (Alq_3). Previous attempts to make an electroluminescent cell only used a single organic layer and the light output was low; the use of the organic heterojuction was a significant step forward.

A diagram of the bilayer device, as developed by Tang and VanSlyke [*2*], as well as the structure of the organic materials used for the hetrojunction are presented in figure 1.1.A. In this device, indium tin oixide (ITO) coated glass was utilized as a substrate as well as the anode. A 750Å thick layer of the diamine (organic hole transport material) followed by 600Å of luminescent Alq_3 was vapor deposited onto the ITO substrate,

forming the organic heterojunction. The cathode was a 10:1 mixture of magnesium and silver deposited simultaneously from two separate evaporation sources. This alloy formed a low workfunction cathode, providing electrical contact for the injection of electrons into the electroluminescent material. This basic design has undergone numerous modifications and additions since its initial development including the use of different electron transport/luminescent materials[*3-8*], stacking multiple layers of organic materials for improved efficiency and stability[*9-16*], doping various electroluminescent dyes into the electron transport layer[*17-23*], and varying the hole transport material[*24-30*]. The literature cited above is but a small sample of the numerous studies that have been performed.

An energy diagram of the bilayer OLED device is presented in figure 1.1.B. In this device, electrons are injected into the organic electroluminescent layer through the low workfunction cathode; shown on the left of the figure. Under an applied bias these electrons migrate through the layer towards the organic heterojunction, at which point they encounter an interfacial barrier. This barrier reduces electron transport at the organic interface because of the energetically up hill process of passing from the lowest unoccupied molecular orbital (LUMO) of the electroluminescent material to the higher energy LUMO of the hole transport material. At the same time, holes (electron vacancies) are injected into the diamine or hole transport layer from the high

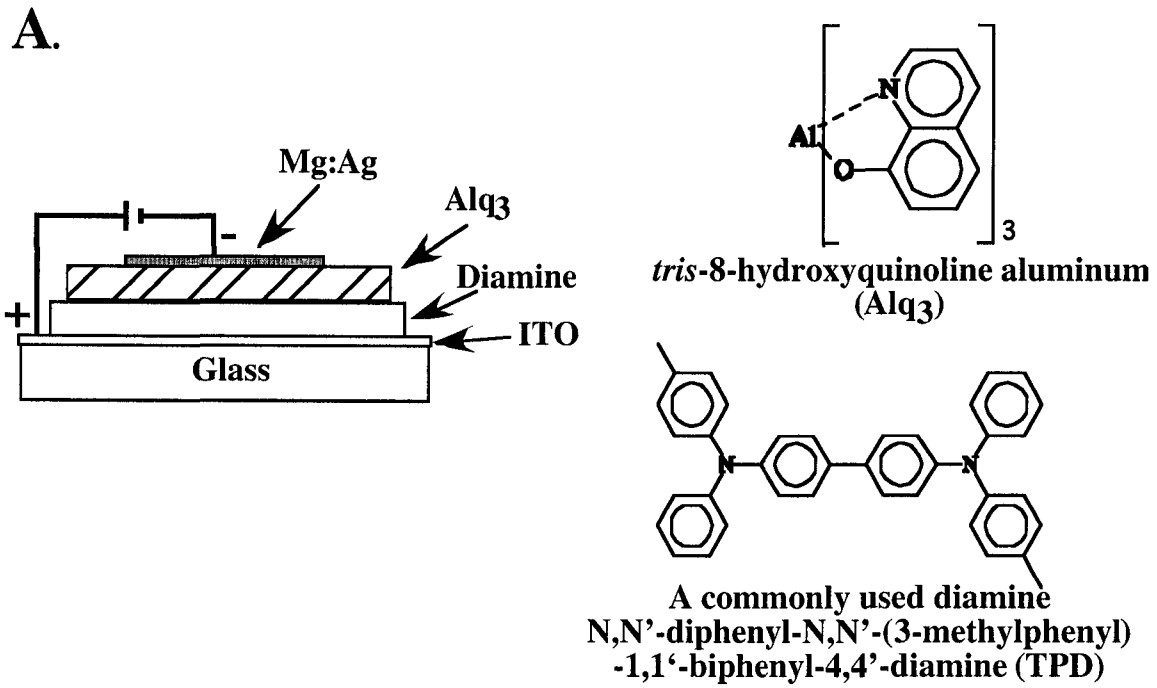

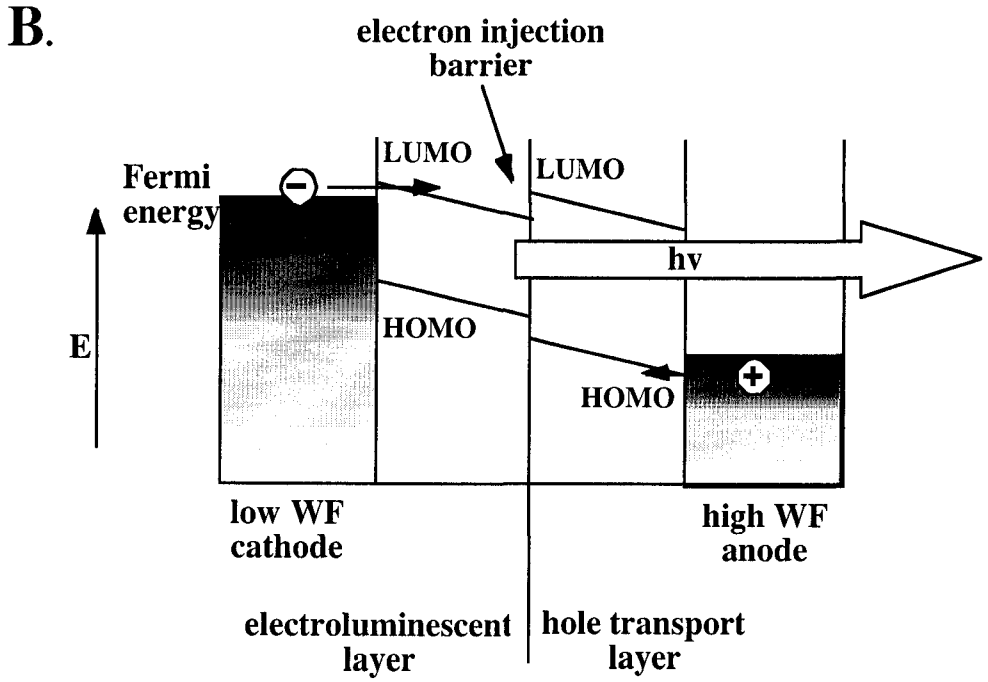

Figure 1.1: (A). Configuration of the bilayer electroluminescent cell and molecules used by Tang and VanSlyke (1987). (B). Energy level diagram of a simple organic bilayer organic light emitting device (OLED).

workfunction anode; shown on the right of the image. The holes are drawn towards the organic bilayer and can cross the heterojunction to the electroluminescent layer without a barrier. Thus the electrons and holes are confined within the electroluminescent material increasing the probability of producing an electronically excited molecule. The relaxation of the electron-hole pair in a molecule from the LUMO to the highest occupied molecular orbital (HOMO) produces a photon of light with a characteristic wavelength of the luminescent material. The simple use of an organic bilayer to impose an electron injection barrier significantly increased the radiative recombination in the organic based LEDs, compared to the single layer devices of Pope and coworkers.

Another device for which organic semiconducting materials are being developed, is the organic thin film transistor (OTFT).[*31-39*] The basic structure of this device is similar to the metal oxide field effect transistor (MOSFET), with the conductive channel produced in the organic semiconducting material.[*40*] A simple OTFT device is shown in figure 1.2.A where an n-type Si gate electrode with a blocking oxide layer is used as a substrate. The organic semiconductor material is either vapor deposited or spin coated onto the oxide. Electrical contact is then achieved through the deposition of gold source and drain contacts. The source contact has a positive bias applied while the drain is negative, thus electrons flow from the source to the drain. However, control over the amount of current flow is achieved by the regulation of the bias on the gate electrode.

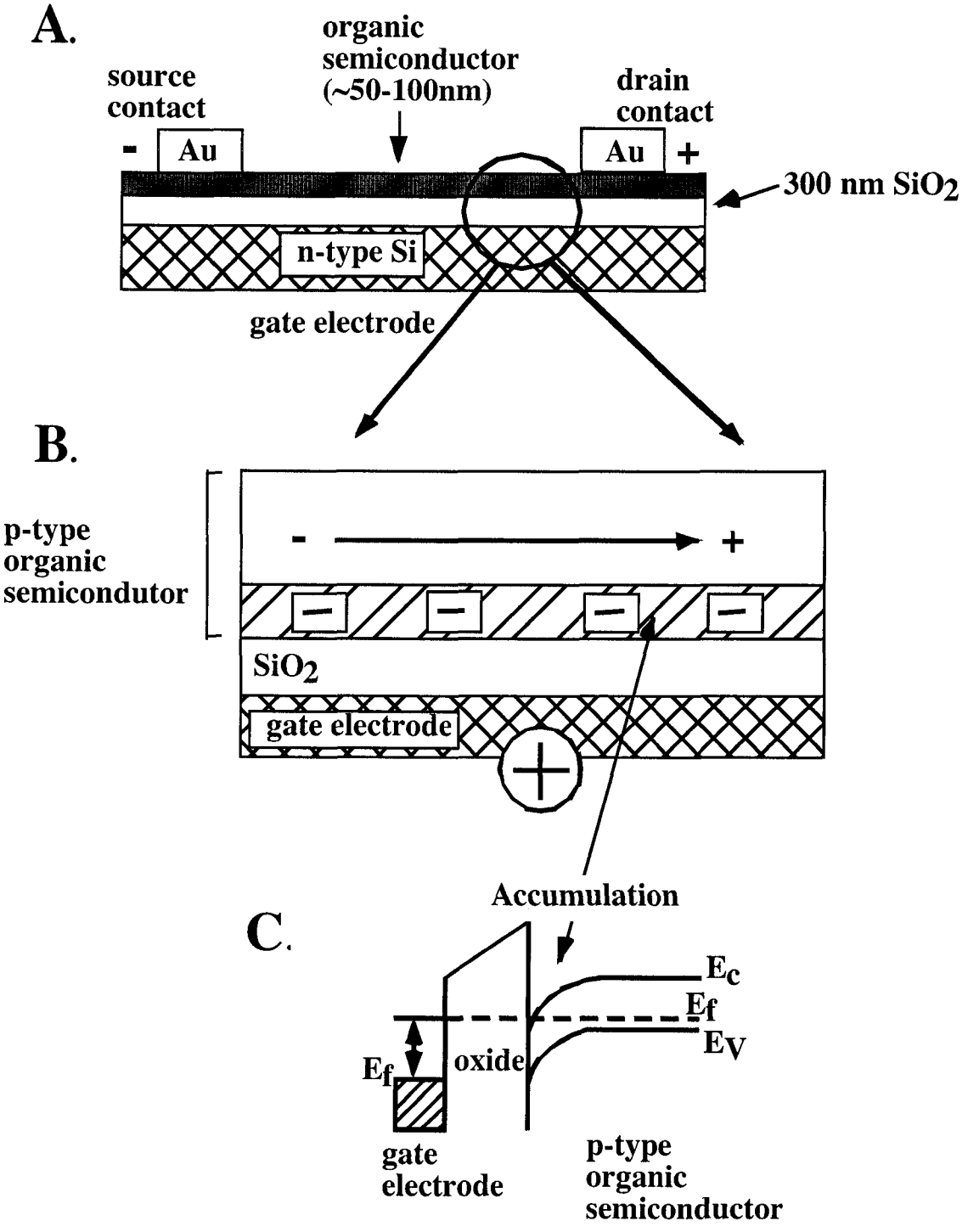

Figure 1.2: (A) A simple schematic of an organic thin film transistor (OTFT). (B) A diagram of an OTFT in operation where a conductive channel is formed in a p-type organic material and electrons flow from left to right. (C) Energy level diagram of the formation of an accumulation layer at the oxide/organic semiconductor interface.

The mechanism by which these OTFT devices work is demonstrated in figure 1.2.B. When a sufficiently positive bias is applied to the gate electrode, the p-type organic semiconducting material has electrons accumulate at the interface of the oxide material.[*33*] This accumulation of charge produces a channel through which electrical current can migrate from the source to the drain contact. An energy level diagram of the organic material in accumulation at the oxide interface is presented in figure 1.2.C. The application of the positive potential on the gate electrode drives the conduction band edge down below the Fermi level energy. This causes an accumulation of electrons at the interface and the formation of a conducting channel. Varying the applied potential of the gate electrode can alter the amount of current that flows through the device. If the bias is not sufficient, no channel will be formed and the current will be drastically reduced. Application of a larger bias on the gate electrode will cause the accumulation layer to increase until current saturation is achieved. The interfaces between the source and drain contacts with the organic material are junctions that could affect the characteristics of the OTFT device. Further discussion of this interface will be presented in section 1.2.

Many different organic and organometallic materials have been investigated for use in OTFTs. A short list of those molecules studied include; thiophenes,[*31, 33, 39*] perylene direvatives,[*31*] oligophenyl compounds,[*32, 33*] phthalocyanine[*33, 35, 36*] and polyacene films[*33, 34, 36-38*]. The structures of many of these compounds and the

molecules studied in subsequent chapters are shown in figure 1.3. Each of these molecules is primarily composed of a delocalized π electron system. This feature of the molecules permits the materials to function as semiconductors. The ability of the molecules to support positive or negative carriers through their π system leads to the relatively high charge carrier mobilities of the film or single crystal. The poly-paraphenylenes have been demonstrated to be relatively efficient electron transport materials. Pentacene is an example of an organic thin film transistor material with a high field effect mobility for an organic crystals (0.6 $cm^2V^{-1}S^{-1}$).[*34*] Naphtho[2,3-a]pyrene has a similar aromatic electronic makeup with an interesting low degree of symmetry, such that the molecule becomes two-dimensionally chiral when adsorbed onto a surface. Further information concerning the application of these organic semiconductors will be included in future chapters.

1.2 Introduction to Organic Semiconductors and Interfaces

Investigations into the morphology and electronic properties of organic interfaces with metal substrates will ultimately lead to the understanding and thus development of better devices. Correlation of the electronic properties with physical structure will provide insight to the current-voltage behavior, charge injection characteristics, and efficiency of organic based devices.

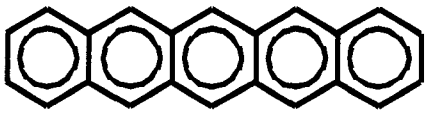

pentacene
thin film transistor material

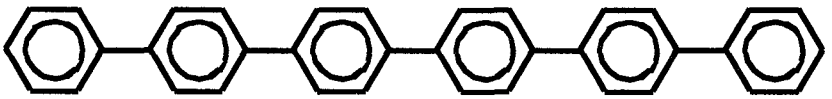

***p*-sexiphenyl**
luminescent / transport material

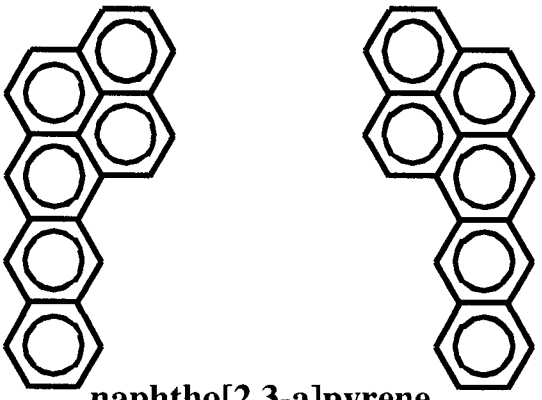

naphtho[2,3-a]pyrene
two dimensionally chiral material

Figure 1.3: Organic semiconducting materials examined in later chapters.

The electronic properties of conventional inorganic semiconductors are similar to organic materials, including junction offset characteristics and an increasing conductivity with temperature relationship.[*41*] The mechanism of conduction is different since a 'hopping' process between molecules takes place in the organic semiconductors. Since there are many similarities in band-like behavior between organic and inorganic systems, the concept of bands will be treated in a universal and traditional inorganic sense.

The Fermi level (E_F) is a reference energy that is relevant for both semiconductors and metals. The Fermi energy or Fermi level is the energy of the topmost filled state and is synonymous with the chemical potential of the electrons in the solid. It is defined as the energy where the probability of electron occupation is one half. The population probability P(E) of the energy levels is based on the Fermi-Dirac distribution, which is a version of the Bolzman equation that takes into account the Pauli exclusion principle.

$$P(E) = \frac{1}{1 + e^{(E-E_F)/kT}}$$

Since semiconductors have a band gap in which there exist no energy states between the conduction and valence bands, there is zero probability for an electron to exist at the Fermi level. In the case were there are negligible impurities in the semiconductor and it is in its intrinsic state, the Fermi level is defined as

$$E_F = \frac{E_C + E_V}{2} + \frac{3kT}{4}\ln\left(\frac{m_{dh}}{m_{de}M_c^{2/3}}\right)$$

where the energy level of the conduction and valence levels are E_c and E_v, m_{dh} and m_{de} are the effective masses of the holes and electrons, and M_c is the number of energy states in the conduction band.

To raise or lower the Fermi level in inorganic semiconductors, electrically active impurity atoms must be implanted or diffused into the intrinsic semiconductor. The position of the Fermi level will depend on the density and nature of these impurities, known as dopants. The Fermi level of the semiconductor is raised when electron donating dopants are added to the semiconductor. This is known as n-type (negative carrier) doping and an example is the addition of phosphorous to silicon. Lowering the Fermi level is achieved through the addition of electron acceptor dopants also known a p-type doping (positive carriers). The addition of gallium to silicon will function as an acceptor and thus p-type dopant.

Organic semiconductor materials can be doped in a similar way to inorganic semiconductors, through the implantation of dopants into the film or crystal.[*8, 42-44*] For example, the oxidation of Cs in an organic matrix will lead to the addition of an electron and thus function as an n-type dopant. Where as the reduction of molecular iodine in the organic material will remove and electron and serve as a p-type dopant.

While these dopants are difficult to introduce and control in organic materials because they are not rigidly held as in an inorganic material, their potential use and application in future devices is worthy of note. Future reference to the organic semiconductors will be in their intrinsic or non-doped state.

The interface between a semiconductor and a metal causes two important changes to take place in the semiconductor material; band bending and the formation of an interface dipole. Figure 1.4.A shows the energy levels of a metal and semiconductor that are separated and do not influence each other. The lack of any energetic shift is shown by the common vacuum level energy (E_{vac}). The energy difference between the vacuum level and Fermi level is known as the workfunction of the material As the two materials (with different Fermi levels (chemical potentials)) are brought into contact, there is a thermodynamic drive towards equilibration of their chemical potentials. The semiconductor has fewer conductive states than the metal, therefore the Fermi level of the semiconductor will decrease and become equivalent to the metal Fermi level. Since the metal Fermi level is more positive than that of the semiconductor, the positive charge carriers of the p-type semiconductor are pushed away from the surface into the bulk, causing a drop in the bulk Fermi energy of the semiconductor. This interface repulsion of the positive charge carriers is diagramed as a bending of the bands from the original energy levels at the surface to the new lowered Fermi level in the bulk. The

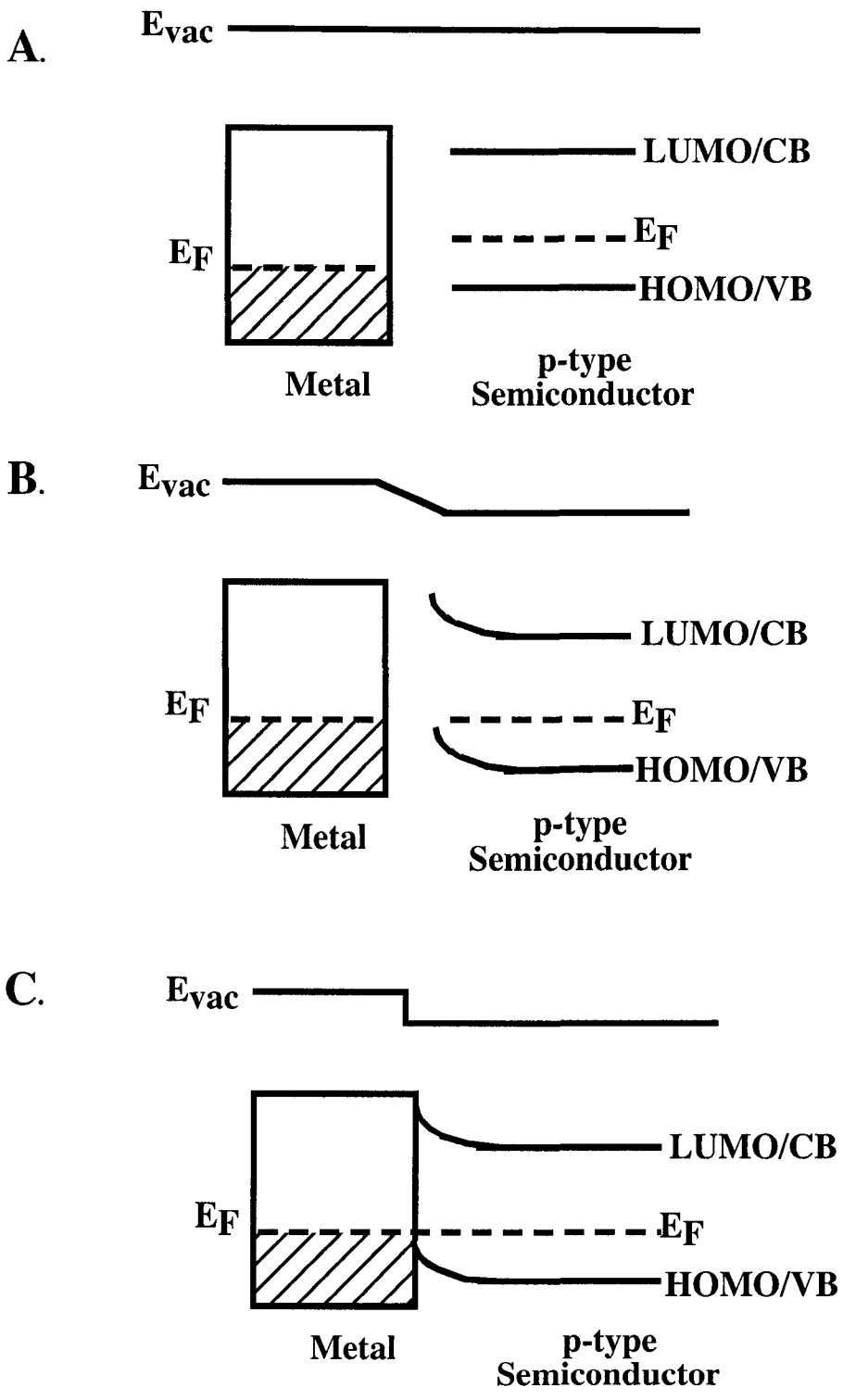

Figure 1.4: Diagram of the energetics of a metal interface with a semiconductor. (A). Infinite separation. (B). Equilibration of the Fermi levels. (C). Metal and semiconductor are brought into contact and a Schottky contact is produced.

workfunction of the semiconductor does not change during the formation of an interface thus the relative energy of the vacuum level shifts at the metal-semiconductor junction. This equilibration of chemical potentials (Fermi levels) is demonstrated in figure 1.4.B.

Upon contact between the metal and semiconductor, the Fermi energies have become completely equilibrated and the bending of the semiconductor energy states is at a maximum. The junction energetics and semiconductor band bending is diagramed in figure 1.4.C. The shift in the vacuum level in figure 1.4.C is shown as it is observed at an organic semiconductor-metal interface. As will be discussed in future chapters, the vacuum level of these junctions shifts within the thickness of the first monolayer at the interface. This is different than what is found in traditional inorganic semiconductor junctions. At these traditional interfaces the vacuum level shift would appear similar to the band bending that is shown in the valance and conduction bands. The nature and cause of this abrupt vacuum shift in the organic semiconductor / metal interface will be discussed below.

It is worth noting the electronic applications of these semiconductor-metal interfaces as rectifying or ohmic interfaces. The electronic properties of the interface depend on the original materials that make up the junction. Since all semiconductor devices require electrons to function, the understanding of these organic semiconductor-metal interfaces is fundamentally important. The interface diagramed in figure 1.4 is an

example of a rectifying contact as electron vacancies (holes) can move from the p-type semiconductor material to the metal without encountering an energy barrier, however a barrier is encountered moving holes from the metal to the semiconductor. This contact would be ohmic if the Fermi level was lower than the valence band of the semiconductor. Another ohmic contact would be formed when a metal and n-type semiconductor with workfunctions (ϕ) $\phi_m < \phi_s$ are brought into contact. Rectifying or Schottky barrier contacts are formed when $\phi_m > \phi_s$ in an n-type semiconductor / metal junction and $\phi_m < \phi_s$ with a p-type semiconductor.

The potential drop that occurs at the interface between the two materials is known as an interface dipole, which causes an abrupt shift in the vacuum level and is diagramed in figure 1.5.B (similar to figure 1.4). The magnitudes of interface dipoles that are formed at the junction can vary from 0 to larger than 1 eV. There are a number of factors that can cause the formation of an interface dipole and all of them are based on interface states. One mechanism for the formation of interface dipoles is through the donation of electron density from the organic material to the metal substrate, see figure 1.5.A. For the experiments described in later chapters, this explanation of interface dipole formation is the most relevant. This donation of electrons or electron density is also known as a quantum dipole. Typically, less than one electron equivalent per molecule is donated in the formation of the interface dipole. The deposition of organic molecules with a

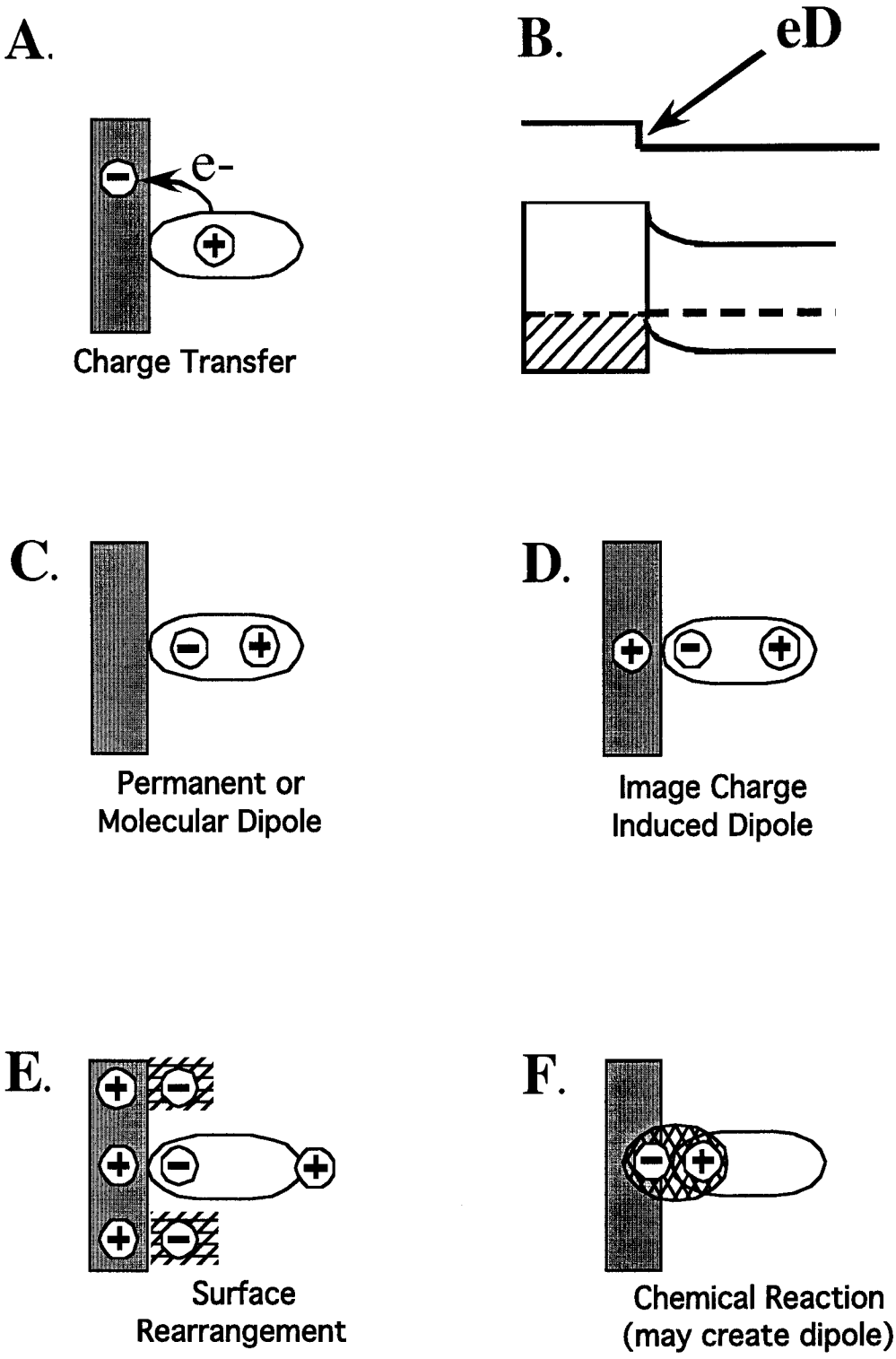

Figure 1.5: Factors that can influence the formation of an interface dipole in organic semiconductor materials. (B). The energy levels of an interface with a shift in the vacuum level that is indicative of an interface dipole.

permanent dipole can cause the formation of an interface dipole through the alignment of the polar molecules on the surface (figure 1.5.C). The formation of an induced dipole in the organic layer through charged species (dopants) in the substrate could also cause an interface dipole to form, depending on the dopant concentration at the surface. Similarly, an image charge in the substrate could be produced through the adsorption of polar or charged molecules (figure 1.5.D.). Adsorption of a large polarizable atom, such as a xenon atom on a metal surface, has been shown to cause a surface electronic rearrangement that will generate an interface dipole (figure 1.5.E.). The metal's electronic 'cloud' is pushed back into the surface by the repulsive interaction with the large adsorbate leaving a net positive charging effect on the vacuum side of the interface. The deposition of a reactive organic species onto a catalytic surface can cause a chemical reaction to take place. An interface dipole could be produced if the result of that reaction generated a polar product or transition state that meets one of the above requirements (figure 1.5.F.).

The importance of the states that produce interface dipoles have recently been indicated by Baldo and Forrest in their investigations of electronic contacts between metals and a organic semiconductor material (Alq_3).[*45*] They demonstrate that charge transport across the metal-to-organic interface is injection limited because of the presence of interfacial dipoles that induce intermediate states that participate in the injection

process. This interfacial dipole field broadens the energy distributions of the interface states and causes charge hopping from those states to be the rate-limiting step for charge injection into the organic material. Traditionally, thermionic emission over the interface barrier between the metal/semiconductor interface is used to describe transport characteristics. The current density, J, would be predicted by the Richardson-Schottky equation[*46*],

$$J = A^* T^2 \exp\left[-\left(\phi_B - \sqrt{qF/4\pi\varepsilon}\right)/k_B T\right]$$

where A^* is the Richardson constant, ϕ_B is the injection barrier, q is the electronic charge, F is the electric field, ε is the organic permittivity, k_B is Boltzmann's constant, and T is the temperature. However, the use of this equation to fit injection characteristics of the Alq_3 organic semiconductor device have shown that the Richardson constant prefactor, A^*, would have to be approximately 10 orders of magnitude lower than the value calculated for a free electron. Furthermore, the temperature dependence of these electronic interfaces has been shown not to follow Arrhenius behavior below room temperature [exp1/k_BT]. These deviations from the existing model indicate that a modification is needed to take into account the interface states that are important in the charge injection processes.

A model proposed by Baldo and Forrest,[*45*] has utilized a hopping mechanism for charge injection from a Gaussian distribution of interface states where the rate limiting step is the injection of charge from the interface states into the bulk of the organic material. The authors assume that hopping out of these interface sites limits the current density and that, at least initially, these transport sites are empty. The charge density per unit energy of the states near the metal is determined by Fermi-Dirac statistics and is given by,

$$n_I(E_I,E_F)=\frac{N_I/\sqrt{2\pi\sigma_I^2}}{1+\exp\left[(E_I-E_F)/k_BT\right]}\exp\left[-\frac{1}{2}\left(\frac{E_I}{\sigma_I}\right)^2\right]$$

were N_I and E_I are the density and energy of interfacial sites, E_F is the Fermi energy, N_I is the density of the interfacial sites, and σ_I is the energetic distribution of the sites in the first organic layer at the interface. The current density across the interface is then given by

$$J(E_F)=\frac{\bar{a}q}{\sqrt{2\pi\sigma_B^2}}\int_{-\infty}^{\infty}\int_{-\infty}^{\infty}n_I(E_I,E_F)R\left(E_B-E_I-\bar{a}qF\right)\times\exp\left[-\frac{1}{2}\left(\frac{E_B}{\sigma_B}\right)^2\right]dE_I dE_B$$

where $\bar{a}$ is the average intermolecular spacing, E_B is the energy of the charge in the bulk, and σ_B is the width of the bulk charge distribution. The rate of polaron hopping, R, is used as the corrected activation energy because the rate-limiting step is not the electron transfer between weakly interacting molecular orbitals, but the formation of and activated

complex that precedes the transfer. A polaron is a charge (positive or negative) that is coupled to a phonon within a lattice or molecule and is used for describing charge states in an organic film.

Experimental current voltage and temperature studies of the organic electronic devices, made using Alq_3, have been shown to more closely match this new model rather than the traditional Richardson-Schottky model. This demonstrates that the interfacial states produced by an interface dipole play an important role in the charge injection characteristics of organic based devices. Baldo and Forrest propose that the nature of the interface states arises from variations in the local dipole strength and orientation, which results from randomness in the interface morphology, and the localization of charge in molecular materials. The new model does demonstrate its usefulness in the studied Alq_3-metal interfaces, however the Richarson-Schottky equation may still be valid for other systems. The application of this model demonstrates the importance of the interface molecules in a metal-organic heterojunction and shows that the molecule's morphology and electronic characteristics are important to further understand the behavior of organic electronic devices.

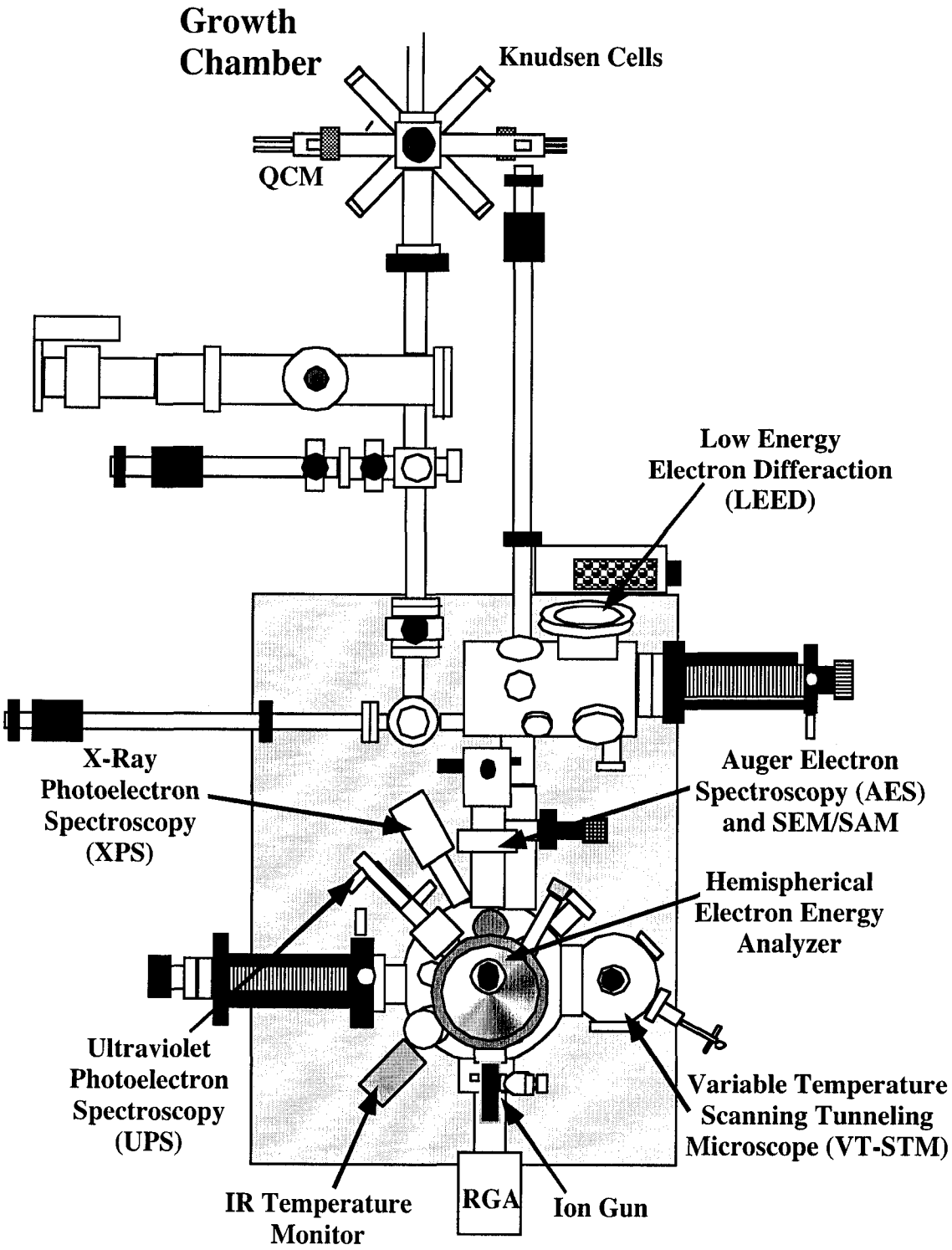

Figure 1.6: Omicron Multiprobe Ultra-high Vacuum system.

1.3 Experimental Procedure for Interface Electronic Characterization

All experiments were performed in a commercially available Omicron multiprobe ultra-high vacuum (UHV) analysis system; a diagram of the instrument is presented in figure 1.6. The techniques that are available for sample analysis include, X-ray photoelectron spectroscopy (XPS), ultraviolet photoelectron spectroscopy (UPS), Auger electron spectroscopy (AES) with secondary electron microscopy (SEM) and scanning Auger microscopy (SAM) capabilities, residual gas analysis (RGA) mass spectrometry which is utilized as a detector for temperature programmed desorption (TPD), an infrared temperature monitor, low energy electron diffraction (LEED), and a variable temperature scanning tunneling microscopy (VT-STM). The base pressure of the two UHV chambers that house all of the instrumental techniques is $\sim 1 \times 10^{-10}$ mbar.

A physical vapor deposition chamber ("growth chamber") was added onto the commercially available Omicron system allowing for the deposition of organics and metals under UHV conditions. These deposited films can then be transferred back into the analysis chambers through the entry system while maintaining a UHV environment. The base pressure of the deposition chamber is $\sim 1 \times 10^{-9}$ mbar. This beneficial design permits the *in situ* deposition and analysis of growth, morphology and electronic structure of ultra thin films. The chamber is equipped with a quartz crystal microbalance (QCM), a sample heater, and home built Knudsen-type deposition sources. A diagram of the

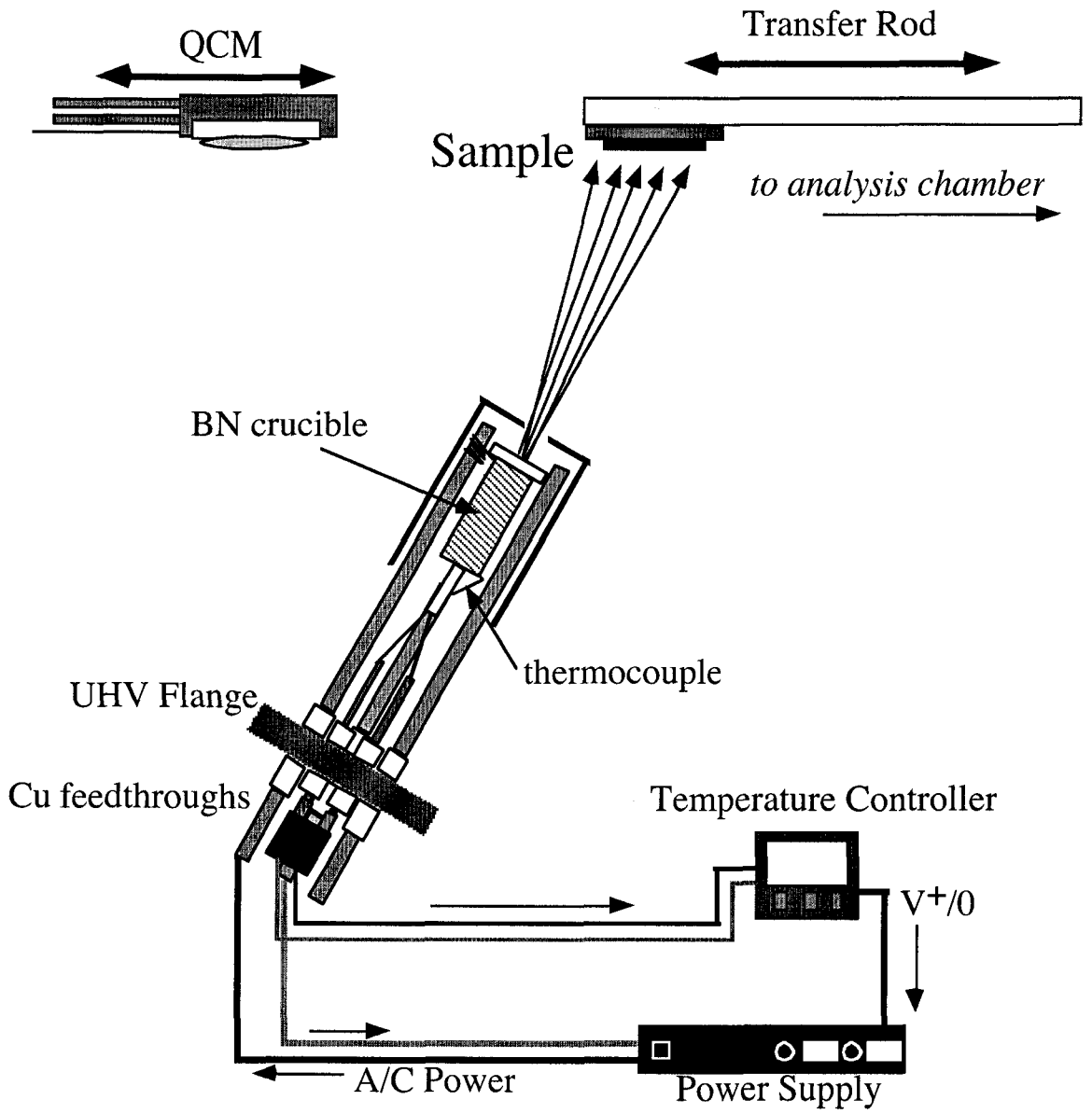

Figure 1.7: Physical vapor deposition setup. A boron nitride (BN) crucible is resistively heated, while the temperature is monitored with a K type thermocouple. A Eurotherm temperature controller allows for accurate control of the crucible temperature. A quartz crystal microbalance (QCM) is used to determine the deposition rate. The QCM is then moved out of the way and a sample is place in front of the Knudsen cell for the deposition of the desired film thickness.

deposition setup is presented in figure 1.7. The Knudsen cells utilize a boron nitride (BN) crucible for the physical vapor deposition of organic materials while a tungsten basket is used for the deposition of metals. The BN crucible is wrapped with a resistively heated wire that is connected to a copper UHV feed-through flange. A tungsten basket, for the deposition of metal, would be connected directly to the copper feed-through. A K-type thermocouple (Chromel/Alumel) is place inside a small hole on the backside of the crucible allowing for the determination of the deposition temperature. The temperature of the Knudsen cell is monitored by a Eurotherm temperature controller, which compares a set point temperature with the measured temperature. The power of the resistive heating is controlled through the Eurotherm management of a Sorensen power supply. The deposition is monitored with a quartz crystal microbalance that measures film thickness changes as small as an Ångstrom. Once a stable deposition rate is obtained, as measured with the QCM, the sample is placed in front of the heated Knuden cell for the desired amount of time. The sample can be deposited on while it is in either the magnetic transfer rod, room temperature sample, or in a resistive sample heater that is mounted on a linear motion translator. In all of the experiments performed with this deposition process, a rate of 4Å/min or less was established for the deposition of monolayer and sub-monolayer films.

The Au(111) surface can be prepared in one of two ways, a single crystal can be cleaved along the (111) plane or through the vacuum evaporation of a gold film on a suitable surface. Mica is the most commonly used surface for gold evaporation to produce a predominate (111) orientation.[*47*] This procedure produces a Au(111) surface without the cost or difficulty of purchasing or making a single crystal substrate, and is the substrate utilized in the experiments discussed in later chapters. The gold was treated in concentrated HNO_3 prior to placing it into a tungsten wire basket in the depostion chamber. A freshly cleaved mica surface is attached to a stainless steal sample holder with molybdenum clips (figure 1.8.A). The mica is then placed in the UHV chamber and heated of 24 hours at 300 °C. This allows any volatile contaminates to be removed from the surface before the deposition of the gold. While the mica sample is hot, the tungsten basket containing the gold is resistively heated to evaporate the gold onto the surface. The deposition slowly continues until an approximately 1 μm thick film is produced. The gold film is then cooled to room temperature and moved to the analysis chamber where it is further cleaned with repeated sputter (1 - 2 KeV Ar^+, 10 - 12 min) and anneal (300 – 350°C, for 30 – 60 min) cycles. The chemical purity of the gold film is established with XPS. LEED and STM are used to determine the presence of the characteristic $23 \times \sqrt{3}$ reconstruction. Figure 1.8.B shows a clean, well prepared, reconstructed Au(111) sample in a 200 × 200 nm STM image. The reconstruction is observed as raised (0.2 Å high)

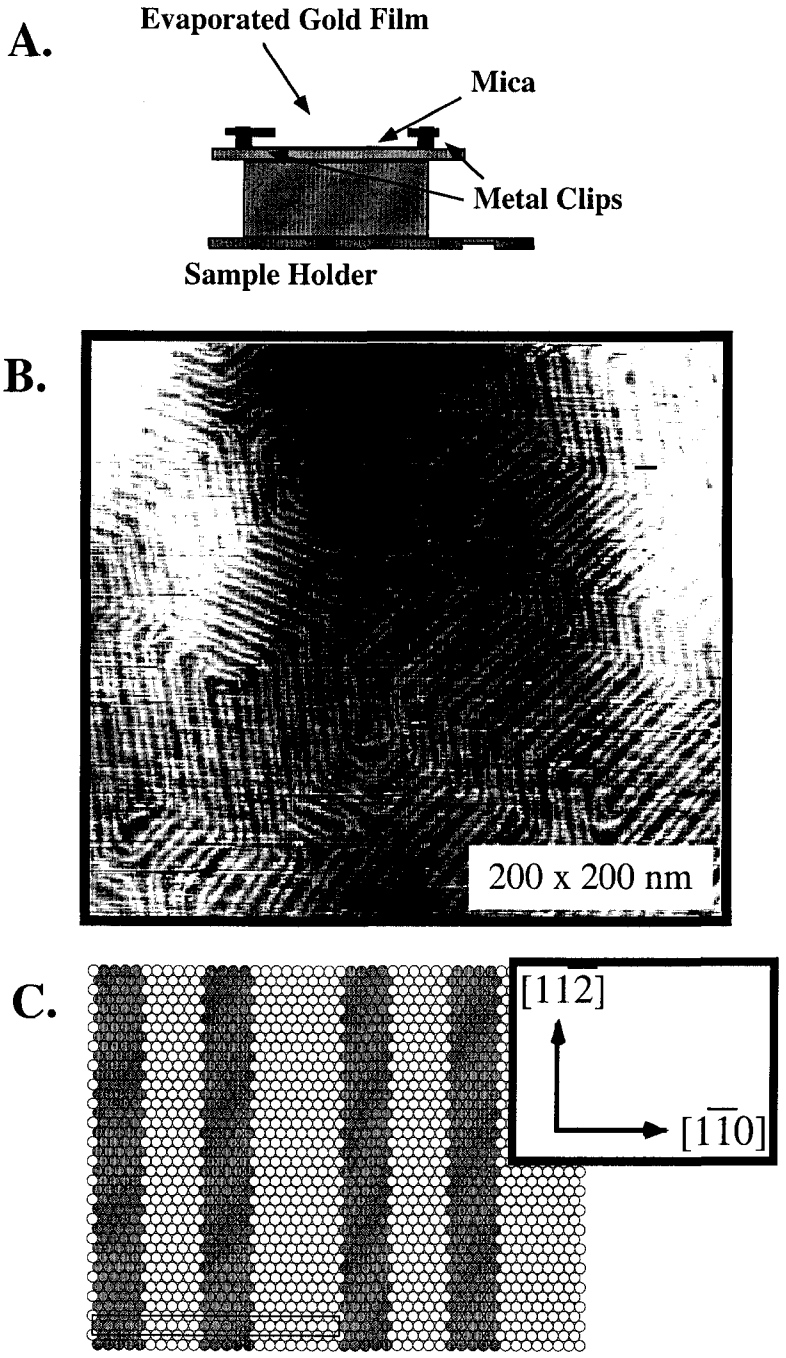

Figure 1.8: (A). A diagram of the Au(111) sample and sample plate. (B). An STM image of a clean reconstructed Au(111) surface. (C). A model of the Au(111) sample were the dark substrate atoms represent the elevated "stripes" of the reconstruction.

"stripes" across the surface. These elevated stripes are formed because there are 23 gold atoms on the surface for every 22 atoms in the bulk. This increase in the number of surface atoms causes a buckling and the formation of these stripes. The reconstruction traverses across the hexagonal Au(111) surface in one of the three equivalent $[1\bar{1}2]$ directions. The reconstructed Au(111) surface is modeled in figure 1.8.C, were the dark substrate atoms represent the elevated stripes. The direction vectors are included in the upper right hand of the model and a rectangle showing the reconstructed unit cell is presented in the lower left.

The roots of photoemission spectroscopy (PES) can be traced to Einstein's explanation of the photoelectric effect. The fundamental equation for photoemission spectroscopy is given by:

$$KE = h\nu - BE - \phi_s$$

were KE is the kinetic energy of the photoemitted electron, hυ is the energy of the light source, BE is the binding energy of the orbital from which the electron orginated and ϕ_s is the spectrometer work function. Core level orbitals have fairly fixed binding energies but they can vary over several electron volts due to changes in the sample composition and oxidation state. During a photoemission measurement, the kinetic energy of the emitted electron is monitored with a hemispherical electron energy analyzer. The use of a well-defined light source with a known energy allows for the determination of the binding

energy of the emitted electrons' orbital. The energy of the light source is chosen based on the desired orbitals to be investigated; core levels require x-rays (XPS) and ultraviolet for valence states (UPS). Figure 1.9 shows a representation of the energy wells of a carbon molecular adsorbate on a gold surface, the energy of the probing radiation determines the information that is obtained from the system. The x-ray source on the Omicron UHV system is a dual anode source where either the Mg Kα ($h\nu$ = 1254.6 eV) or Al Kα ($h\nu$ = 1486.6 eV) x-ray line sources are selected. A differentially pumped helium discharge lamp is used for the generation of ultraviolet light to probe the valance states of the sample surface. Two narrow line sources can be produced with this lamp, the He I line (21.22 eV) or He II radiation (40.81 eV). The He I line corresponds to the n = 1← 2 transition in the Lyman series for the helium atom and the He II light comes from the first line of the Lyman series for the He^+ ion. The spectrum produced by UPS (upper right of figure 1.9) probes the filled states from the Fermi level down into the valence states.

Now that the UHV environment of these experiments has been described as well as the deposition of organic molecules onto the prepared Au(111) films, the measurement of the interface energetics using photoemission spectroscopy can be discussed. The use of XPS and UPS to measure the electronic structure of an interface has been performed by other researchers to characterize the interface through the growth of many layers of

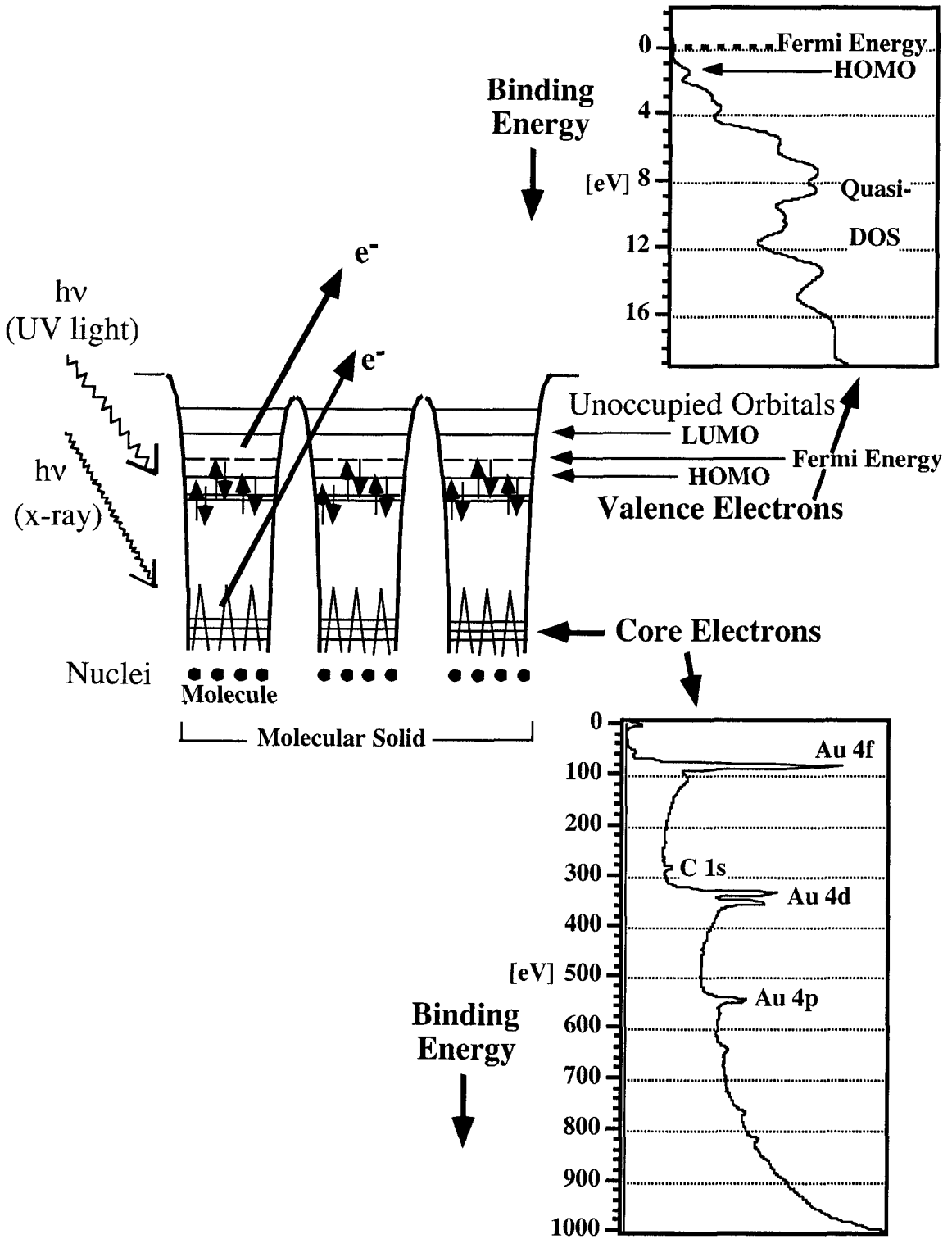

Figure 1.9: The potential well of a molecular adsorbate on a gold film. X-ray photoelectron spectroscopy is used to measure core orbital binding energies. Ultraviolet photoelectron spectroscopy probes the valence states of the interface yielding Quasi-density of states information.

organic materials.[*48-54*] The purpose of our studies is the determination of the morphology and electronic structure of the organic molecules at the interface of the organic and metal. Therefore, when a gold sample has been adequately cleaned, such that no contamination is measured with XPS and the correct workfunction is determined for a clean Au(111) film by UPS, the experiment is ready to proceed. The sample position of the manipulator arm is determined so that the maximum XPS signal is obtained then the UPS signal is optimized. These sample positions are noted so that after each deposition step, additional spectra are obtained from the same position. The Au(111) is moved to the deposition chamber where a very thin film of organic semiconductor (typically 0.1Å) is deposited on the substrate. The sample is then returned to the analysis chamber were XPS and UPS measurements are repeated. This process is repeated eight to ten times until the final thickness of the organic semiconductor film is about 50Å.

The evaluation of this data is performed using Igor Pro software (Wavemetrics Inc.). Core level electrons are monitored with XPS and used to follow the composition and energy levels of the interface with increasing coverage of the organic semiconductor. The XPS data is also used to insure the sample is contamination free, determine if any undesired chemical reactions are taking place and identify any charging that may be present.[*50*]

The work function (Φ) of the sample is measured with UPS and is determined from the He I spectrum. The high binding energy cutoff (E_{HBEC}) of the inelastically photoemitted electrons is subtracted from the source energy (21.22 eV)

$$\Phi = h\nu - E_{HBEC}$$

As the work function of the sample is measured throughout the experiment, the change in the work function ($\Delta\Phi$) between the cleaned Au(111) ($\Phi_{sub.}$) and that of the thick film (Φ_{film}) is determined.

$$\Delta\Phi = \Phi_{film} - \Phi_{sub.}$$

This work function shift is the result of the formation of an interface dipole.

A first approximation of the complete band line up can also be obtained from this experiment. However, as more measurements and additional analysis should be performed to obtain a more accurate determination of the complete interface entergetics, the reader should consult the references herein for more information. As the scope of our experiments is limited to the morphology and energetics of the immediate interface between the Au(111) and organic, the complete energetic alignment was not performed on all interfaces studied.

1.4 Binding Energy Determination of Adsorbates

Temperature programmed desorption (TPD) is a widely used technique to measure the binding energy between molecules and substrates.[*55-61*] The basic principle behind the technique is to heat up the sample and provide enough thermal energy to cause the desorption of adsorbates from the substrate or the decomposition of the molecule. The stronger the adsorbate binds to the surface, the more thermal energy will be required to desorb it. In our experiments, we are interested in determining if there is a measurable binding difference between the first monolayer of organic molecules, the molecules in contact with the metal surface, and that found in thicker layers. Due to the low evaporation temperatures and the stability of the molecules, we assume the molecules are desorbed intact. From these measurements we determine whether the molecules simply physisorb to the metal or if there is a stronger interaction due to electrostatic forces or covalent bonding.

A diagram of our custom designed and built TPD system that was added to the Omicron UHV system is depicted in figure 1.10. The sample is placed in a manipulator arm that can be resistively heated in UHV. A Eurotherm temperature controller controls the power supply that heats the sample. The sample temperature is monitored with an infrared thermopile detector through a ZnSe window that is mounted on the side of the UHV chamber. The benefit of using the IR thermocouple is to establish a more accurate

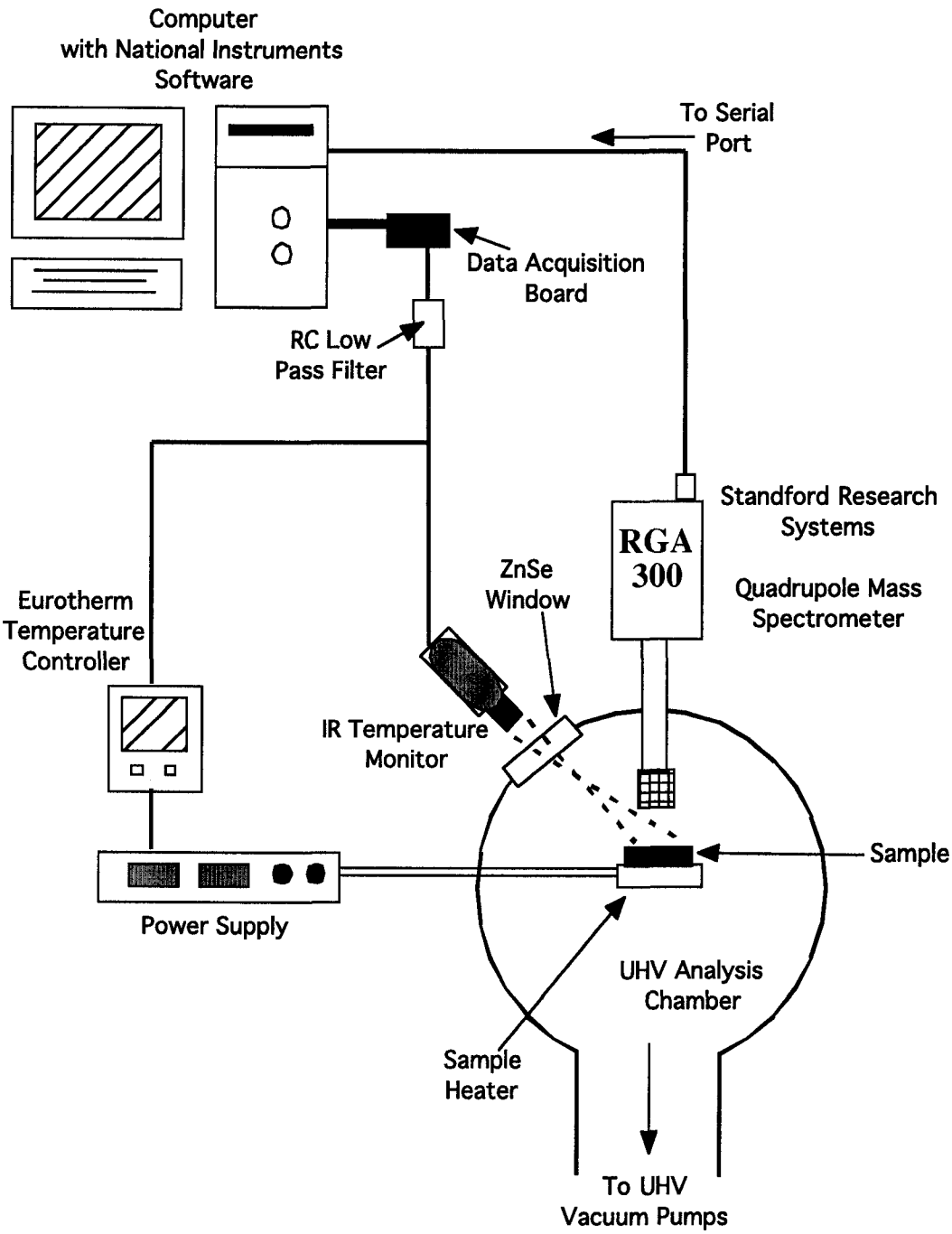

Figure 1.10: Diagram of the home build setup for temperature programmed desorption.

reading of the actual sample surface temperature. Whereas the use of a thermocouple attached to the manipulator will not provide an accurate reading of the surface temperature, as variation between sample plates will increase the error. The signal from the IR thermocouple is sent simultaneously to the Eurotherm controller as well as to a PC. In this configuration, the Eurotherm controller allows for a temperature program routine to be used to control the heating rate, range, and time of the sample. As the temperature of the sample is elevated the organic adsorbates will eventually desorb. A residual gas analyzer (Stanford Research Systems, RGA 300) quadrapole mass spectrometer monitors a pre-selected mass-to-charge (m/z) ratio related to a molecular fragment or parent peak. Since the molecules that desorb in these experiments are typically uncharged, an ionizing filament is positioned between the sample plate and the RGA. This filament will ionize and fragment the vaporized organic molecules allowing for the analysis of parent peak masses or fragments. The signal from the RGA is sent to the PC where the intensity of the selected m/z is recorded. The data collected at the computer is then plotted with the mass spectrometer counts on the y-axis and the temperature of the sample on the x-axis.

The peak position represents the mean vaporization temperature for a particular molecule or fragment. The existence of more than one binding environment on a sample is depicted by the formation of more than one peak in the TPD spectrum. The Redhead

formula[*58*] is utilized to determine the binding energy of the adsorbate based on its peak in the TPD spectrum. This equation is derived from an Arrhenius relationship where the rate of desorption from the surface may be written by:

$$N(t) = -d\sigma/dt = \nu_n \sigma^n \exp(-E/RT)$$

where n is the order of the desorption reaction, σ is the surface coverage (molecules/cm^2), ν_n is the rate constant and E is the activation energy of desorption. By utilizing a linear heating rate ($T = T_0 + \alpha t$) and assuming that E is independent of coverage (σ). Then for a first order desorption it can be derived[*58*] that the binding energy (BE) or energy of desorption is determined by:

$$BE = N_A kT\left[\ln\left(\frac{T\nu}{\alpha}\right) - 3.64\right]$$

where T is the temperature in Kelvin, N_A is Avogadro's number, k is the Boltzman constant, ν is a vibrational constant equal to 1×10^{13}, and α is the temperature ramp rate expressed in °C/second. Further experimental details and measurements can be found in chapter 3.

1.5 Procedures for Determination of Organic Morphology on Au(111)

To obtain a more through understanding of the immediate interface between organic semiconductors and Au(111), morphological characterizations must be

undertaken. Electronic barriers to charge transfer at the interface are not the only considerations since the structures and orientations of the molecules also influence the electronic properties of the interface. The influence of large interface dipoles on molecular arrangements is till an open question. As discussed above, the interface dipole has a large influence in the charge transfer capabilities of an interface, as charge migration through them is often the rate-limiting step.

Two techniques are available to on the UHV system to investigate the structure of the interface, low energy electron diffraction (LEED) and variable temperature scanning tunneling microscopy (VT-STM). LEED is commonly used on single crystal surfaces to probe the long-range order of the surface. This technique takes advantage of the interference phenomena of electrons scattered as they diffract off the crystal surface. Low energy electrons have a wavelength small enough to diffract off atomic layers and provide information about the top most layer of the surface. The de Broglie wavelength (λ) of the electron is determined by the velocity (v), mass of an electron (m_e) and Plank's constant (h); given by:

$$\lambda = \frac{h}{m_e v} = \frac{h}{\sqrt{2 m_e KE}}$$

which can be given as a function of the kinetic energy (KE) of the electron. As the electrons strike the sample surface they are reflected back and produce a pattern on a

phosphorescent screen. These points of constructive interference on the screen are known as the LEED pattern. Bragg's Law determines the relationship between the point on the screen and the surface structure,

$$n\lambda = d\sin\theta$$

where n is the diffraction order, λ is the wavelength of the electron, d is the lattice spacing and θ is the diffraction angle relative to the surface normal. LEED is very similar to the more commonly known x-ray diffraction techniques however the use of low energy electrons ensures that only the first surface most layers are analyzed. LEED has been used to characterize and determine the ordering of Au(111) films. The fact that our non-single crystal surface yielded LEED spots is attributable to the well-oriented films used in these experiments. An effort to analyze organic films on Au(111) with LEED was performed however they did not yield strong diffraction patterns. This could be caused by the lack of long-range order within the films or it could be that the electron beam was damaging the organic materials. These difficulties limited the use of LEED to the characterization of the freshly prepared, clean, Au(111) on mica substrates.

Binning and Rohrer recently invented the Scanning tunneling microscopy (STM) [*62*]. It has the capability to image a surface in real space while resolving individual atoms and has revolutionized surface science. The mechanism that STM uses to obtain such high resolution is electron tunneling. This quantum mechanical process requires

that the analyzed sample is conductive, thus allowing electrons to flow through the material while the current is monitored. An atomically (or nearly atomically) sharp tip is held within electron tunneling distance (several Å) of the sample surface. A bias is applied between the tip and sample, usually from a few tenths of a volt to several volts (see Figure 1.11.A). The applied bias polarity can be either positive or negative allowing electrons to tunnel to or from the sample, respectively. The sample-tip separation (s) is important because the tunneling current has been found to be exponentially dependant on the separation:

$$I \propto \exp(-2\kappa s)$$

The tunneling decay constant (κ) is given by:

$$\kappa = \frac{(2m\phi)^{\frac{1}{2}}}{\hbar}$$

where ϕ is the effective local potential barrier height, $\hbar$ is the Plank constant, and m is the effective mass of the tunneling electrons.

Moving the atomically sharp tip across the sample surface and monitoring the tunneling current allows for the production of high-resolution images. There are two common modes for monitoring the tunneling current in an STM: constant height mode and constant current mode. In the constant height mode the tip is set at a given height above the sample surface. The tip is then quickly raster scanned (through the use of a

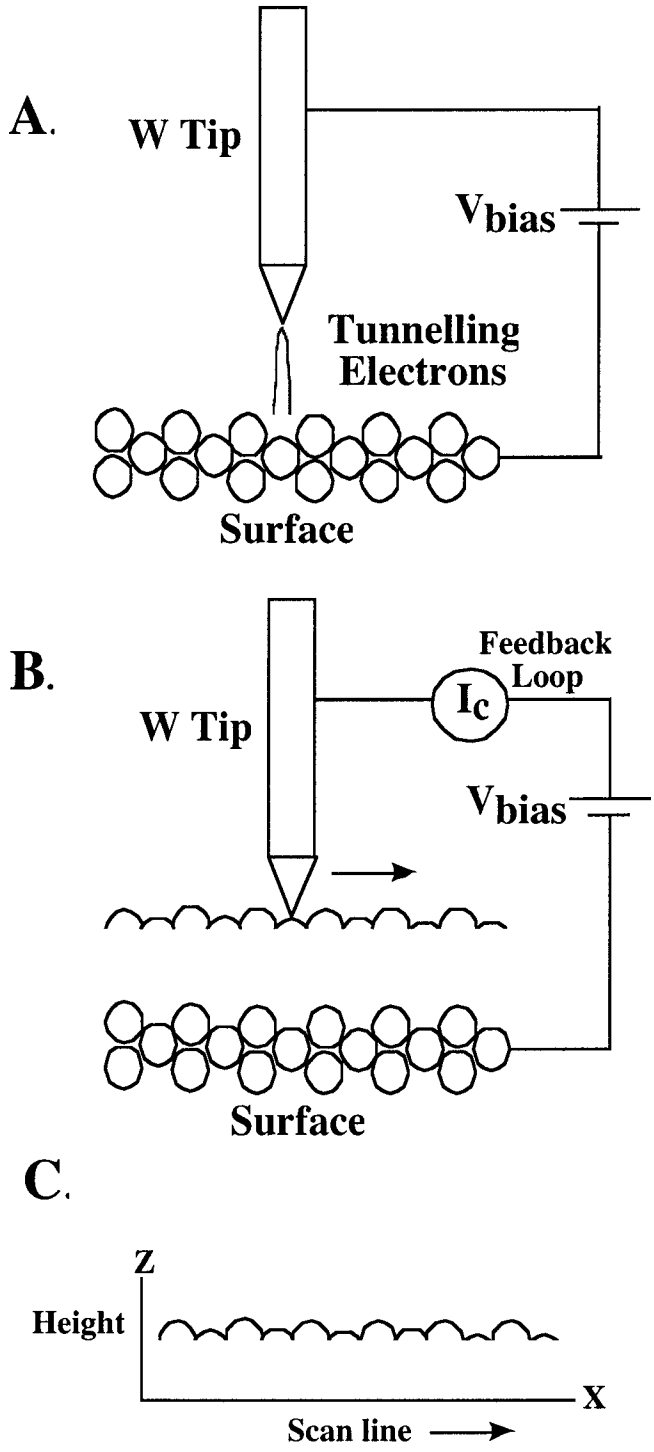

Figure 1.11: (A). Tunneling electrons allows for high-resolution STM imaging. (B) Constant current mode where the STM feedback mechanism maintains a constant current by altering the height of the tip. (C) Line scan of an image produced in constant current mode.

piezo-electric tube) over the sample surface. The modulation of the tunneling current, with the full sensitivity of the exponential dependence of the current on tip-sample spacing, then reflects the atomic-scale topography. Advantages to this method are that the speed at which an image can be produced is not limited by the STM feedback mechanism, provided the scan speed is not faster than the instrument preamplifier. Real-time video rates have been achieved with this technique to observe dynamic atomic-scale processes[*63*], however these advantages have not been utilized in our experiments due to instrumental and sample limitations. The analysis of a rough surface or a sample with large adsorbates using the constant height mode can cause the tip to crash into the surface thereby destroying the resolution of an atomically sharp tip.

STM images in future chapters were all obtained utilizing the first and most widely used mode of STM operation, constant current imaging mode. This mode involves the use of a feedback mechanism to maintain the tip-sample separation. The principle behind this process is presented in figure 1.11.B and C. The tip is brought within a fixed tunneling distance determined by the exponential tip-sample spacing, to obtain a predetermined tunneling current. As the tip is raster scanned across the sample surface, the feedback loop keeps the current constant by applying an appropriate voltage to the piezoelectric drive, maintaining the predetermined current setting (typically 0.01 – 5 nanoamperes) (Figure 1.11.B). The signal from the feedback loop is then recorded as

the atomic topography and is often referred to as the 'topographic image' (Figure 1.11.C).[*63*] While this mode of imaging sounds straightforward, it is important to remember that the image produced with this technique is a convolution of both height and electronic effects of the sample surface. Interpretation of STM images will be discussed in later chapters.

STM tips can be produced from several materials, the two most common are PtIr alloys or tungsten wire. A malleable material, PtIr tips can be produced by simply performing a mechanical cutting to the end of a piece of wire thereby generating a sharp tip. PtIr can also be electrochemically etched to produce sharp tips, however the ease with which it can be mechanically cut causes this to be the preferred method. Electrochemically etched tungsten tips are commonly used in UHV STM since the procedures were previously developed for techniques like field ion microscopy (FIM) and where tungsten oxidation is not a problem in UHV. The use of W tips in techniques developed before STM made them an ideal choice for an atomically sharp imaging probe. While the recipes for producing sharp tips are available, many procedures differ and experience indicates that making these tips is an art. All of the tips used in these experiments were electrochemically etched W tips. They were produced by dipping annealed (resistively heated until white hot for 5 hrs) W wire into a 4 M NaOH solution and applying a 7 V DC bias. The oxidation of the W wire takes place at the anode while

the reduction of hydrogen occurs at the cathode. Figure 1.12.A is a diagram of the experimental setup of the etching process. The bias is applied with a simple power supply and the current of the etching process is monitored with and ammeter. The etching current decreases with etching time since the diameter of the wire in the electrolyte solution gets smaller. The wire eventually breaks at the air/liquid interface and the current drops to nearly zero. The power supply is then immediately shut off to prevent further etching and dulling of the newly formed tip. The wire is quickly removed, washed with water then methanol and its structure investigated with an optical microscope. The tip is then mounted in a magnetic tip holder and loaded into the UHV system. A secondary electron microscopy image of a W STM tip is shown in figure 1.12.B.

The STM utilized in these experiments is a commercially available Omicron variable temperature microscope. Vibration is a major concern when attempting to image on a molecular scale. The entire UHV system is suspended on air legs and vacuum is maintained by non-mechanical, non-moving pumping systems. Furthermore the STM stage is suspended by four springs and equipped with an eddy current dampening mechanism.

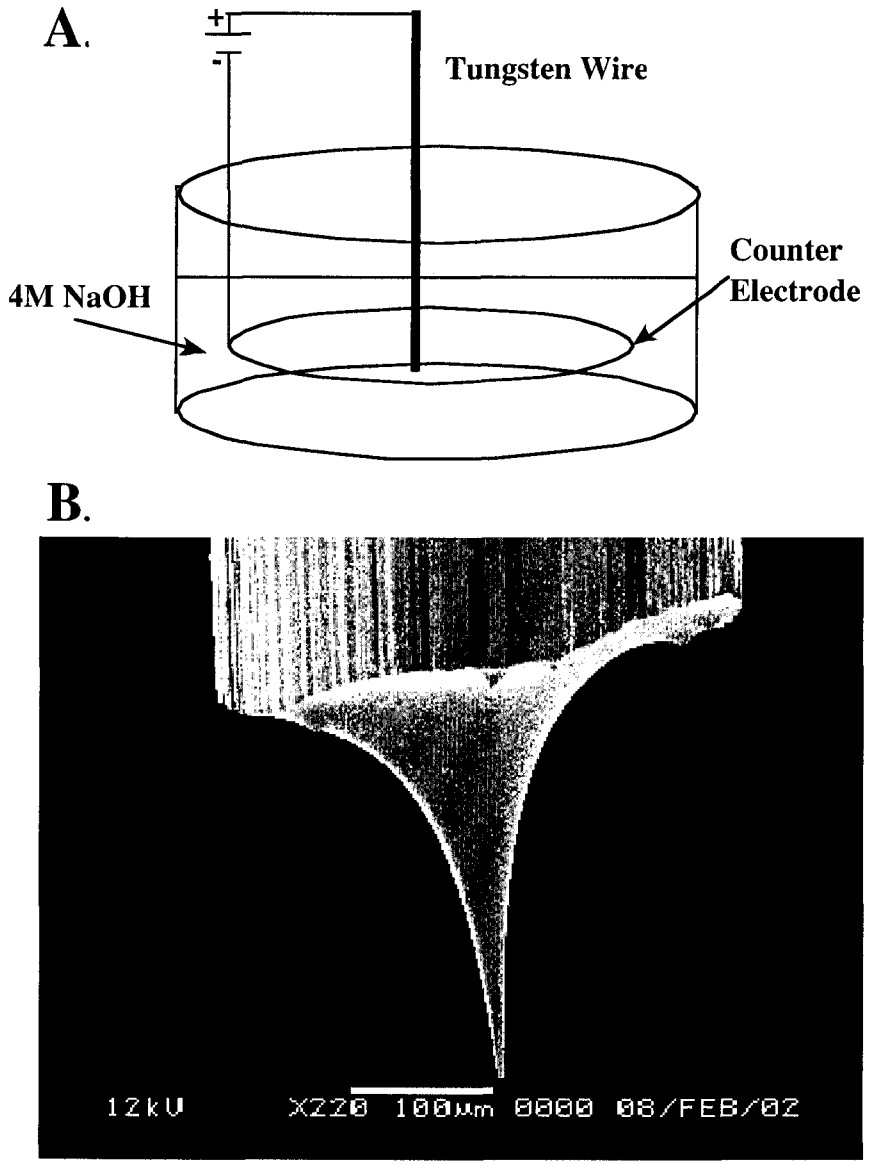

Figure 1.12: (A). Electrochemical setup for producing W STM tips. (B). An SEM of an electrochemically etched tungsten wire.

The use of the all-in-one investigative tools of the multiprobe UHV system allows for the through investigation of the immediate interface between organic semiconductors and Au(111). The ability to study the morphology, electronic structure and binding environment of an organic film allows us to gain valuable insight to these important interfaces. Furthermore, the use of a pristine UHV environment prevents contamination from interfering with the measurements and allows for the through characterization of these technologically important heterojunctions.

References:

[1] M. Pope, H. P. Kallmann, P. Magnante, J. Phys. Chem. **38**, 2042 (1963).

[2] C. W. Tang, S. A. VanSlyke, Appl. Phys. Lett. **51**, 913-915 (1987).

[3] Y. Hamada, T. Sano, M. Fujita, T. Fujii, Y. Nishio, K. Shibata, Jpn. J. Appl. Phys. pt 2 **32**, L514 (1993).

[4] N. Donzé, P. Péchy, M. Grätzel, M. Schaer, L. Zuppiroli, Chem. Phys. Lett. **315**, 405 (1999).

[5] Y. Hamada, T. Sano, M. Fujita, T. Fujii, Y. Nishio, K. Shibata, Jpn. J. Appl. Phys. pt. 2 **32**, L511 (1993).

[6] Y. Hamada, H. Kanno, T. Sano, H. Fujii, Y. Nishio, H. Takahashi, T. Usuki, K. Shibata, Appl. Phys. Lett. **72**, 1939-1941 (1998).

[7] Y. Hamada, T. Sano, M. Fujita, T. Fujii, Y. Nishio, K. Shibata, Chem. Lett., 905 (1993).

[8] M. Matsumura, T. Akai, Jpn. J. Appl. Phys. **35**, 5357-5360 (1996).

[9] Z. Y. Xie, J. S. Huang, S. Y. Liu, Y. Wang, Y. Q. Li, J. C. Shen, Appl. Phys. Lett. **74**, 641 (1999).

[10] J. Kido, Y. Iizumi, Appl. Phys. Lett. **73**, 2721 (1998).

[11] G. Gu, V. Khalfin, S. R. Forrest, Appl. Phys. Lett. **73**, 2399 (1998).

[12] G. Gu, G. Parthasarathy, S. R. Forrest, Appl. Phys. Lett. **74**, 305 (1999).

[13] C. Adachi, S. Tokito, T. Tsutsui, S. Saito, Jap. J. Appl. Phys. B **27**, L269 (1988).

[14] G. Gu, G. Parthasarathy, P. Tian, P. E. Burrows, S. R. Forrest, J. Appl. Phys. **86**, 4076 (1999).

[15] G. Gu, G. Parthasarathy, P. E. Burrows, P. Tian, I. G. Hill, A. Kahn, S. R. Forrest, J. Appl. Phys. **86**, 4067 (1999).

[16] A. Dodabalapur, L. J. Rothberg, T. M. Miller, Appl. Phys. Lett. **65**, 2308 (1994).

[17] T. Mori, K. Miyachi, T. Mizutani, J. Phys. D: Appl. Phys. **28**, 1461-1467 (1995).

[18] H. Mattoussi, H. Murata, C. D. Merritt, Y. Iizumi, J. Kido, Z. H. Kafafi, J. Appl. Phys. **86**, 2642 (1999).

[19] Y. Hamada, H. Kanno, T. Tsujioka, H. Takahashi, T. Usuki, Appl. Phys. Lett. **75**, 1682 (1999).

[20] G. Sakamoto, C. Adachi, T. Koyama, Y. Taniguchi, C. D. Merritt, H. Murata, Z. H. Kafafi, Appl. Phys. Lett. **75**, 766 (1999).

[21] X.-C. Gao, H. Cao, C.-H. Huang, S. Umitani, G.-Q. Chen, P. Jiang, Synth. Met. **99**, 127 (1999).

[22] C. W. Tang, S. A. VanSlyke, C. H. Chen, J. Appl. Phys. **65**, 3610-3616 (1989).

[23] Y. Hamada, C. Adachi, T. Tsutsui, S. Saito, Jpn. J. Appl. Phys. Pt. 1 **31**, 1812 (1992).

[24] G. E. Jabbour, Y. Kawabe, S. E. Shaheen, J. F. Wang, M. M. Morrell, B. Kippelen, N. Peyghambarian, Appl. Phys. Lett. **71**, 1762-1764 (1997).

[25] L. S. Hung, C. W. Tang, Appl. Phys. Lett. **74**, 3209 (1999).

[26] A. Yamamori, C. Adachi, T. Koyama, Y. Taniguchi, J. Appl. Phys. **86**, 4369 (1999).

[27] Y. Shirota, Y. Kuwabara, H. Inada, T. Wakimoto, H. Nakada, Y. Yonemoto, S. Kawami, K. Imai, Appl. Phys. Lett. **65**, 807 (1994).

[28] C. Giebeler, H. Antoniadis, D. D. C. Bradley, Y. Shirota, J. Appl. Phys. **85**, 608 (1999).

[29] E. W. Forsythe, D. C. Morton, C. W. Tang, Y. Gao, Appl. Phys. Lett. **73**, 1457 (1998).

[30] S. R. Forrest, Chem. Rev. **97**, 1793-1896 (1997).

[31] H. E. Katz, J. Mater. Chem. **7**, 369 (1997).

[32] D. J. Gundlach, Y.-Y. Lin, T. N. Jackson, D. G. Schlom, Appl. Phys. Lett. **71**, 3853 (1997).

[33] H. E. Katz, Z. Bao, J. Phys. Chem. B **104**, 671 (2000).

[34] C. D. Dimitrakopoulos, S. Purushothaman, J. Kymissis, A. Callegari, J. M. Shaw, Science **283**, 822 (1999).

[35] Z. Bao, A. J. Lovinger, A. Dodabalapur, Appl. Phys. Lett. **69**, 3066 (1996).

[36] A. R. Brown, C. P. Jarrett, D. M. de Leeuw, M. Matters, Synth. Met. **88**, 37 (1997).

[37] J. G. Laquindanum, H. E. Katz, A. J. Lovinger, J. Am. Chem. Soc. **120**, 664 (1998).

[38] J. G. Laquindanum, H. E. Katz, A. J. Lovinger, A. Dodabalapur, Chem. Mater. **8**, 2542 (1996).

[39] A. Dodabalapur, L. Torsi, H. E. Katz, Science **268**, 270 (1995).

[40] J. W. Mayer, S. S. Lau, *Electronic Materials Science: For Integrated Circuits in Si and GaAs* (Macmillan Publishing Company, 1990).

[41] M. Pope, C. E. Swenberg, *Electronic Processes in Organic Crystals and Polymers* (Oxford University Press, Oxford, 1999).

[42] C. H. Chen, J. Shi, C. W. Tang, Macromol. Symp. **125**, 1-48 (1997).

[43] J. H. Schön, Z. Bao, J. Appl. Phys. **89**, 3526 (2001).

[44] C. J. Bloom, C. M. Elliot, P. G. Schroeder, C. B. France, B. A. Parkinson, J. Am. Chem. Soc. **123**, 9436 - 9442 (2001).

[45] M. A. Baldo, S. R. Forrest, Phys. Rev. B **64**, 85201 (2001).

[46] S. M. Sze, *Physics of Semiconductor Devices* (John Wiley & Sons, ed. 2nd, 1981).

[47] M. M. Dovek, C. A. Lang, J. Nogami, C. F. Quate, Phys. Rev. B **40**, 11973 (1989).

[48] R. Schlaf, B. A. Parkinson, P. A. Lee, K. W. Nebesny, N. R. Armstrong, App. Phys. Lett. **73**, 1026 -1028 (1998).

[49] R. Schlaf, B. A. Parkinson, P. A. Lee, K. W. Nebesny, N. R. Armstrong, Surface Science **420**, L122 - L129 (1999).

[50] P. G. Schroeder, M. W. Nelson, B. A. Parkinson, R. Schlaf, Surf. Sci. **459**, 349 (2000).

[51] R. Schlaf, P. G. Schroeder, M. W. Nelson, B. A. Parkinson, P. A. Lee, N. R. Armstrong, J. Appl. Phys. **86**, 1499 (1999).

[52] P. G. Schroeder, C. B. France, J. B. Park, B. A. Parkinson, J. Appl. Phys. **91**, 3010 (2002).

[53] P. G. Schroeder, C. B. France, J. B. Park, B. A. Parkinson, J. Phys. Chem. B **107**, 2253 (2003).

[54] P. G. Schroeder, C. B. France, B. A. Parkinson, R. Schlaf, J. Appl. Phys. **91**, 9095 (2002).

[55] A. Bishop, R., G. S. Girolami, R. G. Nuzzo, J. Phys. Chem. B **104**, 754 (2000).

[56] B. Chalamala, D. Uebelhoer, R. Reuss, Rev. Sci. Instrum. **71**, 320 (2000).

[57] D. King, Surf. Sci. **47**, 384 (1975).

[58] P. A. Redhead, Vacuum **12**, 203 (1962).

[59] L.-Q. Wang, K. F. Ferriw, G. S. Herman, M. H. Engelhard, J. Vac. Sci. Technol. A **18**, 1893 (2000).

[60] C. Wiegenstein, K. Schulz, J. Scott, Rev. Sci. Instrum. **69**, 3707 (1998).

[61] J. N. Wilson, D. J. Titheridge, L. Kieu, H. Idriss, J. Vac. Sci. Technol. **18**, 1887 (2000).

[62] G. Binning, H. Rohrer, C. Gerber, E. Weibel, Phys. Rev. Lett. **49**, 57 (1982).

[63] R. Wiesendanger, *Scanning Probe Microscopy and Spectroscopy* (Cambridge University Press, New York, 1994).

Chapter 2: Review of Previous Pentacene on Au(111) Research

2.1 Origin of Information

This chapter is intended to provide the reader with all of the information and experiments that have been performed in the Parkinson group concerning the pentacene on Au(111) interface. The experiments and results reviewed in this chapter come from two published reports, also making up the majority of chapters 4 and 5 in the thesis of P. G. Schroeder, and will be referred to in later chapters.

(1) P. G. Schroeder, C. B. France, J. B. Park, and B. A. Parkinson, *J. Appl. Phys.*, **91**, 3010, (2002).

(2) P. G. Schroeder, C. B. France, J. B. Park, and B. A. Parkinson, *J. Phys. Chem. B*, **107**, 2253, (2003).

This chapter will not contain all of the information presented in the published reports but it will cover the necessary information to inform the reader on the initial experiments that were performed. It is suggested that the original works be obtained for further clarification and additional detail. In the above published reports C. B. France completed a majority of the scanning tunneling microscopy (STM) work, performed statistical analysis of the STM images, was responsible for obtaining the optical absorbance data, and assisted in the STM image modeling and photoemission data collected for the interface band lineup.

2.2 Orbital Alignment and Morphology of Pentacene on Au(111)

The energy level alignment of the pentacene/Au interface was measured using photoemission spectroscopy. The XPS measurements when combined with UPS allow for the determination of the energy level alignment at the metal/semiconductor interface. Figure 2.1 shows the He I UPS spectra, which were measured in a similar fashion to the experiments described in chapter 1. The full spectra are shown in the center part of the figure where the bottom spectrum is of the bare gold substrate. The high biding energy cutoff (HBEC) is normalized, expanded and shown on the left of the figure. This is the region from which the work function of the interface can be determined. This shift in the work function is plotted as the black boxes in figure 2.2. From this plot it is determined

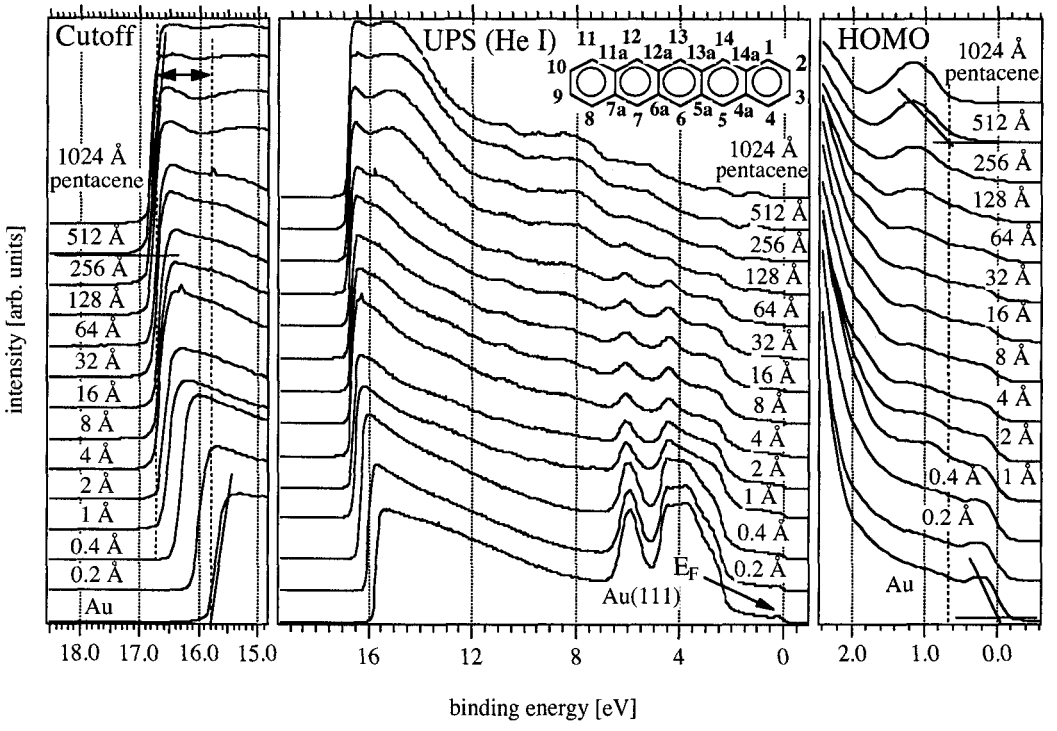

Figure 2.1: UPS He I spectra of pentacene deposited on Au(111). The center portion shows the full spectra on a binding energy scale. The spectra on the left are the magnified high binding energy cutoff (HBEC) used to determine the sample work function. The right side shows the magnified region where the gold Fermi edge and the HOMO peak of the pentacene are observed. The molecular structure of pentacene is shown with the IUPAC numbering system for the C atom positions.

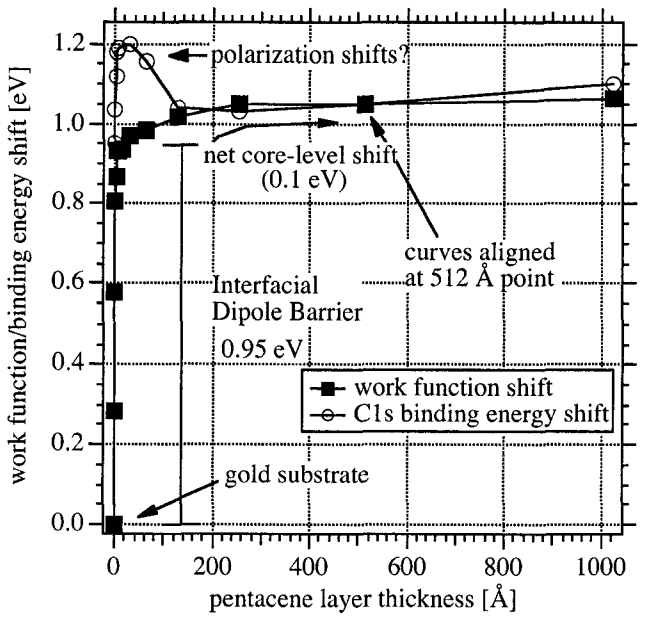

Figure 2.2: Pentacene on Au(111): plot of the C 1s binding energy shift and work function shift as a function of the pentacene layer thickness. The difference between these shifts yields the magnitude of the interfacial dipole barrier.

the work function shift or magnitude of the interface dipole is 0.95 eV. It is also important to note that the shift in the work function is complete by about the 7th experimental point corresponding to a 4Å thick film. This is also clearly visible in HBEC section of figure 2.1.

The region of the spectra showing the Fermi level of the metal and the evolution of highest occupied molecular orbital (HOMO) is presented on the right of figure 2.1. The difference in the metal Fermi level and the pentacene HOMO level gives the value of the hole injection barrier height (b_h). The spectra indicate that b_h = 0.55 eV. Since photoemission spectroscopy can only measure the energy states of filled orbitals, the energy position of the lowest unoccupied molecular orbital (LUMO) of pentacene had to be obtained through another method. The lowest energy optical transition obtained from optical absorbance was used to obtain the energy of the HOMO-LUMO gap. The absorbance spectrum was obtained from a solid-state film that had been deposited onto a quartz slide. The spectrum was obtained at room temperature and is presented in figure 2.3. The HOMO-LUMO gap was determined to be 1.85 eV.

The complete band diagram for the pentacene / Au(111) interface is shown in figure 2.4. The information that is known from the previous spectra discussed above is the magnitude of the Au(111) work function, the shift in work function (vacuum level shift), the size of the hole injection barrier (b_h), and the HOMO-LUMO gap of the

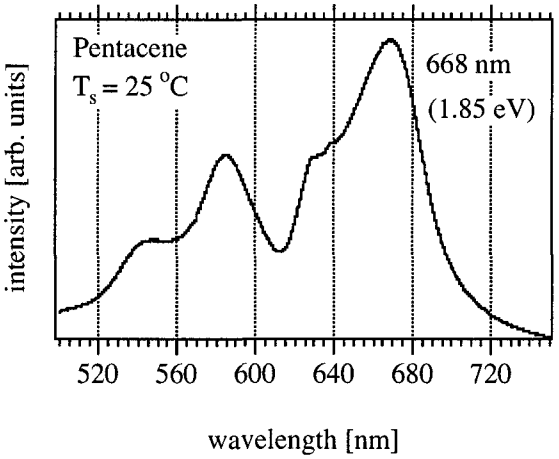

Figure 2.3: Optical absorption spectra of a pentacene film used to estimate the band gap.

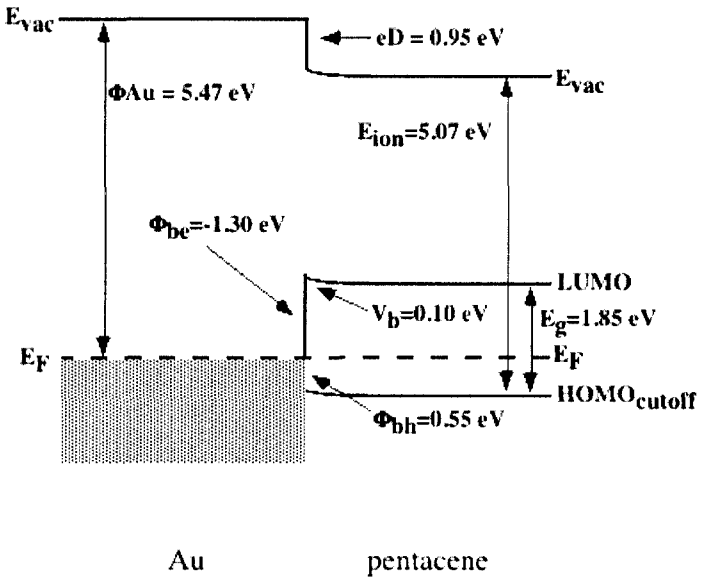

Figure 2.4: Band diagram of the pentacene/Au(111) interface.

pentacene. From these details the height of the electron injection barrier can be determined (b_e) to be –1.30 eV as well as the ionization energy (E_{ion}) of the pentacene on Au(111) (5.07 eV).

Scanning tunneling microscopy was used to investigate the morphology of the pentacene molecules on the Au(111) substrate. The film thicknesses were estimated to be approximately one monolayer. Pentacene was observed to form long one-dimensional rows or strips across the surface. Figure 2.5 shows an 80 × 80 nm STM image of the row structures on multiple Au(111) terraces. These row structures were not found to have equal spacing between them. The black and white boxes in figure 2.5 illustrate the rows that are more widely space apart.. The black box, labeled A, B & C, shows the rows to be closely spaced where as the white boxes labeled D have a lower density.

Higher resolution STM images, like that shown in figure 2.6, suggests the molecules lie flat on the Au(111) substrate and are commensurate with the hexagonal lattice. The STM image on top of figure 2.6 has some pentacene structures overlaid on the image to demonstrate the location of individual molecules. The molecular width of the pentacene molecules was determined from cross-sectional analysis and was measured to be 5.6 ± 0.2Å. This is slightly larger than the para-hydrogen internuclear distance found in the bulk crystal structure of 5.03Å. It is also important to note that the outer rings of the molecules appear brighter than the center rings.

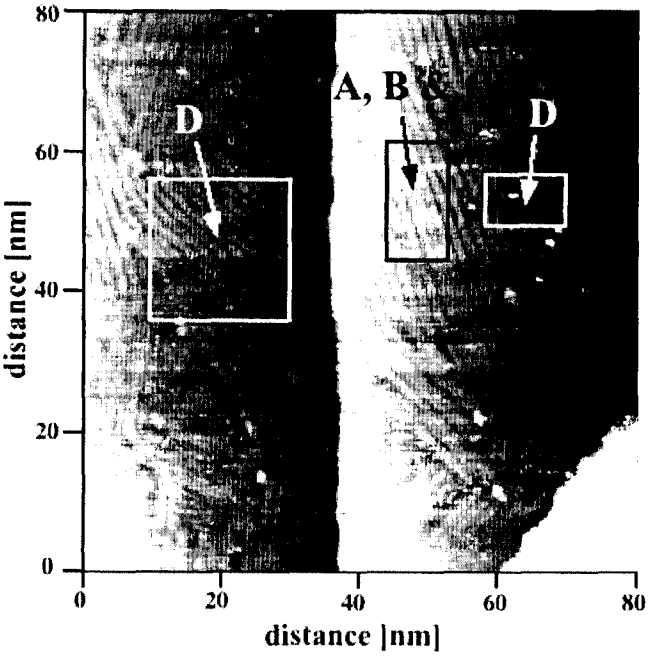

Figure 2.5: STM (80 x 80 nm) image of 0.8 - 1.0 monolayer of pentacene deposited on Au(111). A substrate step edge is observed down the center of the image. Linear chains of pentacene molecules are observed. The black box shows a region of closely spaced rows consisting of type A, B and/or C unit cells. The white boxes show regions containing type D unit cells with larger spacing.

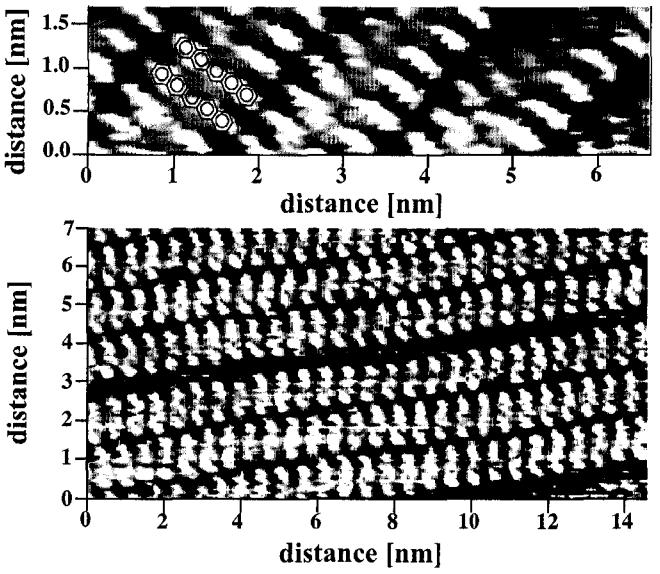

Figure 2.6: (TOP) High resolution STM image of pentacene molecules with type A unit cell, with the pentacene molecules in line with those in the adjacent row. (BOTTOM) High resolution STM image of pentacene where the molecules are more staggered relative to those in the adjacent row, which correspond to the type B or C unit cell. The region containing extra space between the rows corresponds to an extra gold substrate atom between the rows of pentacene molecules. This spacing reflects the type D unit cell.

The geometry of the pentacene molecule can produce commensurate structures on the hexagonal gold lattice when the outer rings are lying on atop gold sites (figure 2.7). Four proposed unit cell structures for pentacene on Au(111) were observed during these experiments. Analysis has included the measured distances between adjacent pentacene molecules was well as the relative orientation of the molecules to each other. A histogram of 240 measurements of row widths (measured perpendicular to the row direction) taken from 23 different images is shown in the bottom of figure 2.7. Two distinct peaks are observed in the row-width histogram, centered at 15Å and 17.5Å and another smaller peak at 21.5Å. The combination of high-resolution STM images and the histogram indicates that a number of different ordered structures are formed by pentacene on the metal substrate.

Several images displayed the type A ordering, modeled in the diagram of figure 2.7. The individual molecules lie perpendicular to the row direction and have a unit cell of $2 \times 3\sqrt{3}$ with respect to the gold lattice. A high-resolution STM image of this structure with the molecules aligning themselves perpendicular to the row axis is shown in top of figure 2.6. The long axis of the unit cell, corresponding to the unit cell distance between rows is 15.0 Å. This unit cell produces a packing density of 1.16×10^{14} molecules/cm^2, and statistically, fits into the first peak in the histogram (labeled A, B & C). Type B is a $2 \times 2\sqrt{7}$ unit cell and has a lower packing density of 1.14×10^{14} molecules/cm^2.

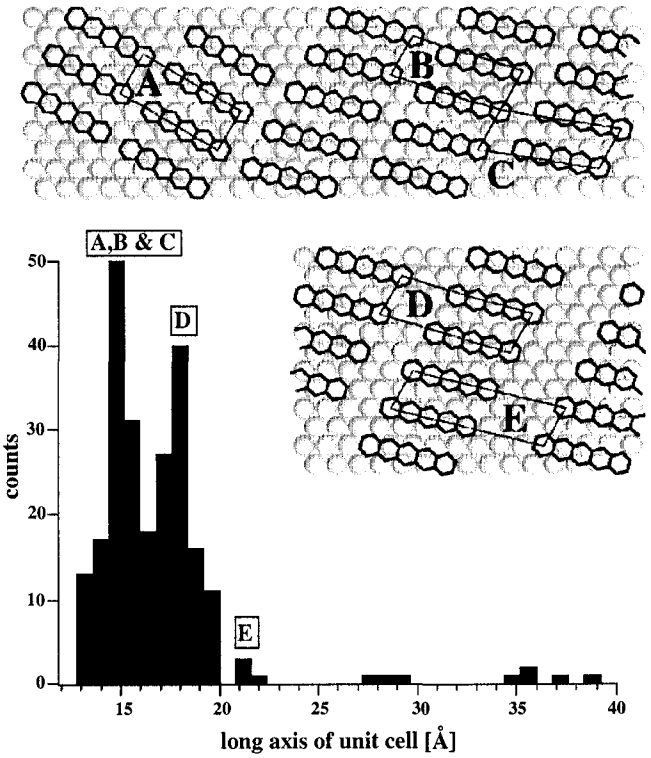

Figure 2.7: (TOP) Diagram of pentacene molecules adsorbed on the Au(111) lattice. Four types of unit cells are diagramed. Type A has a (2 x $3\sqrt{3}$) relationship with the Au(111) surface. Type B has a (2 x $2\sqrt{7}$) unit cell with a slightly lower packing density than type A. Type C appears slightly more staggered than type B and has a (2 x $\sqrt{31}$) unit cell. Type D is similar to type B, except for an extra row of gold atoms between adjacent rows of pentacene molecules yielding a (2 x $\sqrt{39}$) unit cell. Larger spacings such as type E (2 x $2\sqrt{13}$) appear to be possible.

This structure was more commonly observed and has a measured long axis unit cell of 15.3 Å, fitting within the first peak of the histogram. The type C structure was also prevalent in the STM images, having a model unit cell of $2 \times \sqrt{31}$. Again, the long axis of this row structure fell with in the first statistical peak of the histogram with a 16.0 Å length. The primary difference between the type B and C structures is the slight offset between the two rows. These slight differences in structure are likely energetically very similar and can be difficult to discern without high-resolution STM images. It is also important to note that the measurements used to make up the histogram were of repeat row distances perpendicular to the row direction. While this is consistent with the long axis measured for the type A unit cell (molecules are perpendicular to row direction) it is not strictly correct for the type B and C. The average row width measured for type A, B, and C was 14.8 ± 0.9 Å, which is in the range of the $3\sqrt{3}$ gold atom distance of 14.96 Å. This would correspond to the measured distance (perpendicular to the row direction) for each of these unit cells.

Not all of the pentacene unit cells have equivalent row separation; figure 2.5 shows the lower density structures in the white boxes (labeled D). Statistically, these lager width rows fall into the second peak in the histogram, centered at 17.5Å for the long axis. Modeled as the type D unit cell, it is very similar to the C and B structures with an extra gold atom between the rows. This model is presented in the middle right of figure

2.7, with a $2 \times \sqrt{39}$ lattice dimension (5.76 × 18.0 Å). A high resolution STM image of this structure, within other B and C unit cells is shown in the bottom of figure 2.6. The row with the greater separation is the D row whereas the others are B and C. Another row having an even greater separation was observed with long axis unit cells centered at 21.5Å in the histogram (bottom, figure 2.7). This would have a similar unit cell to the previously discussed cells only another gold atom would be present between the rows. The lattice parameters for this type E cell were $2 \times 2\sqrt{13}$ which correlates to 5.76 × 20.8 Å). Since the publication of this report, we have observed even more widely spaced structures than this type E form. We noticed that the spacing of these rows was dependent on the thickness of the pentacene film and have performed coverage dependant studies to gain further understanding of the system. See chapter 3 for some of the interesting structures that were observed.

All of the row structures presented in these reports had a short unit cell axis of 5.6 ± 0.2 Å corresponding well to a two gold atom separation (5.76Å). This unit cell spacing of the molecules within the rows are less dense than that found in the pentacene bulk, 5.03 Å. This decrease in density of the pentacene molecules on the Au(111) would reduce the molecule-molecules interactions which is presumably energetically offset by a stronger substrate-molecule interaction. We believe the formation of the large interface

dipole between these two materials could be an important indicator to the strength of this interaction. Additional discussion on this will be included in chapter 3.

Chapter 3: Scanning Tunneling Microscopy Study of the Coverage-Dependent Structures of Pentacene on Au(111)

Published: C.B. France, P.G. Schroeder, J.C. Forsythe and B.A. Parkinson, Langmuir, **19**, 1274, (2003).

3.1 Abstract:

Pentacene thin films on Au(111) have been investigated at various coverages using scanning tunneling microscopy (STM) and temperature-programmed desorption (TPD). Two distinct binding environments, surface bound and bulk-like, were evident from TPD. The surface monolayer and multilayer pentacene molecules had binding energies of 110 and 106 kJ/mol, respectively. STM investigations of surfaces with pentacene coverages of around 0.25 monolayer equivalents (MLE) yielded four different ordered structures with end-to-end nearest neighbor interactions. Increasing the

pentacene coverage from 0.25 to 1 MLE leads to ordered single monolayer films with rows of molecules aligned side-by-side. STM images of an annealed pentacene film revealed that these side-by-side rows are the dominant structure for complete monolayer films. A periodic row structure with a large spacing of 61 Å was observed to form in films with coverages greater than a monolayer (1.1–1.5 MLE). Upon deposition of 2 MLE, the widely spaced periodic row structure appears to be covered with a layer similar to the monolayer structure. STM images of these coverage-dependent structures and their relationship to bulk crystalline pentacene are discussed.

3.2 Introduction:

The interface between organic semiconductors and metal contacts is important because charge transfer across this interface will be crucial for the operation of new organic-based devices. Ohmic behavior at these contacts is often desired but energetic and structural barriers can influence the electronic properties of the interface.[*1*] Therefore, it is useful to investigate the structural and energetic properties of these interfaces.

Pentacene single crystals have the highest field effect mobility found for an organic semiconductor.[*2*] Thin films of this material have been used for the fabrication of organic field-effect transistors on insulating oxide and plastic electrodes.[*2*] Gold has

commonly been used for the source and drain contacts to the organic semiconductor layer or crystal therefore; the structure of this interface is of interest. We have previously measured the energy level alignment of the pentacene/Au(111) interface using photoelectron spectroscopy, where a large interface dipole barrier was measured in the first layer of pentacene molecules.[*3*] Scanning tunneling microscopy (STM) studies of near monolayer coverages showed that molecules of pentacene on Au(111) form one-dimensional rows with the pentacene molecules aligning perpendicular to, or nearly perpendicular, to the row direction.[*4*] Similar structures were also found for pentacene on Cu(110) substrates.[*5*] Investigations of pentacene films with 1–1.5 monolayer equivalents (MLE) revealed a unique widely spaced periodic row structure.[*6*] Herein we report on the coverage-dependent structures formed by pentacene on Au(111) and the relationship between these structures and the bulk crystalline pentacene structure.

3.3 Experimental section:

Experiments were performed in a commercial Omicron Multi-probe ultrahigh vacuum (UHV) system (base pressure 5×10^{-11} mbar). This system is equipped with variable temperature scanning tunneling microscopy (VT-STM),[*7*] low energy electron diffraction (LEED), X-ray and ultraviolet photoelectron spectroscopy (XPS and UPS) using a VSW EA125 single channel hemispherical analyzer. Temperature programmed desorption (TPD) has been added to the UHV system and is described below. A physical

vapor deposition chamber (base pressure 1×10^{-9} mbar) is attached to the UHV system allowing sample and films to be prepared in situ.

The gold film was prepared by heating a 1 cm × 1 cm mica sample, attached to the sample plate using molybdenum clips, for 24 h in UHV at 300 °C to evaporate surface contaminants. Gold was then evaporated from a resistively heated tungsten basket onto the heated mica substrate.[*8*] The Mo clips provided an electrical contact to the gold surface during STM imaging. Sputter (3 keV Ar^+) and anneal (350 °C) cycles were used to clean and flatten the Au(111) surface. The chemical purity of the surface was determined with XPS (Mg kα, 50 eV pass energy) and the presence of the $23 \times \sqrt{3}$ reconstruction was confirmed with STM.

Pentacene (Aldrich Chemical Co.) films were deposited under UHV (base pressure 1×10^{-9} mbar) from a resistively heated boron nitride crucible (source temperature, 142 °C). The source was maintained at 120 °C for 12 h prior to deposition to remove any volatile contaminants. Pentacene was then deposited at a rate of 4 Å/min as monitored by a Leybold quartz crystal microbalance (QCM). The Au(111) substrate was maintained at room temperature during the deposition.

The Au(111) surface was renewed for each experiment with a sputter and anneal cycle. Pentacene films with various thicknesses were then deposited on the cleaned surface. The STM images were obtained in a constant current mode with sample biases

ranging from –2.0 to +2.0 V and tunneling currents between 0.1 and 0.5 nA. A background plane fit or slope correction was the only post collection processing applied to the images with the exception of Figures 3.3b and 3.8b, which were obtained from an FT averaging algorithm utilizing Scanning Probe Image Processing software (Image Metrology Aps.).

Temperature-programmed desorption experiments were performed by heating the sample using a resistive heater located directly behind the sample holder. The substrate surface temperature was measured using a Raytek Raynger MX™ IR thermometer. Emissivity values were determined using a calibration plot from a standard thermocouple with the sample holder at thermal equilibrium, giving the emissivity used for the Au(111) film of 0.12. The temperature was measured through an infrared transparent ZnSe window that is mounted on the UHV chamber. The signal from the IR thermometer is split and sent to a computer and a Eurotherm™ 2404 temperature controller. The Eurotherm™ temperature controller was used to control the heating rate (typically 15 °C/min) of the sample. Desorbed species were detected with a Stanford Research Systems quadrupole mass spectrometer (model RGA300) with an electron multiplier detector and ionization filament allowing for the detection of molecular fragments. The separation between the sample surface and the RGA is approximately 3 cm, with the substrate surface normal to the mass detector. The electron multiplier counts from a pre-

selected mass are sent from the RGA to a computer. National Instruments Labview™ software is used on a PC computer to control, collect, and store temperature and mass count data as well as to plot the TPD spectrum. The Redhead equation[9] was used to determine the binding energy of a species based on the temperature of maximum desorption intensity.

3.4 Results and Discussion:

TPD spectra for various pentacene coverages desorbed from a Au(111) film are shown in Figure 3.1, where the bottom spectra has the lowest initial coverage (2 Å) and the upper most has the highest coverage (10 Å). TPD revealed two different binding environments at this interface. Due to nonlinearity of our quadrapole mass detector near its high mass limit, we measured the desorbed pentacene molecules at one-half their principal mass-to-charge ratio, which would correspond to a symmetrical fragment or a doubly charged molecule. Two peaks can be seen in the spectra of Figure 3.1 (labeled A and B) indicating that there are two different adsorbate environments present. Peak A in Figure 3.1 is only present for coverages greater than 5 Å and has a peak temperature of 106 °C, corresponding to a calculated binding energy of 106 kJ/mol. Investigation of different coverages of pentacene on Au(111) found that the intensity of peak A increased with increasing initial film thickness. In conjunction with STM analysis of these films before TPD, it was determined that the signal from peak A originates from a multilayer

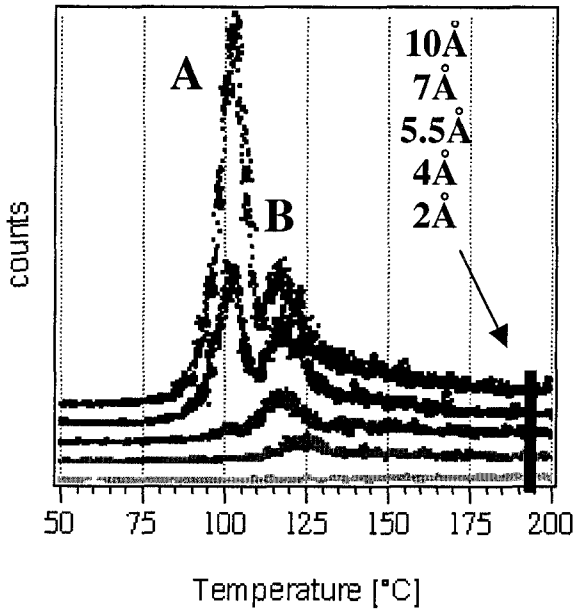

Figure 3.1: TPD spectra of pentacene desorbed from a Au(111) film. The bottom spectrum has 2 Å initial film coverage and the top 10 Å. Peak A originates from multilayer pentacene with a peak temperature of 106°C and a binding energy of 106 kJ/mole. Peak B has a peak temperature of 120°C and a binding energy of 110 kJ/mol and comes from monolayer pentacene on the Au(111).

environment where the interaction is exclusively from other pentacene molecules and so represents the sublimation energy of pentacene. Peak B is seen in all of the spectra, including the 2 Å spectrum and has a peak temperature of 120 °C and calculated binding energy of 110 kJ/mol. The peak is always found at low coverages and its intensity saturates at coverages above 5 Å. STM analysis of pentacene films, where only peak B is present in the TPD spectra, showed only monolayer and submonolayer structures on the surface. Therefore peak B is attributed to the initial monolayer of pentacene on the Au(111) surface. This monolayer-multilayer distinction allowed TPD to be used to determine the film coverage in further investigations of this interface. It is also noteworthy that we observed a large (0.95 eV) initial work function shift in the orbital alignment of pentacene on Au(111), with the majority of the shift occurring within the first 4 Å of deposition.[*3*, *4*] This work function shift is attributed to donated electron density from the pentacene molecules to the Au(111). The increased interaction between the first pentacene layer and the Au(111) is likely the cause for the larger binding energy of the submonolayer film on the surface, as determined with TPD (4 kJ/mol greater than multilayer films). This stronger binding at lower coverages is also evident by peak B shifting to higher binding energies at lower film coverages, which would correspond to an increased interaction at lower coverages which is consistent with the initial work function shift.[*3*] Therefore at lower pentacene coverages more electron density per

molecule is donated from the organic film to the Au(111) thus increasing the interaction between the two species at the interface.

Scanning tunneling microscopy was used to investigate the structures formed by pentacene molecules on the Au(111) surface. Four distinct structures were observed after deposition of about 0.25 MLE of pentacene. None of these four low-coverage structures lifted the Au(111) $23 \times \sqrt{3}$ reconstruction which was simultaneously observed in many STM images. The reconstruction was useful for calibrating the size of the structures and to identify their orientation with respect to the Au substrate lattice. The lowest coverage structure observed is labeled type 1 and is shown in a 25.4 nm × 28.7 nm STM image, (Figure 3.2A). Pentacene molecules in the type 1 structure form paired rows where the pentacene molecules align perpendicular to the Au(111) $23 \times \sqrt{3}$ reconstruction (as observed in other STM images). Each molecule interacts with its nearest neighbor in an end-to-end fashion. The center-to-center distance between the pentacene molecules in the end-to-end rows is 18 ± 1 Å. The separation between the two rows of pentacene molecules that make up the paired row is 13 ± 1 Å, the repeating distance between the paired rows is 32 ± 1 Å and the measured unit cell angle is 86 ± 3°. Continued imaging with the STM tip tended to disrupt the ordering of this structure. Common disruptions include pushing together or separating molecular rows that previously were paired with other rows. In addition, many disordered or 'noisy' areas in the images were observed

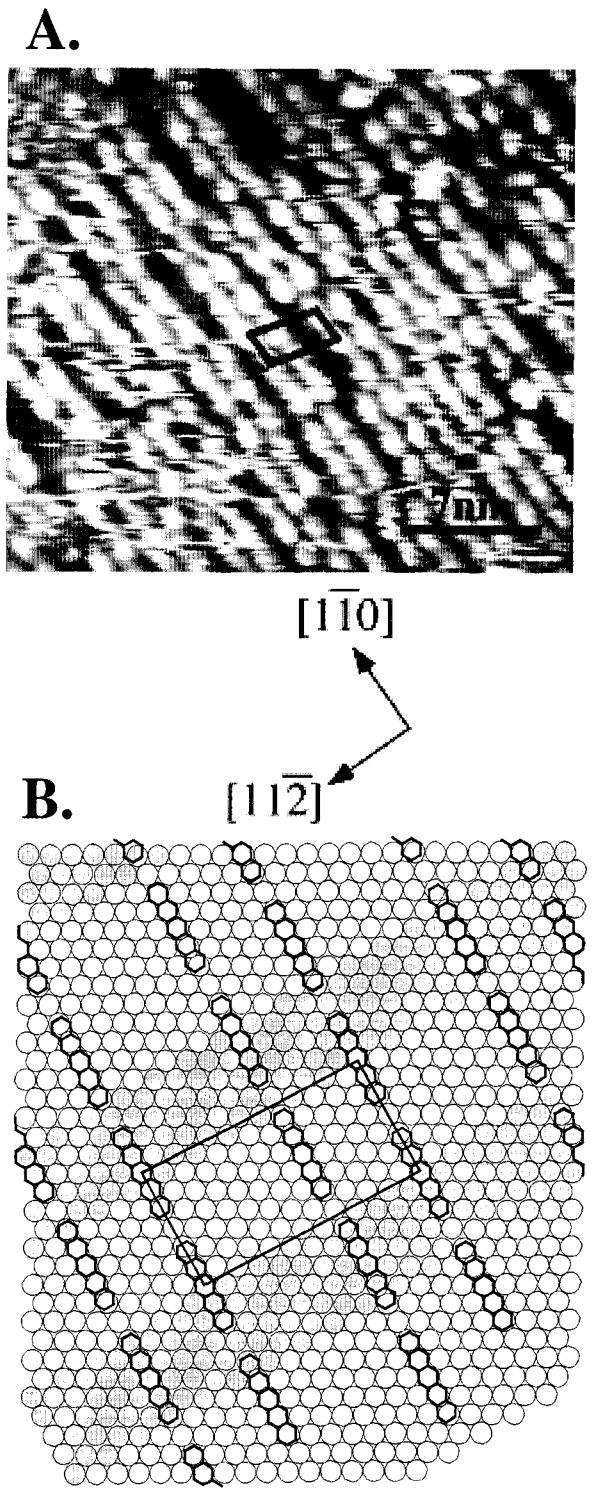

Figure 3.2: (A) A 25.4 nm x 28.7 nm STM image of the low-coverage type 1 pentacene structure. (-2.0 V, 0.3 nA) (B) A proposed model of the pentacene ordering in the 6 x $\sqrt{127}$ type 1 structure. The dark substrate atoms represent the elevated 23 x $\sqrt{3}$ reconstruction of the Au(111). The directional vectors for the Au(111) are consistent for the model and STM image.

and attributed to the STM tip disrupting the loosely packed (low-coverage) structure. Figure 3.2B shows a proposed model of the paired row structure, which is aligned with the STM image as indicated by the directional vectors. All Figures with directional vectors will be aligned for all models and STM images in the Figure. The long axis of the pentacene molecules is aligned perpendicular to the gold reconstruction $[1\bar{1}2]$, represented by the dark substrate atoms. It is important to note that in the model shown in Figure 3.2B and all subsequent models, the actual position of the molecules with respect to the substrate Au atoms has not been directly observed but is based on the expected location as will be discussed below. This structure corresponds to an unusual 6 $\times$ $\sqrt{127}$ (17.3 $\times$ 32.4 Å) noncentrosymmetric overlayer unit cell with a theoretical packing density of 3.57×10^{13} molecules/cm^2 and a unit cell angle of 87.5°. The reason for the pairing of the pentacene rows is unclear since there is sufficient room for pentacene molecules to adsorb between the paired rows as was seen after STM tip disruption of the structure and is shown in the proposed model.

An 18.7 $\times$ 18.7 nm STM image in Figure 3.3A shows the type 2 structure. The Au(111) 23 $\times$ $\sqrt{3}$ reconstruction, $[1\bar{1}2]$, is observed beneath this structure running nearly vertical across the image as depicted by the directional vectors. A unit cell averaged 5.6 $\times$ 7.6 nm STM image is shown in Figure 3.2B along with the observed unit cell. The experimentally measured unit cell distance between the pentacene molecules (center-to-

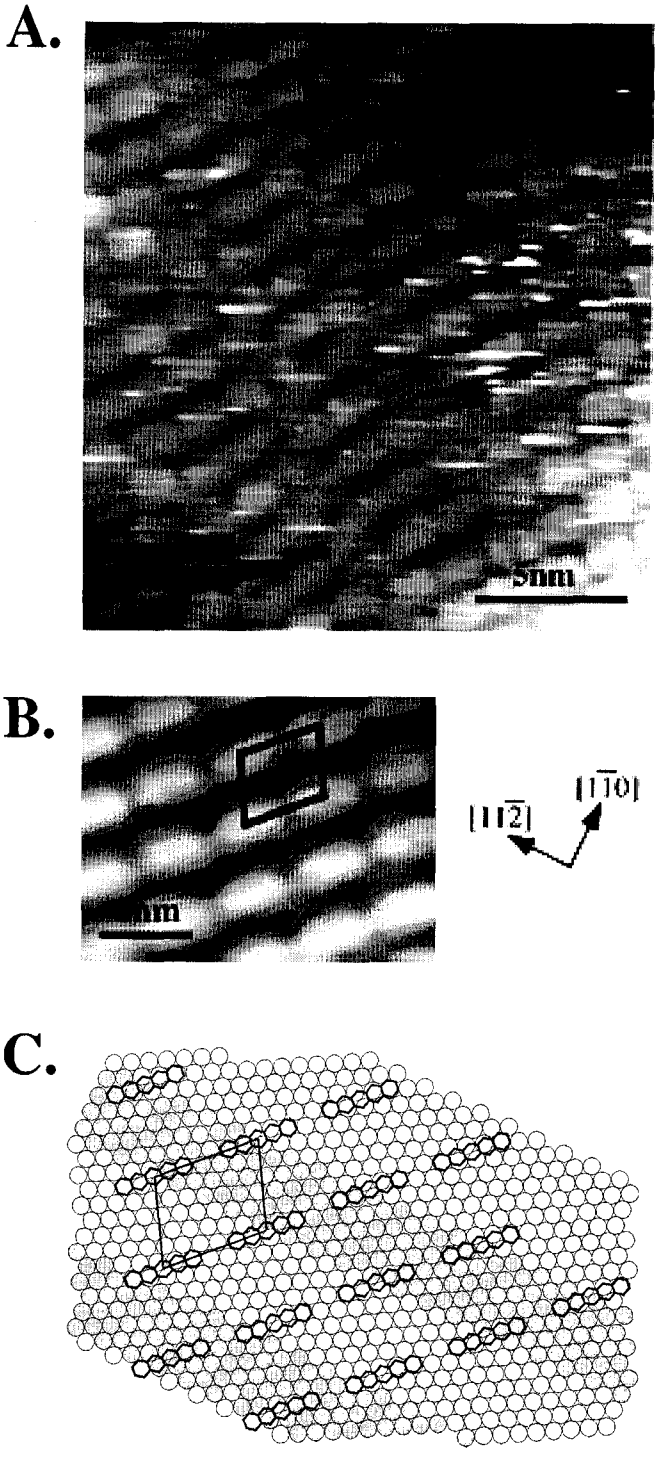

Figure 3.3: (A) A 18.7 × 18.7 nm STM image of type 2 ordering on Au(111). (-2.0 V, 0.3 nA) (B) An averaged STM image produced from Figure 3.3A using SPIP software. The pentacene unit cell is drawn has been added. (C) A model of the pentacene in the $3\sqrt{3} \times \sqrt{19}$ type 2 overlayer. The Au(111) directional vectors are consistent for the entire figure.

center) in the end-to-end rows is 18 ± 1 Å with a unit cell distance of the side-by-side molecules of 15 ± 1 Å and a unit cell angle of 105 ± 3°. A proposed model of this structure is shown in Figure 3.3C where the pentacene molecules form a $3\sqrt{3} \times \sqrt{39}$ (15.0 × 18.0 Å) unit cell with $\alpha = 106.1°$ (unit cell angle) with a theoretical packing density of 3.7×10^{13} molecules/cm^2.

Figure 3.4A shows a 50 nm × 50 nm STM image of the type 3 low-coverage structure. The structures in the upper left of Figure 3.4A are side-by-side rows or single molecular width rows that will be discussed below. The lower left of the image contains two polymorphic structures where the left side shows type 1 ordering while the molecules on the right side of the image are the type 3 structure. By averaging measurements of many STM images it was determined that the pentacene molecules in the type 3 structure have a center-to-center distance of 17 ± 1 Å in the end-on-end row direction and 13 ± 1 Å center-to-center separation that determines the other unit cell dimension, $\alpha = 51 \pm 3°$. A close-up STM image (9.9 nm × 10.1 nm) showing the pentacene unit cell and Au directional vectors for the Figure is presented in Figure 3.4B. A proposed model of the type 3 structure is offered in Figure 3.4C where a $2\sqrt{7} \times \sqrt{37}$ (15.3 × 17.5 Å) with $\alpha =$ 52.8° pentacene unit cell was found with a theoretical packing density of 3.73×10^{13} molecules/cm^2.

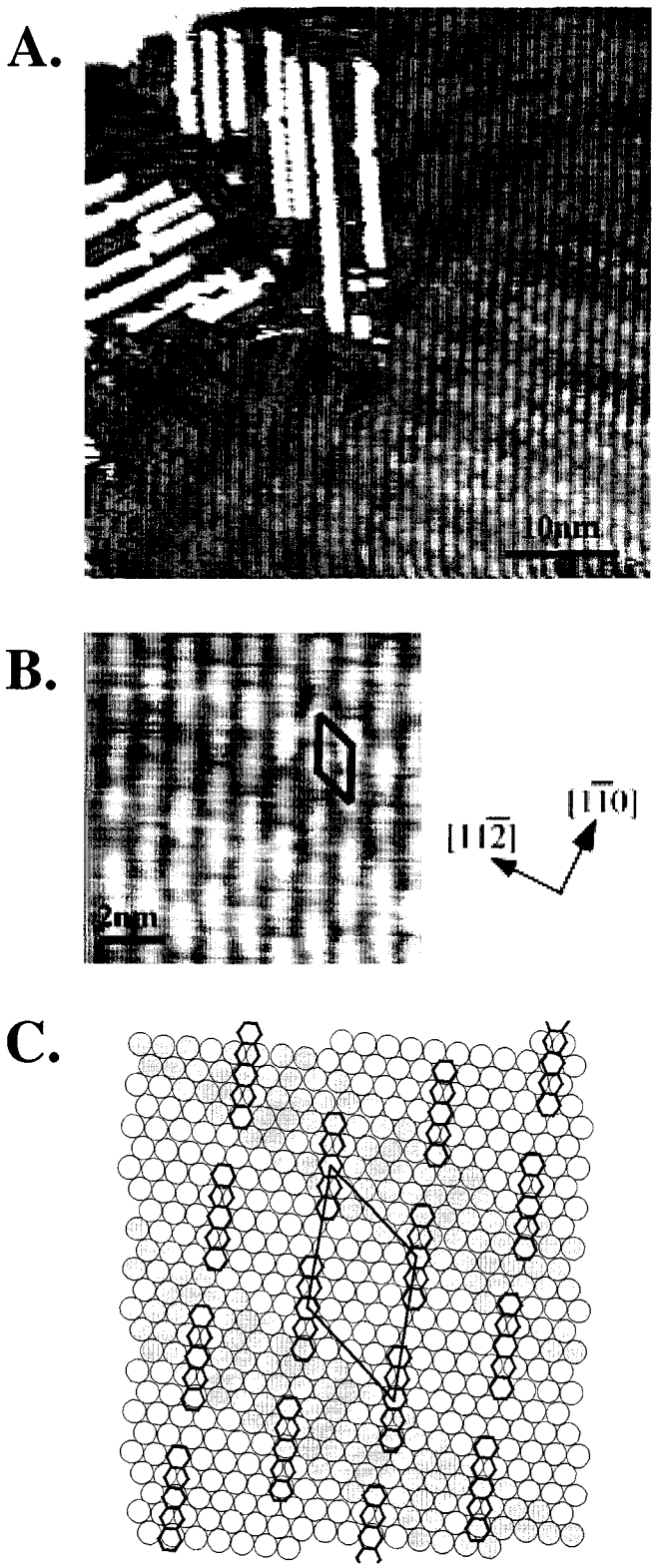

Figure 3.4: (A) A 50 × 50 nm STM image with 3 different pentacene polymorphs. The upper left contains side-by-side row pentacene. The lower left contains the type 1 low-coverage structure. Molecules on the right side of the image are the type 3 structure. (-2.0 V, 0.3 nA) (B) A 9.9 × 10.1 nm zoom in of the type 3 structure with the pentacene unit cell drawn. (C) A proposed model of the $2\sqrt{7} \times \sqrt{37}$ type 3 structure.

The type 4 low-coverage ordering is shown in the 17 × 48 nm STM image of Figure 3.5A where the left half of the image is the type 1 structure and the type 4 structure is seen on the right side. The Au(111) reconstruction is present under both polymorphs with a reconstruction elbow located under the type 4 structure and perpendicular to the direction of the type 1 rows, as described above. To help clarify the pentacene orientation relative to the Au(111), a close-up STM image is shown in Figure 3.5B from a location in Figure 3.5A where the Au reconstruction is uniform. The pentacene unit cell is drawn in Figure 3.5B for clarity. The directional vectors are oriented to this zoomed in location and the model. End-to-end interactions between nearest neighbor molecules resulted in measured distances, center-to-center, of 18 ± 1 Å between end-on molecules and 13 ± 1 Å between side-on molecules, $\alpha = 113 \pm 3°$. The type 4 structure has been determined to have a $\sqrt{21} \times \sqrt{43}$ (13.2 × 18.9 Å) unit cell, $\alpha =$ 116.7°, with a theoretical packing density of 4.00×10^{13} molecules/cm^2. A model of this overlayer is shown in Figure 3.5C.

As discussed above, these type 1-4 structures were measured at submonolayer film thickness (~0.25 MLE). As seen in many of the figures of this report, multiple structures were often imaged in the same STM image with as many as 4 polymorphs coexisting in an area of 2500 nm^2. The interesting end-to-end interaction between neighboring pentacene molecules in these low-coverage structures is unexpected. Crystal

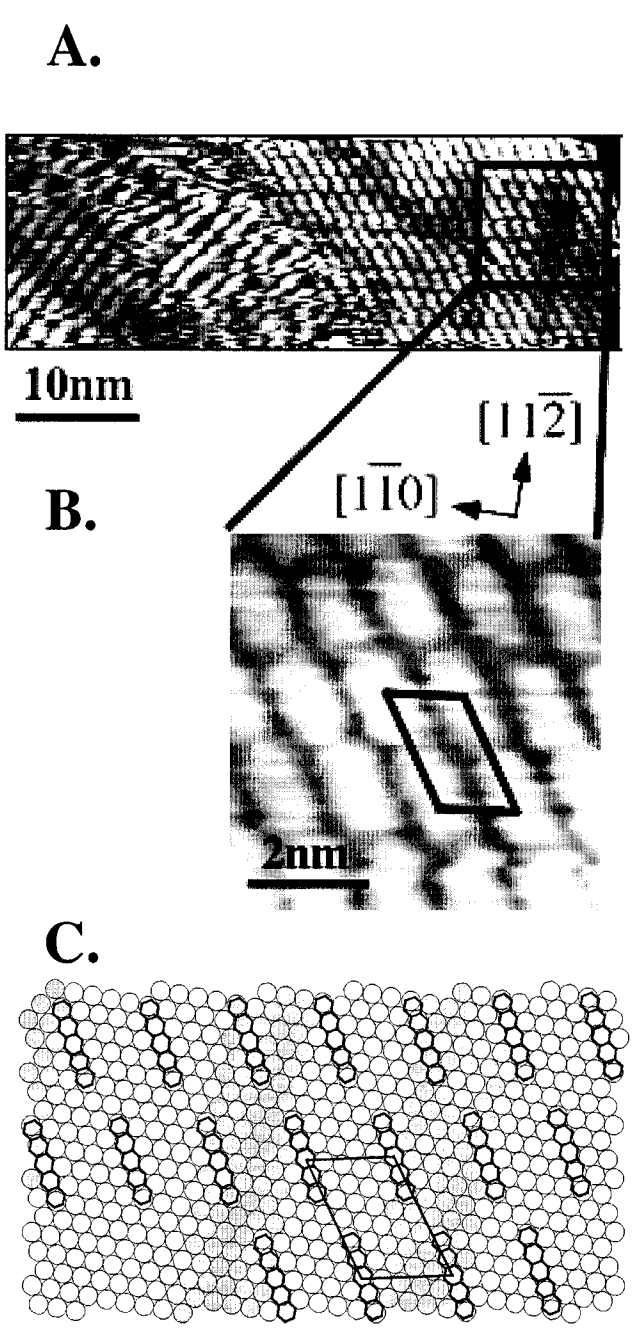

Figure 3.5: (A) A 17 × 48 nm STM image of two different pentacene polymorphs on Au(111). The left half of the image contains the type 1 pentacene structure with the Au reconstruction running perpendicular to the pentacene molecules. On the right side of the image is the type 4 polymorph with a Au reconstruction elbow visible. (-2.0 V, 0.3 nA) (B) A 6.1 nm × 6.1 nm zoom in from the upper right of Figure 3.5A. The directional vectors are consistent for this location (Figure 3.5B location) and the proposed model. The pentacene unit cell has been included. (C) A proposed model of the $\sqrt{21} \times \sqrt{43}$ type 4 ordering.

structures of pentacene show the molecules aligning in a herringbone structure with nearest neighbor molecules in a side-by-side fashion and layers of the molecules tilted to facilitate edge-face interactions.[*10-12*] Pentacene polymorphs on Au(111) have yielded structures similar to these bulk orientations, as was observed in previous STM experiments.[*4*] In those experiments, pentacene films with a thickness of ~0.75 MLE were found to form rows with nearest neighbors having side to side interactions. At these higher coverages, side-by-side rows allow for an increased overlayer packing density on the Au(111). Statistical analysis of the row spacings revealed the formation of 3 basic orientations of side-by-side rows, type A ($2 \times 3\sqrt{3}$), type B ($2 \times 2\sqrt{7}$), and type C ($2 \times \sqrt{31}$) unit cells. Rows separated by one or more additional Au atom were also observed, increasing the area covered by each unit cell.

Coverages close to one monolayer were investigated by depositing approximately 10 Å of pentacene on the gold surface and annealing the sample at 60 °C for around 15 min. After annealing, the STM was used to investigate the ordered structures at room temperature. TPD was subsequently performed to estimate the thickness of the remaining film. STM experiments revealed that multilayer films remained on parts of the surface after annealing, however large areas of the surface showed only the annealed monolayer. A 300 nm × 300 nm STM image, shown in Figure 3.6A, demonstrates the types of structures seen on an annealed pentacene film on the gold surface. A zoom-in of

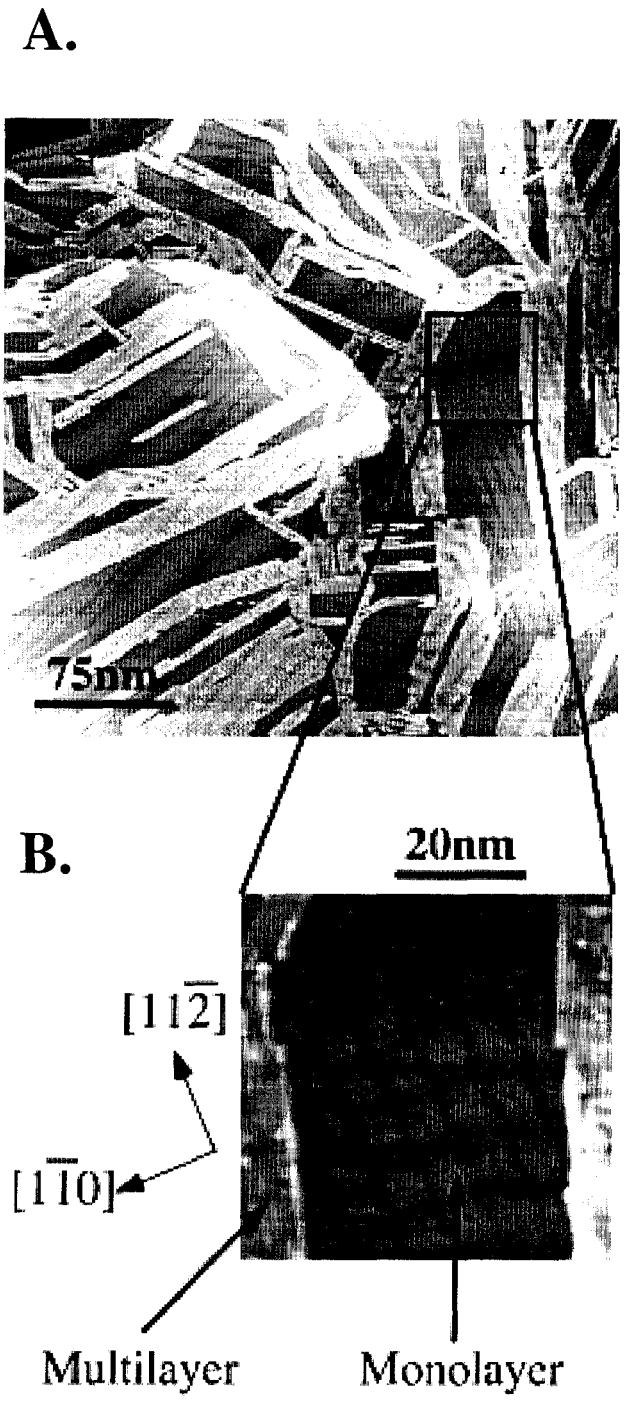

Figure 3.6: (A) A 300 nm × 300 nm STM image of an annealed pentacene film on Au(111). A screw dislocation is observed coming from the center of the image in a counterclockwise direction. The Au 23 × $\sqrt{3}$ reconstruction is imaged through both the first and second layer pentacene structures. (-2.0 V, 0.3 nA) (B) A zoom of the indicated region from Figure 3.6A with corresponding directional vectors. Bright second layer rows of pentacene molecules are shown with a monolayer of pentacene molecules visible throughout the image.

a region from Figure 3.6A is shown in Figure 3.6B. The directional vectors for the Au(111) are included for the zoomed-in region and the locations of the monolayer and multilayer pentacene structures are highlighted. The Au(111) 23 × √3 reconstruction is observed throughout the image, through both the first (darker regions) and second layer (brighter areas) pentacene structures. A Au(111) screw dislocation begins in the center of the image, rotating out from the origin in a counterclockwise direction. The bright rows of pentacene molecules are single molecule width rows with the molecules aligning side-by-side. Upon zooming in on the monolayer covered areas, two pentacene polymorphs were identified. The first structure identified was the 2 × 2√7 (5.76 × 15.3 Å), α = 79.1°, structure with a theoretical packing density of 1.14×10^{14} molecules/cm^2, originally identified as the type B unit cell in our previous paper where the initial pentacene coverage was 0.75 MLE but annealing was not performed.[*4*] The type B monolayer is shown in the STM image in Figure 3.7A where the gold reconstruction can clearly be seen under the monolayer structure. The measured center-to-center distances between the pentacene molecules in the overlayer are 6 ± 1 Å for the side-to-side molecules and 15 ± 1 Å for molecules aligned end-to-end (α = 79 ± 3°). A proposed model of the type B monolayer is shown in Figure 3.7B. The other monolayer unit cell was also previously identified in submonolayer films (~0.75 MLE) as the type C unit cell.[*4*] This type C structure was identified as a 2 × √31 (5.76 × 16 Å), α = 69.0°, unit cell with a packing

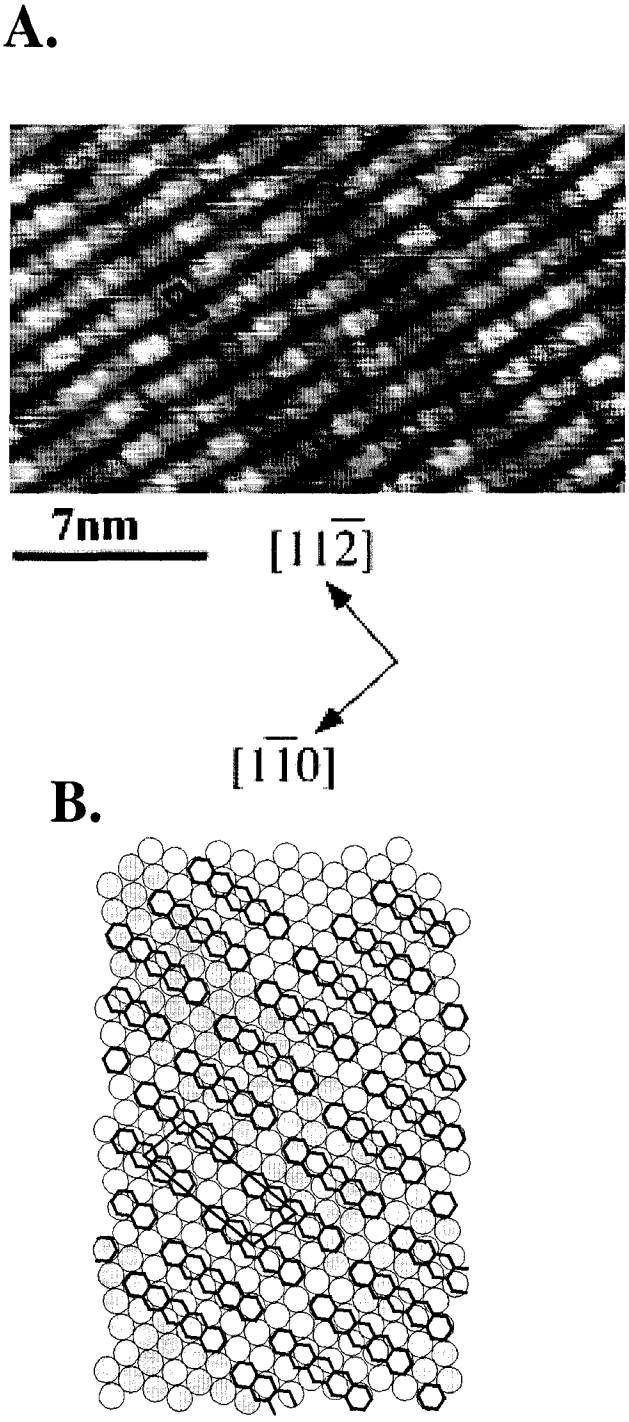

Figure 3.7: (A) The type B monolayer is shown in the constant current STM image. (-2.0 V, 0.5 nA) (B) A proposed model of the 2 × 2$\sqrt{7}$ type B monolayer structure which has been aligned with the STM image.

density of 1.09×10^{14} molecucles/cm^2. In Figure 3.8A, an image of the type C monolayer structure is shown in a 12.4 nm × 12.4 nm STM image. The measured overlayer distances of the pentacene molecules are 15 ± 1 Å for the end-to-end molecules and 6 ± 1 Å for the side-to-side molecules (α = 75 ± 3°). An averaged image of this type C structure is shown in Figure 3.8B, as produced by SPIP software. The overlayer unit cell has been drawn in to clarify the pentacene positions. A model aligned with the STM images and showing the rows of pentacene molecules in the type C monolayer is presented in Figure. 3.8C. The fact that these two unit cells predominate on the annealed monolayer film indicates they are most likely the stable configurations for a monolayer structure. Table 3.1 summarizes all of the ordered monolayer and submonolayer structures described in this report. The labeling of these structures is somewhat arbitrary but numbers are used for the low-coverage structures ($< 8 \times 10^{13}$ cm^{-2}) with end-to-end interactions and letters are used for the high-coverage structures ($> 8 \times 10^{13}$ cm^{-2}) with side-on interactions.

It is interesting to compare the observed monolayer structures with the molecular packing in pentacene crystals. The molecular packing along the (100) plane of the crystal is very similar to the structure of the type B monolayer. Figure 3.9 shows 4 × 4 unit cells of the (100) face of the bulk pentacene structure from a crystal structure determination (compare with Figure 3.7B).[*11*] It is important to note that the molecules in Figure 3.9

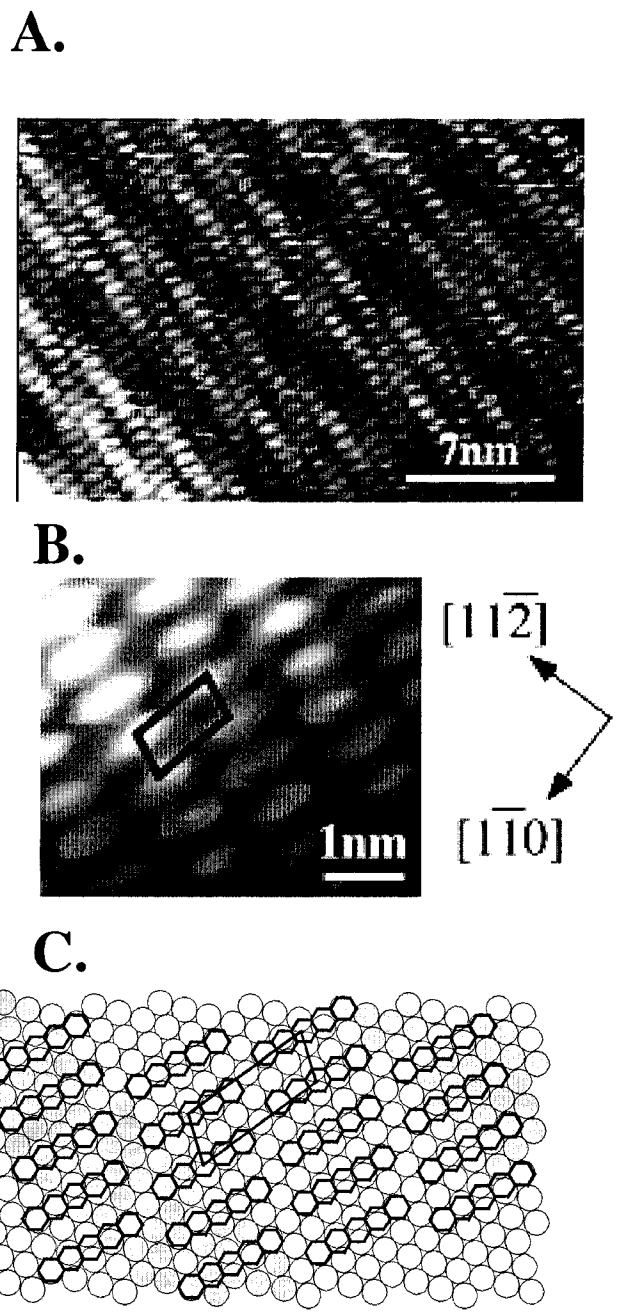

Figure 3.8: : (A) A 27 × 27 nm STM image of the type C monolayer structure on Au(111). (-2.0 V, 0.4 nA) (B) An averaged STM image from Figure 3.8A with pentacene unit cell added. (C) A model of the 2 × $\sqrt{31}$ type C monolayer aligned with directional vectors as indicated.

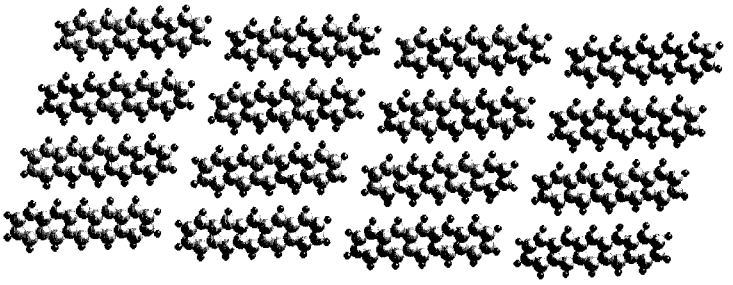

Figure 3.9: 4 × 4 unit cells of the crystalline pentacene structure at the (100) plane. These molecules are not coplanar with the (100) plane, however they have a very similar structure to that of the type B monolayer.

are not completely coplanar with the (100) plane as they are expected to be on the Au surface. Even so, the unit cell distances of 6.1 × 16.0 Å and unit cell angle of 78° are within experimental error of the type B monolayer distances 6 ± 1 Å × 15 ± 1 Å and angle 79 ± 3°. The type C monolayer structure does not resemble the bulk structure of either pentacene polymorph and therefore its existence is attributed to a favorable adsorbate-substrate interaction. Epicalc[*13*] was used to investigate the presence of any epitaxial interactions between these monolayer structures and the reconstructed Au(111) substrate. The type B monolayer was found to be coincident with the reconstructed substrate where as the type C monolayer was found to be incommensurate with the reconstructed Au(111) surface. The coincidence of the type B monolayer and its similar structure to that of bulk pentacene, suggests that it could be the template layer for the direct formation of bulk pentacene crystallites with the (100) planes parallel to the Au(111) substrate.

Investigation of the pentacene film on Au(111) at greater than monolayer coverage led to the discovery of a unique widely spaced periodic (WSP) row structure.[*6*] Rows made up of tilted pentacene molecules formed with a periodic center-to-center distance of 61 ± 5 Å, an unusually large separation as it is significantly larger than the width of the pentacene molecules. STM images after deposition of ~1.5 MLE of pentacene revealed WSP rows covering the entire investigated surface. The nonbulk like,

incommensurate type C monolayer was found to lie below these unique structures with the WSP rows traveling across the surface coincident with the monolayer structure. The large spacing of the WSP rows was attributed to the incommensurate type C monolayer forming defects or offsets allowing for better alignment with the reconstructed surface. Epicalc determined that the large WSP overlayer was coincident with the reconstructed substrate. Details of this structure are published elsewhere.[*6*]

Two monolayer equivalents or 10 Å pentacene films were also imaged with STM. Observation of the thicker films was more difficult because of mobile, less strongly bound, pentacene molecules in the second layer, thus leading to significant noise and streaking in the STM images. However, some observations revealed that the WSP row molecules were being covered with another layer of side-by-side pentacene rows, similar to the structures found in the monolayer films. While the precise alignment of the pentacene molecules was not determined in these films, an additional layer of pentacene molecules aligning with their aromatic plane parallel to the substrate is similar to what would be expected of crystalline ordering. This additional layer would generate parallel-tilted-parallel herringbone structure similar to the crystalline pentacene structure growing from the (100) plane on the Au(111).

High-resolution STM images of pentacene in the side-by-side row structures commonly showed individual molecules as having more facile tunneling at either end of

the molecule. An excellent example of this was shown in a previously published high-resolution STM image[*14*] where side-by-side pentacene rows clearly show each pentacene molecule consists of bright lobes at either end of the molecule. Similar high-resolution images were also frequently obtained during the studies reported herein with sample biases ranging from –2 to 2 V. The lack of a strong voltage dependence on the molecular contrast suggests that pentacene molecular orbitals do not dominate the tunneling during the imaging process. The angle of the pentacene rows and molecule directions measured with respect to the Au(111) $23 \times \sqrt{3}$ reconstruction and the size of the pentacene molecule relative to the Au lattice, suggest that the interaction between the Au substrate atoms and pentacene dominates the STM image contrast. Although we do not have direct evidence of this interaction, many of the models presented in this report show the pentacene molecule aligning with the two end acene rings on atop sites of the Au lattice, while the middle ring of the molecule resides above a 2-fold site. If this alignment is correct, we believe there will be more facile tunneling to the region of the pentacene molecules that are above the atop sites of the Au lattice while the middle of the molecule will not interact as strongly with the substrate as it straddles a Au 2-fold site. A similar double-lobed STM contrast mechanism has been proposed for very low coverages of pentacene on a Si(100) 2×1 surface.[*15*] Higher-resolution images of the low-coverage pentacene structures on the Au(111) surface do not show a double-lobed

structure, instead showing uniform tunneling across the entire molecule. We believe this is due to thermal motion of the molecules in the low packing density, end-on-end, structures. The space around each pentacene molecule in the lower density films allows limited rotational and lateral motion that prevents submolecular resolution of the molecules at room temperature and results in averaging of the tunneling current across the molecule. Although the angles of the substrate reconstruction, relative to the direction of the pentacene molecules, indicates the molecules are lining up with the substrate as discussed above, motion of the pentacene causes a blurring of the molecules during the STM imaging process and thus the molecules appear larger than expected (for example see Figure 3.3A). Low-temperature STM studies are being attempted to further understand the Au-pentacene interactions and image contrast mechanisms in these low-coverage films.

A summary of the many structures identified and the coverages at which they were imaged is presented in Table 3.1 along with a film thickness vs structure chart shown in Figure 3.10. The bottom axis of Figure 3.10 is the pentacene film thickness in angstroms, as determined by quartz crystal microbalance, and monolayer coverage as confirmed from STM and TPD measurements. The four low-coverage structures, types 1-4, all had end-on-end nearest neighbor interactions. Whereas the higher-coverage side-by-side row structures are the unit cells of type A-E. Type D unit cells have 2 Au atoms

Table 3.1: Modeled (bold) and Experimentally Determined Unit Cell Information for Submonolayer and Monolayer Pentacene Structures on Au(111)

Structure	a	b	α	Density (mlcs/cm^2)	Unit Cell Symmetry
Type 1	**17.3 Å**	**32.4 Å**	**87.5°**	**3.57 × 10^{13}**	p1
	18±1 Å	32±1 Å	86±3°		
Type 2	**15.0 Å**	**18.0 Å**	**106.1°**	**3.70 × 10^{13}**	p2
	15±1 Å	18±1 Å	105±3°		
Type 3	**15.3 Å**	**17.5 Å**	**52.8°**	**3.73 × 10^{13}**	p2
	13±1 Å	17±1 Å	51±3°		
Type 4	**13.2 Å**	**18.9 Å**	**116.7°**	**4.00 × 10^{13}**	p2
	13±1 Å	18±1 Å	113±3°		
Type A	**5.76 Å**	**15.0 Å**	**90°**	**1.16 × 10^{14}**	p2mm
Type B	**5.76 Å**	**15.3 Å**	**79.1°**	**1.14 × 10^{14}**	p2
	6±1 Å	15±1 Å	79±3°		
Type C	**5.76 Å**	**16.0 Å**	**69°**	**1.09 × 10^{14}**	p2
	6±1 Å	15±1 Å	75±3°		
Type D	**5.76 Å**	**18.0 Å**	**76.1°**	**9.64 × 10^{13}**	p2
Type E	**5.76 Å**	**20.8 Å**	**73.9°**	**8.35 × 10^{13}**	p2

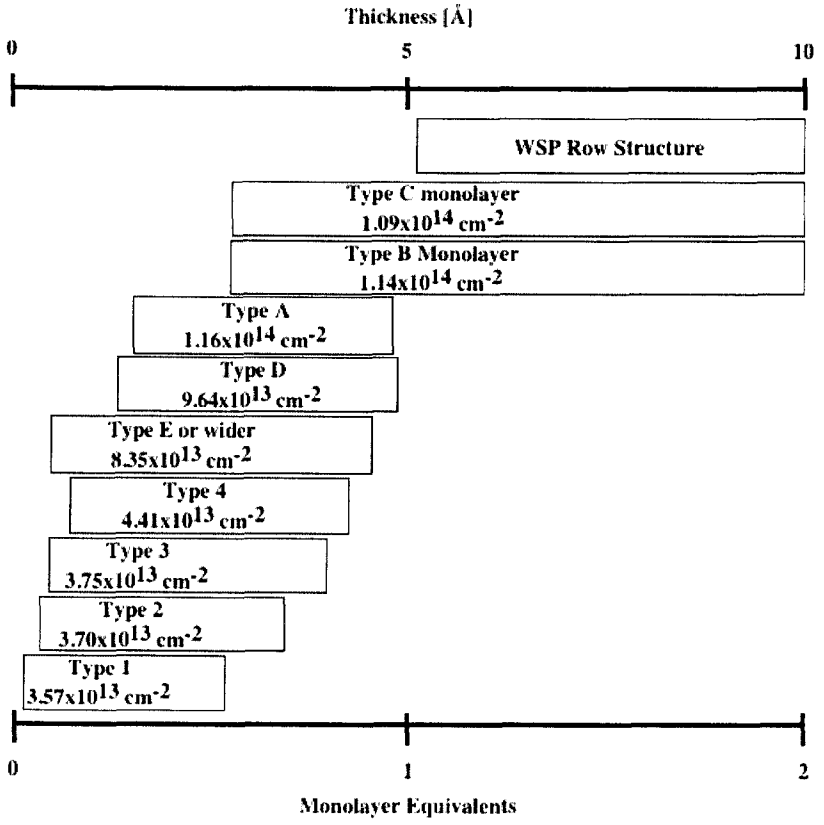

Figure 3.10: A film thickness vs. structure diagram of the ordered pentacene polymorphs formed on Au(111). The bottom axis is the coverage of the pentacene molecules in monolayer equivalents and angstroms, as determined by quartz crystal microbalance.

between side-by-side rows and type E unit cells have more than two Au atoms between rows; for more information on the type A, D, and E structures see ref 10. Type E or wider (many Au atoms between rows) are the first side-by-side row structures found at lower coverages. Increasing the film thickness forces the rows together and generates additional side-by-side rows until a monolayer film is produced. Additional deposition of pentacene generates the tilted molecule WSP rows that cover the entire surface. Continued deposition of pentacene, around two monolayers, covers the WSP rows with a structure that appears to be similar to the side-by-side rows of the monolayer.

It is worth noting the unexpected richness of observed structures that have been imaged at this interface. The surprising number of ordered structures formed by this nonpolar, polyacene molecule was not expected on the relatively inert Au surface. The structural change between the end-on to side-on interactions in the film results in a sudden two and a half fold increase in the packing density between the low coverage structure (type 4) and the monolayer structures (type B and C), see Table 3.1. While two distinct types of structures were imaged (end-on and side-on), the many slight variations observed suggest a small energy difference or concentration dependence between those structures. The existence of pentacene 3D crystalline polymorphs also points out that subtle structural differences are possible when packing molecules with primarily van der Waals interactions.[*10, 11*] These results indicate the interesting and complex nature of

this technologically interesting interface and the need for additional investigation into these types of systems.

3.5 Summary:

The coverage-dependent ordered structures of pentacene molecules on Au(111) have been investigated. Temperature-programmed desorption was used to determine the presence of two distinct binding environments -the monolayer and multilayer- with binding energies of 110 and 106 kJ/mol respectively. TPD was also used to calibrate the coverage of the pentacene film where 5 Å was determined to be the thickness of one monolayer. Scanning tunneling microscopy was utilized to image the ordered structures of pentacene on the reconstructed Au(111) surface. At low coverages of pentacene, four end-to-end nearest neighbor ordered structures were identified. Increasing the pentacene coverage generated structures where the higher packing density side-by-side rows became dominant as film thickness approached one monolayer. Two different monolayer structures were identified after annealing films with greater than a monolayer coverage. From these two monolayer structures, the type B form was found to have similar parameters to the bulk (100) form of pentacene and was coincident with the reconstructed substrate. The type C form was found to be incommensurate with the reconstructed Au(111) and had geometries substantially different than that of the bulk pentacene structures. Evidence for the formation of defects or offsets in the type C film to allow for

a coincident interaction is demonstrated through the adhering of additional pentacene molecules at these sites and the formation of the WSP rows. The large number of ordered structures formed by this nonpolar, aromatic pentacene molecule on the relatively unreactive Au(111) substrate is quite surprising and underscores the complexity of this heterojunction.

Acknowledgements:

This work is supported by the Department of Energy under contract DE-F603-96ER14625.

References:

[1] M. A. Baldo, S. R. Forrest, Phys. Rev. B **64**, 85201 (2001).

[2] C. D. Dimitrakopoulos, S. Purushothaman, J. Kymissis, A. Callegari, J. M. Shaw, Science **283**, 822 (5 Febuary 1999, 1999).

[3] P. G. Schroeder, C. B. France, J. B. Park, B. A. Parkinson, J. Phys. Chem. B **107**, 2253 (2003).

[4] P. G. Schroeder, C. B. France, J. B. Park, B. A. Parkinson, J. Appl. Phys. **91**, 3010 (2002).

[5] S. Lukas, G. Witte, C. Wöll, Phys. Rev. Lett. **88**, 028301 (2002).

[6] C. B. France, P. G. Schroeder, B. A. Parkinson, Nano Lett. **2**, 693 (2002).

[7] The variable temperature capabilities of this instrument were not utilized during these experiments. All STM images in this report were produced at room temperature.

[8] The gold film thickness on the mica is estimated at a few microns.

[9] P. A. Redhead, Vacuum **12**, 203 (1962).

[10] T. Siegrist, C. Kloc, J. Schön, B. Batlogg, R. Haddon, S. Berg, G. Thomas, Angew. Chem. Int. Ed. **40**, 1732 (2001).

[11] R. B. Campbell, J. M. Robertson, J. Trotter, Acta. Cryst. **14**, 705 (1961).

[12] R. B. Campbell, J. M. Robertson, J. Trotter, Acta. Cryst. **15**, 289 (1962).

[13] Epicalc is a computer program that performs epitaxy calculations utilizing an analytical algorithm. Epicalc was developed by the Ward group in the department of Chemical Engineering at the University of Minnesota and is available at http://www.wardgroup.umn.edu/software.html

[14] Figure 4 of reference 4.

[15] M. Kasaya, H. Tabata, T. Kawai, Surf. Sci. **400**, 367 (1998).

Chapter 4: Direct Observation of a Widely Spaced Periodic Row Structure at the Pentacene / Au(111) Interface using Scanning Tunneling Microscopy

Published: C. B. France, P. G. Schroeder and B. A. Parkinson, Nano Lett., **2,** 693, (2002).

4.1: Abstract:

The transition from surface to bulk pentacene at the Au(111) interface will have important implications for the mechanism of carriers transported across the interface. STM observations of pentacene molecules on the Au(111) surface, at more than a monolayer coverage, revealed periodic rows of molecules spaced 61±5Å apart. These widely spaced periodic rows consist of flat and edge-on molecules aligned with the initial

layer of pentacene. Commensuration with the surface and characteristic bulk pentacene-pentacene interactions drive the formation of this unique structure.

4.2: Experimental Report:

The ability to assemble organic molecules on surfaces into nanometer size structures, such as one-dimensional wire-like arrangements, has technological implications. One-dimensional structures of atoms and molecules have been produced by substrate mediated assembly at steps[*1*] and other surface defects.[*2*] Molecules interacting with each other[*3*] and/or the substrate through functional groups[*4, 5*] have also been used to form ordered structures on a surface terrace. Substrate mediated ordering has also been demonstrated using the reconstruction of the Au(111) surface.[*3, 6, 7*] These molecular systems can form large two-dimensional domains or one-dimensional rows. These self-assembled structures typically have repeating dimensions on the order of a length of one or two molecules. There have been very few reports of an assembly of atoms or molecules into repeating patterns separated by more than one or two molecular lengths.[*8*]

Highly purified pentacene single crystals have been shown to have one of the highest carrier mobilities measured for an organic semiconductor.[*9, 10*] These high

mobilities make pentacene a promising material for use in thin film transistors[*11, 12*] and organic photovoltaic devices.[*13-15*] Gold is commonly used as an electrical contact to the organic semiconductor in these devices. Our previous studies of this interface revealed the existence of a large interface dipole barrier and a rich variety of ordered pentacene structures.[*16*] During the studies of the pentacene/Au(111) interface we observed widely spaced periodic (WSP) rows of pentacene molecules, with 61Å separation. These widely spaced periodic structures will be described herein.

Experiments were performed in a commercial Omicron Multi-probe® ultrahigh vacuum system described previously.[*16, 17*] The Au(111) sample was produced by depositing a ~1μm thick gold film onto a mica substrate at 300°C. The Au(111) surface was cleaned with repeated sputter and anneal cycles until x-ray photoelectron spectroscopy verified chemical purity and scanning tunneling microscopy (STM) revealed the characteristic herringbone 23 × $\sqrt{3}$ reconstruction.[*18*] Pentacene was deposited onto the Au(111) surface in an attached deposition chamber from a resistively heated boron nitride crucible and monitored with a Leybold® quartz crystal microbalance. The pentacene film thickness for these investigations was between 5.5 – 7Å. The Au substrate was held at room temperature during the deposition. The STM images were obtained in a constant current mode with sample biases ranging from –2.0 to

+2.0 V and tunneling currents between 0.1 and 0.5 nA. A background plane fit or slope correction was the only post collection processing applied to the images.

Previous STM experiments with pentacene on the Au(111) surface have shown that at approximately one monolayer coverage, rows of molecules are formed.[*16*] These structures are formed when pentacene molecules line up in a side-by-side orientation. The row structure with a $2 \times \sqrt{31}$ unit cell, labeled type C in ref 16, was found to be one of the predominate structures formed by pentacene at monolayer coverage. Single molecule wide rows, of or similar to the monolayer structure described above, will be referred to as single molecular width (SMW) rows throughout this report.

Upon deposition of slightly more than a monolayer of pentacene[*19*] (film thickness of 5.5Å), STM revealed a new surface structure. Figure 4.1A shows this new structure across the left side of the image. The right side of the image is composed of SMW rows. The separation between the middle of the large WSP rows is 61 ± 5Å, with the rows at the bottom of the image being spaced further apart than the rows at the top. Between the WSP rows, first layer SMW rows can be seen. These SMW rows run approximately 60° to the WSP rows and are parallel to the SMW rows on the right side of the image. The $23 \times \sqrt{3}$ reconstruction of the Au substrate can be seen through the overlayer and is oriented nearly perpendicular to the WSP row direction (Fig. 4.1A).

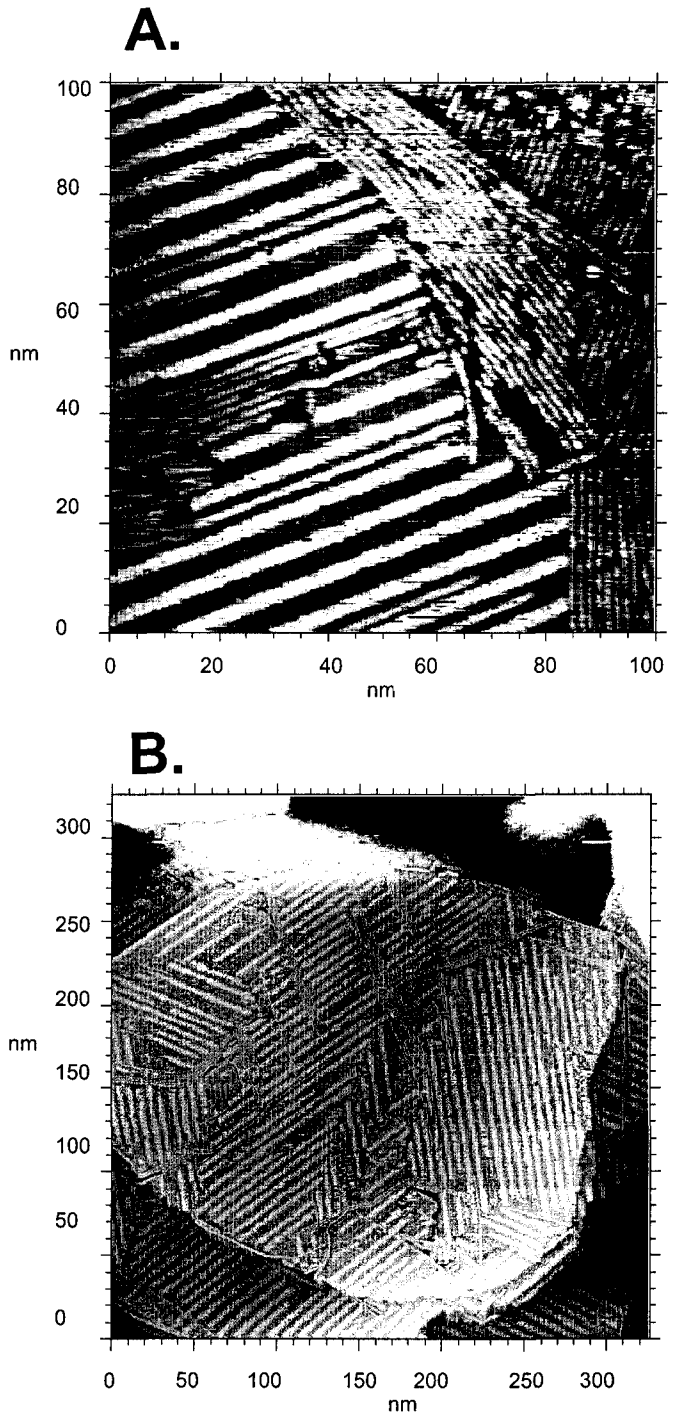

Figure 4.1: STM images of the widely spaced periodic (WSP) rows of pentacene molecules on the Au(111) surface. 5.5Å of pentacene was deposited in A) and the WSP rows are seen on the left side of the image. The 23 × $\sqrt{3}$ Au(111) reconstruction can be seen going nearly perpendicular to the WSP rows. B) Increased numbers of the WSP rows are observed with a 7Å pentacene film. Max z-height for image A) and B) are 0.198nm and 0.808nm respectively.

Pentacene adsorption does not lift the Au(111) reconstruction as is frequently observed with more strongly bound adsorbate molecules.[4] SMW row structures can also be seen running parallel and between the WSP rows within a second layer.

Deposition of an additional 1.5Å (total film thickness of 7Å) of pentacene results in the entire surface being covered with the WSP row structures. The 61Å center-to-center distance between the structures remains nearly constant at this higher coverage. Domains of these structures completely cover large Au (111) terraces as shown in the 325 × 325 nm STM image of Fig. 4.1B. The angles between the WSP rows in the different domains are 60 and 120°. Some second layer SMW rows can be seen on the center of the large Au terrace (Fig. 4.1B). These rows tend to run parallel to the WSP rows or between the domains.

Statistical analysis of 607 measurements, obtained from multiple images, determined the average separation of the repeating center-to-center distances between the WSP rows was 61 ± 5Å. Figure 4.2A shows a histogram of the center-to-center separation; the distances vary over ±10 Å but peak at 61 Å. One hundred sixty-one measurements of the width of the WSP rows at full width half maximum (FWHM) averaged 30 ± 5Å. Figure 4.2B is a histogram from 76 measurements showing that the

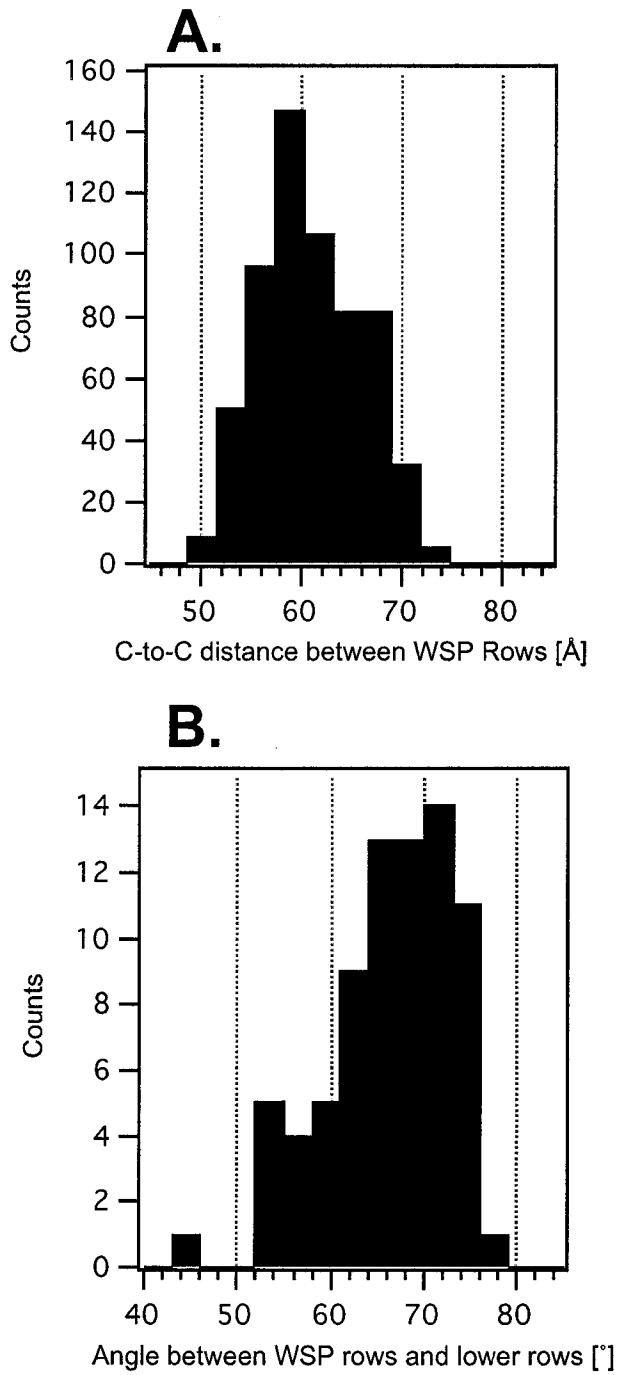

Figure 4.2: A) A Histogram of 607 measurements of the repeating center-to-center distance between the WSP rows, the average was found to be 61 ± 5Å. B) A histogram showing the measured angle between the WSP rows and the first layer SMW rows under them. The average angle was found to be 66 ± 7° from 76 measurements.

angle between the WSP rows and the first layer SMW rows under the WSP rows is 66 ± 7°.

The similar distance between the unit cell of the Au reconstruction (64Å)[*20*] and the WSP rows suggested that this row structure could possibly be templated by the substrate. STM images of the WSP rows, with the reconstruction visible under the pentacene overlayer, showed that the WSP rows were not aligning with the reconstruction (Fig. 4.1A). Furthermore, the fact that the angle between the lower layer SMW rows and the WSP rows was slightly larger than 60° indicates that the WSP rows were templated from the structure of the first layer. Epicalc[*21*] was used to investigate any commensuration between the Au(111) substrate and the pentacene overlayer. The 2 × $\sqrt{31}$ monolayer structure was not found to be coincident with the reconstructed substrate (unit cell I in Fig. 4.3A). We believe a commensurate interaction is achieved through the formation of defects or offsets in the monolayer structure. When the first pentacene molecules of the second layer are deposited, they preferentially adhere to these defect sites. A proposed model of this new pentacene layer is shown in figure 4.3A. The formation of a $\sqrt{31} \times \sqrt{(381)/2}$ (16 × 28.1 Å) (unit cell II in Fig. 4.3A) overlayer structure was found to be coincident with the reconstructed substrate. The angle between the substrate a1 lattice vector (23 Au atoms, see unit cell III in Fig. 4.3A) and the b1

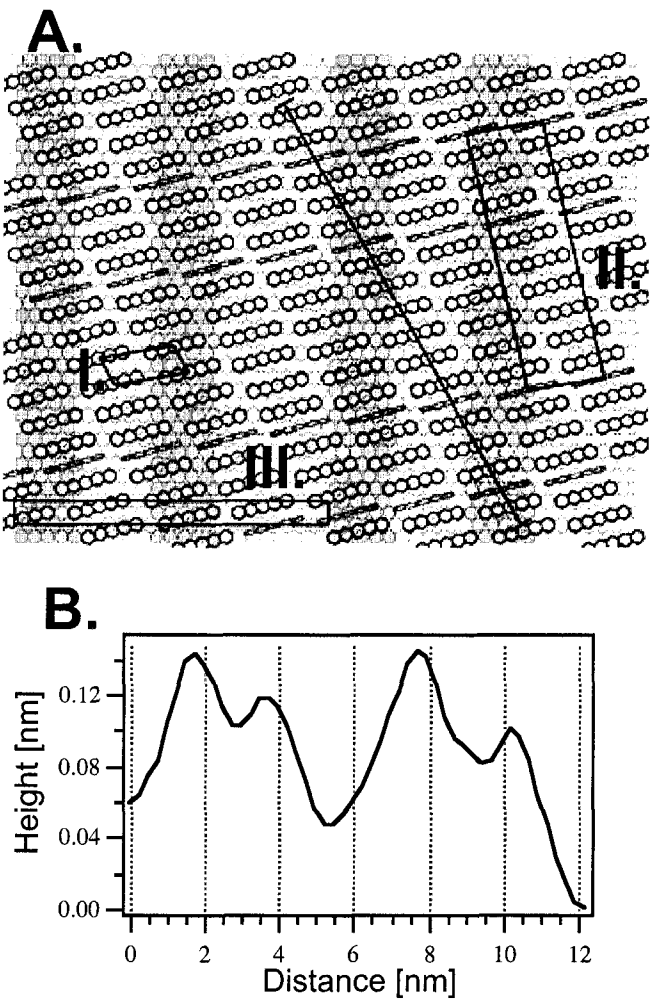

Figure 4.3: A) A proposed model for the WSP row structure. The three unit cells are I) the 2 × √31 pentacene monolayer SMW structure, II) the √31 × √(381)/2 WSP row structure and III) the 23 × √3 reconstructed Au surface (the dark Au atoms represent the location of the reconstruction solitons). A line is also drawn on the model that represents the placement of the STM line profile in 3B. B) A line profile taken from an STM image that shows the double lobed structure of the WSP rows.

overlayer vector ($\sqrt{31}$ Au atoms, see unit cell II in Fig. 4.3A) was calculated to be 9°, whereas the angle is predicted to be 8.95° in the model.

Cross sections of high-resolution images have shown that the WSP rows are comprised of a pair of rows (see Fig. 4.3B) and since the FWHM of the WSP rows is almost two pentacene molecular lengths, (30 ± 5 Å) it is expected that the width of each WSP row be composed of a pair of molecules. The paired row structure in combination with the angles between the WSP and SMW rows, discussed above, indicates that the molecules in the WSP rows are aligned with the pentacene molecules of the first layer. At present, the reason for the formation of a paired row is unclear, however the formation of a coincident overlayer appears to take place by pentacene molecules adhering to defects in the first layer and forming the WSP rows. Tilting of the WSP row molecules to form a herring bone structure is suspected because of the limited amount of space available for the defects. As we continue to investigate this structure, two possible orientations of the molecules in the WSP rows are conceivable. Providing the defects or offsets in the first layer are large enough, tilted pentacene molecules could be inserting through the first layer with an edge on interaction with the Au(111) surface. The WSP molecules could also behave as a second layer structure where the pentacene molecules are tilted over the defect sites of the first layer to maximize edge/face interactions. These

interactions are similar to those in the herringbone structure that is prevalent in the bulk crystal structure[*22-24*]. The possibility of pentacene molecules neighboring the WSP rows tilting can not be ruled out, indicating these periodic rows could be a transition to a bulk pentacene structure.

A widely spaced periodic row structure formed by pentacene molecules on the Au(111) surface has been observed. This unique structure consists of rows of paired molecules spaced approximately 61Å apart. From careful analysis of the STM images and calculations of possible commensurate structures using Epicalc, we believe the formation of these WSP rows takes place because of the total free energy gain due to commensurate growth on the substrate and bulk pentacene-pentacene interactions. The many structures formed by pentacene on the Au(111) surface at different coverages point to the complexity of this important interface. A detailed study of the many coverage dependent structures will be presented elsewhere.[*25*]

References:

[1] M. Zack, K. Ng, R. Penner, Science **290**, 2120 (2000).

[2] T. Yokoyama, S. Yokoyama, T. Kamikado, S. Mashiko, J. Chem. Phys. **115**, 3814 (2001).

[3] M. Bohringer, K. Morgenstern, W.-D. Schneider, R. Berndt, F. Mauri, A. De Vita, R. Car, Phys. Rev. Lett. **83**, 324 (1999).

[4] M. Dishner, J. Hemminger, F. Feher, Lang. **13**, 2318 (1997).

[5] M. E. Stawasz, D. L. Sampson, B. A. Parkinson, Lang. **16**, 2326 - 2342 (2000).

[6] M. M. Dovek, C. A. Lang, J. Nogami, C. F. Quate, Phys. Rev. B **40**, 11973 (1989).

[7] D. D. Chambliss, R. J. Wilson, S. Chiang, Phys. Rev. Lett. **66**, 1721 (1991).

[8] K. Kern, H. Niehus, A. Schatz, P. Zeppenfeld, J. George, G. Comsa, Phys. Rev. Lett. **67**, 855 (1991).

[9] J. H. Schön, C. Kloc, B. Batlogg, Science **288**, 2338 (2000).

[10] J. H. Schön, C. Kloc, R. A. Laudise, B. Batlogg, Phys. Rev. B **58**, 12952 (1998).

[11] J. H. Schön, S. Berg, C. Kloc, B. Batlogg, Science **287**, 1022 (2000).

[12] J. H. Schön, C. Kloc, App. Phys. Lett. **78**, 3538 (2001).

[13] J. H. Schön, C. Kloc, E. Bucher, B. Batlogg, Nature **403**, 408 (2000).

[14] J. H. Schön, C. Kloc, B. Batlogg, App. Phys. Lett. **77**, 2473 (2000).

[15] J. H. Schön, C. Kloc, E. Bucher, B. Batlogg, Synth. Met. **115**, 177 (2000).

[16] P. G. Schroeder, C. B. France, J. B. Park, B. A. Parkinson, J. Appl. Phys. **91**, 3010 (2002).

[17] P. G. Schroeder, M. W. Nelson, B. A. Parkinson, R. Schlaf, Surf. Sci. **459**, 349 (2000).

[18] C. Wöll, S. Chiang, R. J. Wilson, P. H. Lippel, Phys. Rev. B **39**, 7988 (1989).

[19] STM and temperature programmed desorption were used to calibrate the pentacene coverage. One monolayer was determined to be approximately 5Å.

[20] U. Harten, A. M. Lahee, J. P. Toennies, C. Wöll, Phys. Rev. Lett. **54**, 2619 (1985).

[21] Epicalc is a computer program that performs epitaxy calculations utilizing an analytical algorithm. Epicalc was developed by the Ward group in the department of Chemical Engineering at the University of Minnesota and is available at http://www.wardgroup.umn.edu/software.html

[22] R. B. Campbell, J. M. Robertson, J. Trotter, Acta. Cryst. **14**, 705 (1961).

[23] R. B. Campbell, J. M. Robertson, J. Trotter, Acta. Cryst. **15**, 289 (1962).

[24] T. Siegrist, C. Kloc, J. Schön, B. Batlogg, R. Haddon, S. Berg, G. Thomas, Angew. Chem. Int. Ed. **40**, 1732 (2001).

[25] C. B. France, P. G. Schroeder, J. C. Forsythe, B. A. Parkinson, Langmuir **19**, 1274 (2003).

Chapter 5: Physical and Electronic Structure of *p*-Sexiphenyl on Au(111)

Published: C. B. France and B. A. Parkinson, Appl. Phys. Lett., **82**, 1194, (2003).

5.1 Abstract:

The electronic structure, adsorption energies, and molecular ordering of p-sexiphenyl (p-6P) films on Au(111) have been investigated with ultraviolet photoemission spectroscopy, temperature programmed desorption (TPD), and scanning tunneling microscopy (STM). Films up to 50 Å of p-6P were studied and a substantial interface dipole was measured (0.73 eV). Two distinct p-6P binding environments with heats of adsorption of 126 and 143 kJ/mol were observed using TPD. An unusual surface structure that contains alternating face and edge-on p-6P molecules was observed using

STM. A model similar to the bulk p-6P structure with alternating face and edge-on interactions is proposed.

5.2 Experimental Report:

The electronic structure and molecular organization of organic semiconducting compounds on metal electrodes may influence the efficiency of charge transfer in organic based devices.[*1*] We have been investigating the molecular ordering of small organic molecules on Au(111) films prepared on mica substrates which are used to simulate a contacting electrode. Our previous studies of the interface between Au(111) and pentacene demonstrated that a large interface dipole can be formed between a relatively unreactive metal substrate and an organic semiconductor. This interface also produced a rich variety of two-dimensional (2D) ordered structures that formed as the pentacene coverage was changed.[*2-5*] We report on another contact of interest for molecular electronics, the interface between p-sexiphenyl (p-6P) and Au(111).[*6-9*]

The Au film was deposited on mica using previously published methods. [*10, 11*] Chemical purity was confirmed with x-ray photoemission spectroscopy (XPS) and the presence of the characteristic $23 \times \sqrt{3}$ reconstruction on the pristine terraced surface as imaged with scanning tunneling microscopy (STM).[*12*] The molecular organic semiconductor *p*-sexiphenyl was evaporated onto the Au(111) substrate under ultrahigh vacuum (UHV) conditions from a Knudsen cell at a deposition temperature of 184 °C

with a deposition rate of 4 Å/min as monitored by a Leybold quartz-crystal microbalance. The interface was then analyzed *in situ* using XPS and ultraviolet photoemission spectroscopy (UPS),[*13*] an Omicron UHV variable temperature STM,[*14*] and a home-built temperature programmed desorption system that was previously described in detail.[*5*]

The electronic structure of the p-6P/Au(111) interface was determined with UPS using the He (I) line at 21.22 eV. The right-hand side of Fig. 5.1(a) shows UPS spectra with increasing p-6P coverage up to a 50 Å thick film, beginning with bare Au(111) at the bottom of Fig. 5.1(a). The left-hand side section of Fig. 5.1(a) shows the normalized high binding energy cutoff. A continuous increase in the high binding energy cutoff is observed between the clean gold substrate and a 5 Å p-6P film. A plot of the workfunction values, determined by subtracting the value of the high binding energy cutoff from the He (I) source energy (21.22 eV), verses p-6P film thickness is presented in Fig. 5.1(b). The initial workfunction value of the Au(111) film (5.18 eV) decreases to a value of 4.45 eV at 5 Å of p-6P coverage and then remains constant as the thickness of the film increases to 50 Å. The total work function shift of 0.73 eV corresponds to the value of the interface dipole barrier. The magnitude of the interface dipole is similar to that obtained in a previous investigation, however the gold substrate work function was significantly lower than that used in our experiments.[*15*]

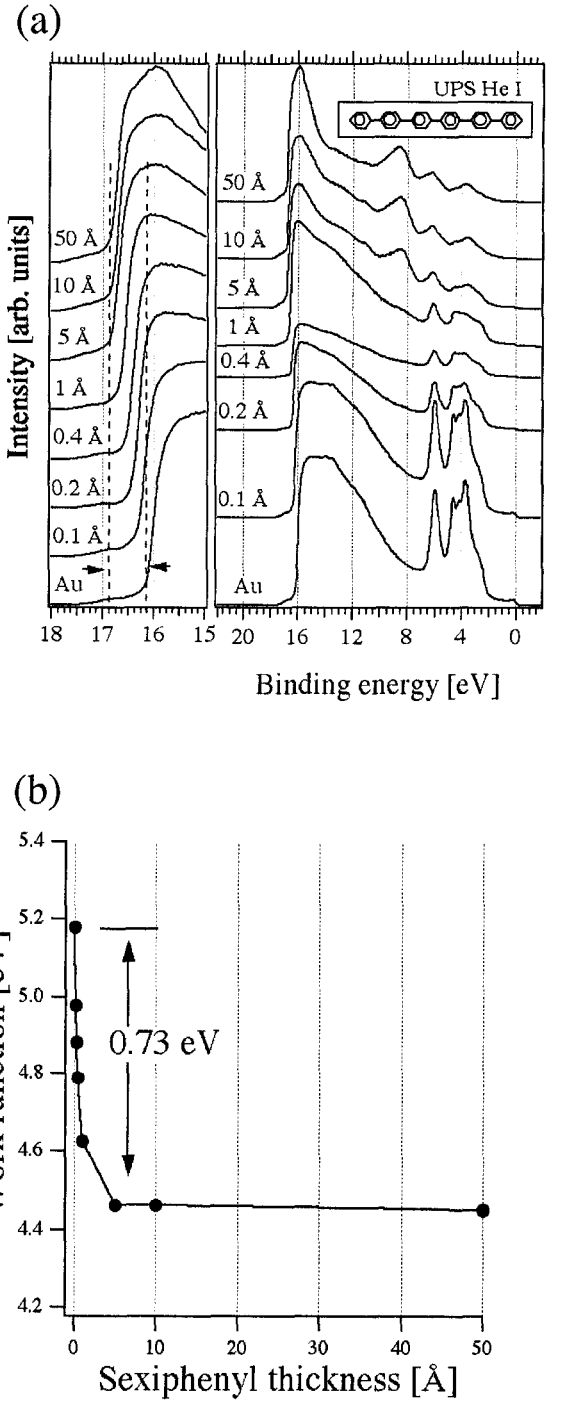

Figure 5.1: (a) He (I) UPS spectra of p-sexiphenyl deposited on Au(111). Full spectra with increasing p-6P coverage are shown on the right-hand side. The left-hand side is the normalized high binding energy cutoff that is used to determine the workfunction. (b) A graph showing the dependence of the work function on the p-6P film coverage.

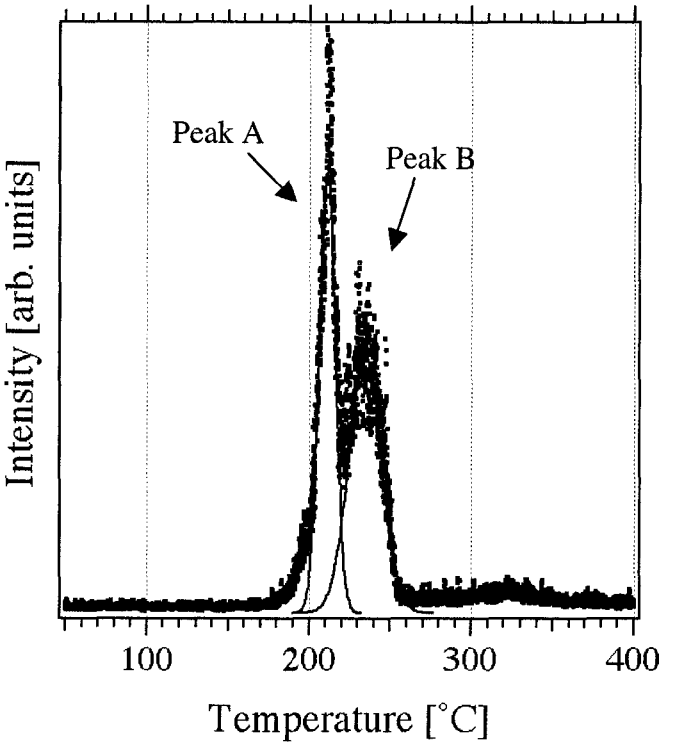

Figure 5.2: Temperature programmed desorption spectrum of a 50 Å p-6P film on Au(111). Peaks A and B have desorption temperatures of 211 and 234°C corresponding to binding energies of 136 and 143 kJ/mol, respectively.

The binding of p-6P to Au(111) was probed with temperature programmed desorption (TPD). The spectrum in Fig. 5.2 was obtained by heating a 50 Å p-6P film at a rate of 15 °C/min and using a quadrapole mass spectrometer[*16*] to detect the mass equivalent to the biphenyl fragment.[*17*] The biphenyl fragment mass to charge ratio was used because the molecular mass of p-6P exceeded the mass limit of the spectrometer.[*18*] The TPD spectrum shows two distinct peaks, peak A and B have desorption temperatures of 211°C and 234°C correlating to binding energies of 136 and 143 kJ/mol, respectively.[*19*] The sharpness of peak A indicates that the molecules in this binding environment have a narrow energy distribution and we assign this peak to mutlilayer/bulk p-6P. The higher binding energy peak B is much broader suggesting the peak originates from p-6P molecules interacting with the gold substrate. The presence of the substantial interface dipole suggests a strong interaction between the Au(111) and p-6P. The broad peak originates from the large number of possible binding sites on the substrate, i.e., steps, terraces, defects, etc.

STM was utilized to observe the structure of near monolayer films of p-6P on Au(111). A 48 × 48 nm STM image from a 2 Å p-6P film is shown in Fig. 5.3(a) where the p-6P molecules appear rectangular. The Au(111) herringbone 23 × $\sqrt{3}$ reconstruction is simultaneously observed with the organic overlayer in the STM image. Observation of the Au(111) reconstruction and organic molecules has also been noted at a similar,

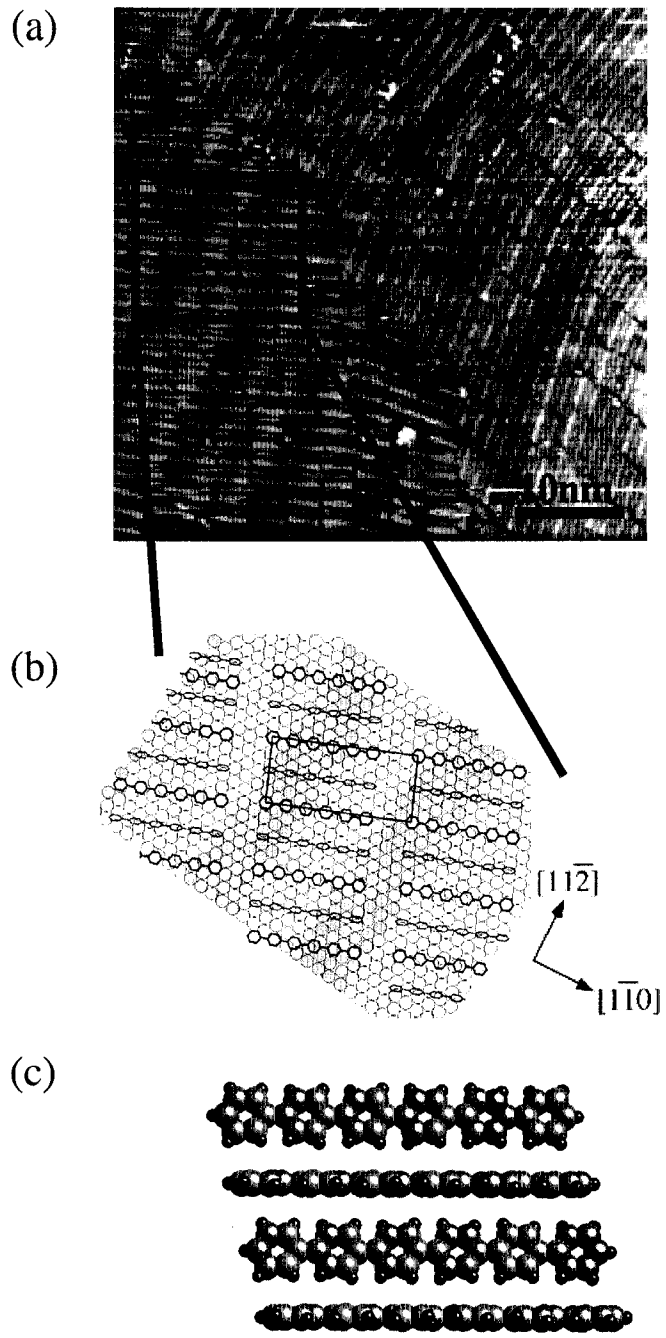

Figure 5.3: (a) A 48.3 × 48.7 nm scanning tunneling microscope image of p-6P on Au(111). The image shows the edge-face unit cell as alternating bright and dark molecules. Note the simultaneous imaging of the Au(111) reconstruction and p-6P molecules. (-0.5 V sample bias, 0.1 nA and 0.1 nm z-range). (b) A proposed model of the alternating edge-face structure. The model shows Au(111) with reconstruction (dark substrate circles are raised atoms) and p-6P molecules. Darker molecules represent the p-6P with its molecular plane parallel to the substrate and the lighter molecules are tilted upright. The model is aligned with a portion of (a) as shown. The directional vectors indicate the Au(111) orientation for both the model and STM image. (c). A space filling model of p-6P taken from crystallographic data (in Ref. 19).

pentacene-gold, interface.[5] Two different domains are observed, in Fig. 5.3(a), with a boundary aligning along a series of Au(111) reconstruction elbows and a 120° angle between the long axes of the molecules in these two domains. The image shows alternating bright and dark p-6P molecules within a unit cell where the distance between bright molecules is 14.6 Å and the other unit cell distance is 32.3 Å, corresponding to the length of the molecule. The unit-cell angle in this image varies depending on the location, as the overlayer appears to be influenced by the gold reconstruction, however it averages close to 90° ± 5°. The long axis of the molecules in the left-hand side domain are 65° ± 3° from the Au(111) reconstruction [$1\bar{1}2$], while the majority of the molecules in the right-hand side domain are aligned parallel to it.

A proposed model for the structure of the p-6P monolayer in the STM image of Fig. 5.3(a) is shown in Fig. 5.3(b). The model is aligned with the image, and the directional vectors correspond to both the image and model. The gold substrate atoms are represented by the light and shaded circles, where the shaded circles represent the elevated atoms of the reconstruction in Fig. 5.3(b). The p-6P molecules corresponding to the darker molecules in the STM image, are lying with their molecular plane parallel to the substrate whereas the molecules appearing brighter in the STM image are tilted upright. The exact location of the p-6P molecules with respect to the atoms of the Au(111) surface has not been directly observed, therefore the position of the p-6P

molecules over the gold atoms is based on their angular relationship with the reconstruction and the separation distance between molecules. The structure has a very unusual 2D unit cell containing two, non-symmetry related, molecules. The dimensions of the model unit cell are a = 14.4 Å, b = 32.5 Å and $\alpha = 91°$, in good agreement with the measurements. The side by side rows of p-6P molecules are aligned on the Au(111) surface with an angle of 30° from the reconstruction, $[11\bar{2}]$. This direction is symmetry equivalent [Au(111) has a hexagonal surface structure] to the $[1\,\bar{1}0]$ direction, thus molecular domains would be expected to differ by 60 or 120° and the long axis of the molecules would deviate from the $[11\bar{2}]$ reconstruction direction by approximately 60°/120° or be nearly parallel, as was observed in the domains of Fig. 5.3(a).. Examination of the p-6P bulk crystal structure [Fig. 5.3(c)] shows important edge-face interactions between p-6P molecules.[*20*] The 2D slice of the bulk structure has a higher packing density when compared to the film since the unit-cell distance between tilted molecules is only 9.5 Å, the long unit cell distance is 26.3 Å and the 2D unit cell angle is 104.2°. Not all the observed 2D structures produced by p-6P on Au(111) have his interesting alternating structure, as will be discussed in future reports.[*21*]

In summary, a substantial interface dipole has been measured between Au(111) and p-6P. TPD has resolved the bulk and surface binding environments. STM images have shown an interesting alternating edge-face structure where each unit cell has

alternating p-6P molecules lying flat on the substrate then tilted on edge. Edge-to-face molecular interactions similar to bulk p-sexiphenyl are prevalent.

Acknowledgements:

P. G. Schroeder is acknowledged for useful discussions and Jerimiah Forsythe for experimental assistance with TPD. This work was supported under Department of Energy Contract No. DE-F603-96ER14625 and The Electrochemical Society Joseph W. Richards Summer Fellowship.

References:

[1] M. A. Baldo, S. R. Forrest, Phys. Rev. B **64**, 85201 (2001).

[2] P. G. Schroeder, C. B. France, J. B. Park, B. A. Parkinson, J. Appl. Phys. **91**, 3010 (2002).

[3] P. G. Schroeder, C. B. France, J. B. Park, B. A. Parkinson, J. Phys. Chem. B **107**, 2253 (2003).

[4] C. B. France, P. G. Schroeder, B. A. Parkinson, Nano Lett. **2**, 693 (2002).

[5] C. B. France, P. G. Schroeder, J. C. Forsythe, B. A. Parkinson, Langmuir **19**, 1274 (2003).

[6] H. E. katz, Z. Bao, J. Phys. Chem. B **104**, 671 (2000).

[7] H. Yanagi, T. Ohara, T. Morikawa, Adv. Mater. **13**, 1452 (2001).

[8] H. Oji, E. Ito, M. Furuta, H. Ishii, Y. Ouchi, K. Seki, Synth. Met. **121**, 1721 (2001).

[9] N. Kock, L.-N. Yu, V. Parente, R. Laxxaroni, R. L. Johnson, G. Leising, J.-J. Pireaux, J.-L. Bredas, Synth. Met. **101**, 438 (1999).

[10] S. Buchholz, H. Fuchs, J. Rabe, J. Vac. Sci. Technol. B **9**, 857 (1991).

[11] The gold film thickness on the mica is estimated at a few microns.

[12] J. V. Barth, H. Brune, G. Ertl, R. J. Behm, Phys. Rev. B **42**, 9307 (1990).

[13] P. G. Schroeder, C. B. France, B. A. Parkinson, R. Schlaf, J. Appl. Phys. **91**, 9095 (2002).

[14] The variable temperature capabilities of this instrument were not utilized during these experiments. All STM images in this report were produced at room temperature.

[15] E. Ito, H. Oji, M. Furuta, H. Ishii, K. Oichi, Y. Ouchi, K. Seki, Synth. Met. **101**, 654 (1999).

[16] The quadrapole mass spectrometer used was a Stanford Research Systems model RGA300.

[17] The mass spectrometer was set to detect 153 atomic mass units. This mass could represent a single charged biphenyl fragment, double charged quaterphenyl ion or some other fragment.

[18] Decomposition of p-6P on the Au(111) surface during TPD is not suspected because of the similar deposition and TPD desorption temperatures.

[19] P. A. Redhead, Vacuum **12**, 203 (1962).

[20] K. Baker, A. Fratini, T. Resch, H. Knachel, W. Adams, E. Socci, Polymer **34**, 1571 (1993).

[21] C. B. France, B. A. Parkinson, unpublished.

Chapter 6: Chiral Morphology and Electronic Interface of Naphtho[2,3-a]pyrene on Au(111)

6.1 Preface:

The work presented in this chapter is the culmination of the research performed on the naphtho[2,3-a]pyrene (NP) on Au(111) system. This chapter will be published as a communication and full paper. The communication to JACS titled "Naphtho[2,3-a]pyrene forms chiral domains on Au(111)" has been submitted. This communication includes the work and discussions on the chiral domains formed by NP. The full manuscript is currently being prepared and will cover the topics of the electronic interface, adsorbate binding energy as well as structural information and analysis.

6.2 Introduction:

Stereospecific chemistry is important for the synthesis and separation of enantiopure compounds. Naturally occurring minerals, biological structures and biomolecules can contain chiral structures. The ability to produce these natural compounds is limited by the capability of reproducing the handedness of the chiral material. A surface that can sense, separate or selectively catalyze these chiral centers would be of great utility. There are at least three different approaches that can be used to generate a chiral surface, the first is the use of naturally occurring chiral surfaces, such as high index metal surfaces.[*1*] This approach has the advantage that the crystalline surface is chiral, however, it will be difficult to tailor the surface to bind a specific adsorbate. This surface will adsorb one enantiomer over another[*1*] but geometric specificity for further molecular recognition and sensor applications will be difficult to achieve.

The second and third techniques for generating a chiral surface involve the use of an achiral surface and the deposition of adsorbates that form chiral patches or pockets on the surface. These chiral patches are formed on the surface in the space between absorbed molecules. In this space, the substrate surface remains exposed and if the patches are asymmetric, then only chiral molecules of a desired enantiomer as well as the correct geometric specificity can fit within them. The pocket can then be tailored by changing the initial adsorbate, allowing for increased selectivity of the molecules being

'sensed'. While more primitive than nature's enzyme/substrate lock and key mechanism, this system should allow for the development of a similar catalytic stereospecificity. The formation of a chiral surface has been produced through the deposition of 3-D chiral molecules on low index metal surfaces.[*2, 3*] These procedures have the drawback that enantiomeric pure forms of the initial adsorbate must be available. We are currently investigating the third method of producing a chiral surface that is based on the use of achiral adsorbates, which have low symmetry and are two-dimensionally chiral. While these molecules are not chiral in three dimensions, adsorption results in the loss of mirror plane symmetry, leading to non-superimposable forms of the molecules on the surface.

Scanning tunneling microscopy (STM) has been used to characterize chiral structures on surfaces produced by organic adsorbates. Chiral adsorbates have been found to segregate into pure R or S enantiomeric domains at the liquid/solid interface.[*4*] DL-Cysteine has been observed to form racemic domains of homochiral pairs on Au in a vacuum environment. Additionally, two dimensionally chiral molecules have also been observed to produce chiral domains. Systems using covalently bound adsorbates,[*5*] metal-organic complexes,[*6*] organic acids with long alkane tails[*7*] and hydrogen bonding functional groups[*8*] have been recently reported.

We have measured the interfacial electronic structure of the naphtho[2,3-a]pyrene (NP) molecule on Au(111). (The molecular structure of NP is presented in the upper

right of figure 6.1.) Utilizing x-ray and ultraviolet photoelectron spectroscopy (XPS and UPS), an estimate of the energy level diagram has been determined. The binding of NP to Au(111) has been measured utilizing temperature programmed desorption (TPD). Unlike previous studies of symmetric aromatic adsorbates[*9, 10*], only one binding energy was observed. Scanning tunneling microscopy has been used to observed the chiral structures that are formed by NP on the highly symmetric, hexagonal, achiral Au(111) substrate. Models of the structures formed in ordered domains are proposed. While numerous morphological and electronic studies have been performed on adsorbed symmetric aromatic molecules,[*9-17*] to our knowledge this is the first observation and characterization of a two-dimensional chiral aromatic system.

6.3 Experimental:

Experiments were performed in a commercial Omicron Multi-probe ultrahigh vacuum (UHV) system (base pressure 5×10^{-11} mbar). This system is equipped with a variable temperature scanning tunneling microscopy (VT-STM) for structural characterization.[*18*]. X-ray and ultraviolet photoelectron spectroscopy (XPS and UPS) using a VSW EA125 single channel hemispherical analyzer were used to study the electronic structure of the interface. Temperature programmed desorption (TPD) has been added to the UHV system as previously described.[*10*] A physical vapor deposition

chamber (base pressure 1×10^{-9} mbar) is attached to the UHV system allowing samples and films to be prepared *in situ*.

The gold film was prepared by heating a 1 cm × 1 cm mica sample, attached to a sample plate using molybdenum clips, for 24 h in UHV at 300 °C to evaporate surface contaminants. Gold was then evaporated from a resistively heated tungsten basket onto the heated mica substrate.[*19*] The Mo clips provided an electrical contact to the gold surface during STM imaging. Sputter (3 keV Ar^+) and anneal (350 °C) cycles were used to clean and flatten the Au(111) surface. The chemical purity of the surface was determined with XPS (Mg kα, 50 eV pass energy) and the presence of the $23 \times \sqrt{3}$ reconstruction was confirmed with STM.[*20*]

Naphtho[2,3-a]pyrene (NP) (Aldrich Chemical Co.) films were deposited under UHV (base pressure 1×10^{-9} mbar) from a resistively heated boron nitride crucible (source temperature, ~ 100 °C). The source was maintained at 75 °C for 12 h prior to deposition to remove any volatile contaminants. The crucible containing naphtho[2,3-a]pyrene was heated to obtain a desired deposition rate that was monitored by a Leybold quartz crystal microbalance (QCM). The Au(111) substrate was maintained at room temperature during the deposition.

Sequential depositions were performed up to a final film thickness of 50Å. After each growth step, XPS (MgKα, 50 eV pass energy) and UPS (HeI, 21.21 eV; and HeII,

40.81 eV, both with 10 eV pass energy) in normal emission were utilized to measure the electronic structure of the surface. A -5.00 V bias was applied to the sample for the UPS measurements to separate the sample and spectrometer high binding energy cutoffs (HBECs). The spectrometer was calibrated as previously described.[*13*] Work function and highest occupied molecular orbital (HOMO) cutoff positions were determined from the high binding energy cutoffs and HOMO onsets of UP spectra and were corrected for the analyzer broadening by adding/subtracting 0.1 eV. XPS core level peak positions were determined by a fitting routine using IGOR Pro (Wavemetrics) data evaluation software. A vacuum deposited Naptho[2,3-a]pyrene film on quartz was used to obtain the solid state absorption spectrum that was measured using a Varian Cary–500 UV–vis–NIR spectrophotometer.

The STM images were obtained in a constant current mode with typical sample biases of – 0.5 V and tunneling currents between 0.1 and 0.5 nA. The Au(111) surface was renewed before each STM experiment with a sputter and anneal cycle. NP films of various thicknesses were then deposited on the cleaned surface. A background plane fit or slope correction was the only post collection processing applied to the images with the exception of Figure 6.8 and 6.11b, which were processed with an FT averaging algorithm utilizing Scanning Probe Image Processing software (Image Metrology Aps.).

6.4 Results and Discussion:

The orbital energy alignment between Au(111) and NP was performed utilizing photoemission spectroscopies. A clean Au(111) sample was prepared and characterized with both UPS and x-ray photoelectron spectroscopy (XPS). Naphtho[2,3-a]pyrene (NP) was then deposited in eight steps to a final thickness of 50Å. The He I UPS spectra of NP on Au(111) are presented in figure 6.1a, where the full spectra are on the right of the figure and the normalized and enlarged high binding energy cutoff (HBEC) is shown on the left. The bottom most spectrum is of the clean Au(111) sample and each subsequent deposition step is shown above it until a 50Å thick film is obtained. Changes in the band structure are evident as the NP film thickness increases. The existence of a large interface dipole is suggested by the significant shift in the HBEC between the bare gold sample and the 8Å NP film. The work function of the gold substrate was determined by subtracting the HBEC of the UP spectra from the source energy (21.22 eV) yielding Φ = 5.06 eV that is lower than published values for single crystal Au(111),[*21*] however this sample is a Au film on mica that contains other Au orientations. The work function of the film after deposition of 8Å of NP is determined to be 4.07 eV. The total work function shift is the difference between these numbers, 0.99 eV, representing the magnitude of the interface dipole formed by the NP on Au(111). The shift in the work function as a function of NP film thickness is plotted in figure 6.1b.

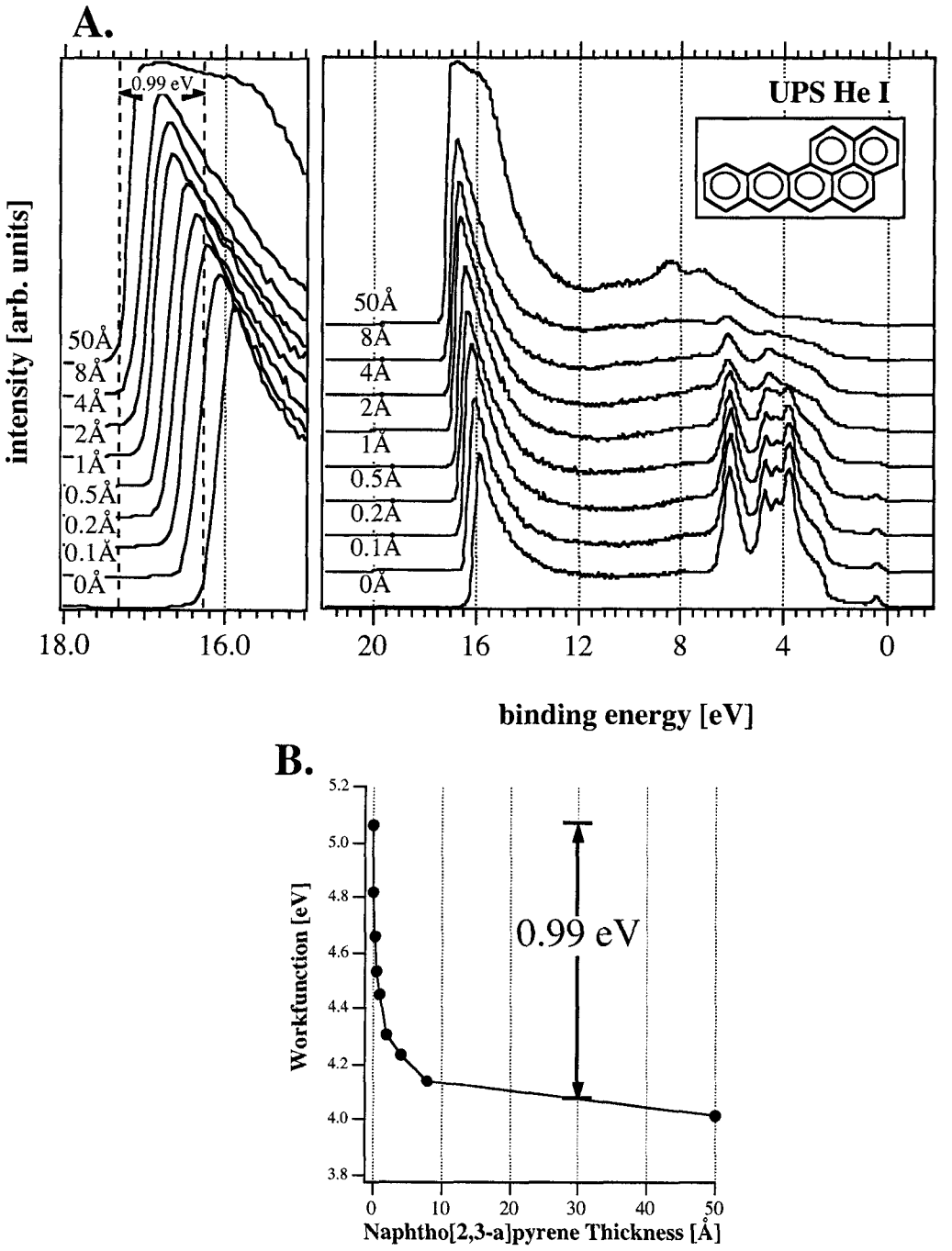

Figure 6.1: (A). UPS He I spectra of naphtho[2,3-a]pyrene deposited on Au(111). The right portion shows the full spectra on a binding energy scale. The high binding energy cutoff (HBEC) is shown on the left. The molecular structure of NP is shown in the upper right of the figure (B). A plot of the interface workfunction verses the NP film thickness. The total workfunction shift was determined to be 0.99 eV.

To monitor the chemical purity and determine if the film is charging during these experiments, atomic core level spectra were measured with XPS. [*14, 15, 22*] A complete band lineup was determined however band bending or polarization related shifts are not determined as these experiments didn't proceed to thick enough films. High-resolution C1s XP-spectra for NP on Au(111) are shown in figure 6.2a. No peak shift is observed; as the analyzer resolution is 0.2 eV and the peak positions were determined to be 284.4 ± 0.1 eV. Peak areas are shown to linearly increase with NP film coverage. A plot of the C1s peak area verse NP film thickness, as determined by quartz crystal microbalance (QCM) is shown in figure 6.2b. The 50 Å NP film is not uniform as indicated by the fact that Au XPS peaks are detected through the 50 Å NP film. The electron escape depth of the Au core level electrons should be less than 20 Å[*23*] indicating the possibility of islanding or uneven growth of the organic film.

UPS He II spectra were also obtained to monitor the valence states of the interface. Figure 6.3a shows the He II spectra that were obtained during the growth of the NP film. The bottom spectrum is the clean Au(111) film on mica. Subsequent depositions of the aromatic molecule show the valence states of the gold are gradually replaced by the spectrum of the organic film. The gold states in the spectrum are completely obscured with 50Å coverage of NP. This thick film He II UP spectrum is shown in figure 6.3.B. No gas phase photoelectron spectra for NP are available to aid in

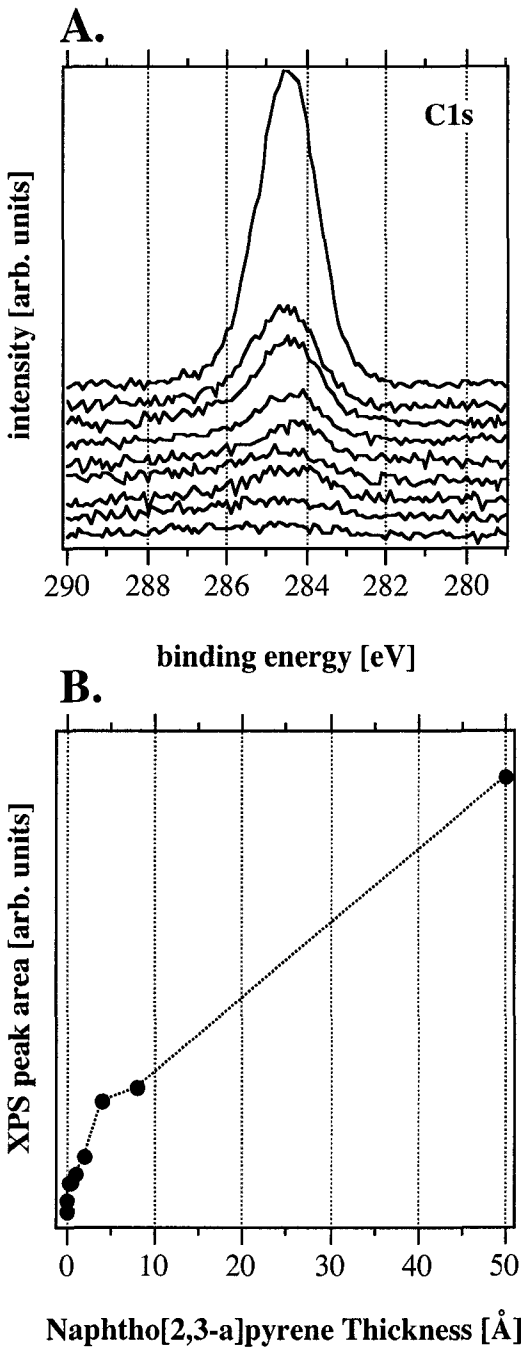

Figure 6.2: (A). C1s XPS of naphtho[2,3-a]pyrene with increasing film coverage. (B). Plot of the C1s peak area verse NP film thickness.

interpretation of this spectrum. No states are observed at the Fermi energy (0 eV) however the highest occupied molecular orbital (HOMO) of the NP film is present at the lowest binding energy edge of the spectrum and has an onset at 0.6 eV. The offset between the gold Fermi level and the HOMO cutoff of the NP is of interest because it represents the height of the hole injection barrier (E_{bh}) at the interface. (E_{bh} = 0.6 eV)

The position of the lowest unoccupied molecular orbital (LUMO) cannot be measured directly with XPS or UPS, however it can be estimated by determining the lowest energy optical absorption of a thin solid state film of NP. The visible absorption spectrum of an NP film that was deposited on a quartz slide is shown in figure 6.4. The absorption maximum occurs at 510 nm, corresponding to a band gap (E_{bg}) of 2.42 eV. (It is important to note that the optical band gap is only used as an estimate for the HOMO-LUMO gap since the large excitonic binding energy of the molecules is not accounted for and the absorption max rather than onset is used).[*24*] The estimated band gap for NP allows for the determination of the energy level position of the NP LUMO states with respect to the gold Fermi level by subtracting E_{bg} (2.42 eV) from E_{bh} (0.6 eV). This analysis also yields the magnitude of the electron injection barrier at the interface, that electrons will have to overcome to be injected into the organic material (E_{be} = 1.8 eV). The ionization potential of ionization potential of naptho[2,3-a]pyrene was determined by

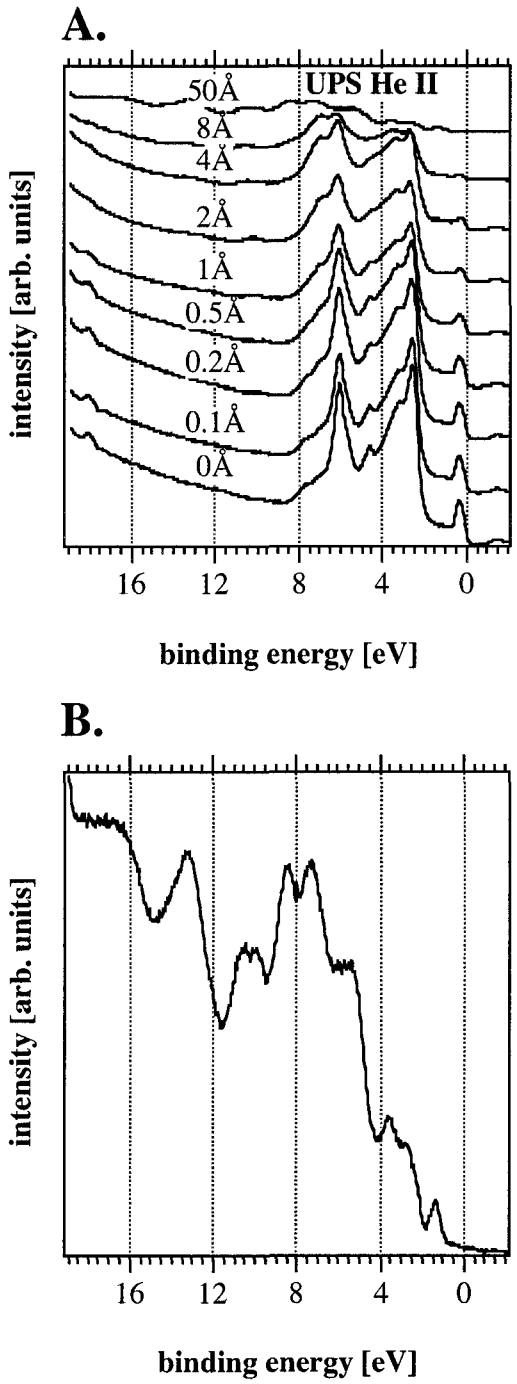

Figure 6.3: (A). UPS He II spectra of naphtho[2,3-a]pyrene on Au(111). (B). Expanded He II spectrum of 50Å thick NP film.

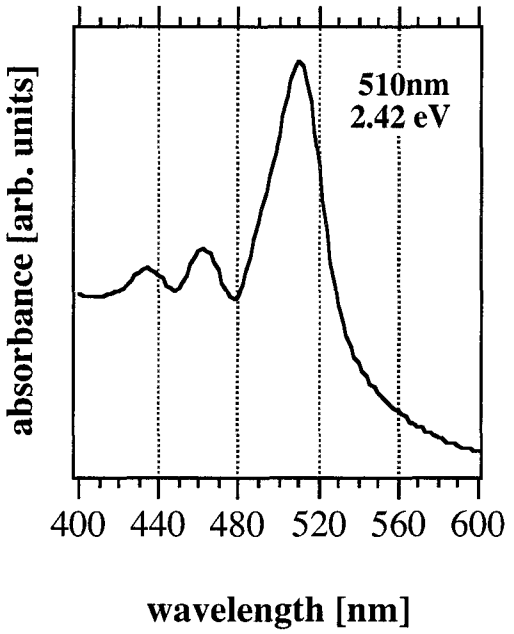

Figure 6.4: Optical absorption spectrum of a naphtho[2,3-a]pyrene film used to estimate the band gap.

adding the work function of the 50Å NP film (4.0 eV) to the HOMO cutoff (0.6 eV) of the same spectra, yielding 4.6 eV. All of these energy values are an estimate of the band line up for naphtho[2,3-a]pyrene on Au(111) since these measurements do not include the determination of polarization or band bending shifts. This information is graphically summarized in the energy alignment diagram of figure 6.5. The NP/Au(111) interface has a slightly larger interface dipole (+0.04 eV) than that found on the pentacene/Au(111) interface.[*13*] The optical HOMO-LUMO gap of NP is also larger than pentacene leading to a much larger electron injection barrier (+0.5 eV). The hole injection barrier of both interfaces is similar.

The binding energy of the naphtho[2,3-a]pyrene film was probed with temperature programmed desorption (TPD). The molecular mass of NP was too large (302 amu) to detect with our mass spectrometer therefore a lower mass/charge ratio was used for these experiments. The mass that was monitored during TPD of the NP film was at one-half its principal mass-to-charge ratio. This peak likely represents a doubly charged intact molecule since a symmetric fragment is unlikely on an asymmetric molecule. However, a concern with using a fragment peak for TPD detection is ensuring the molecule does not disassociate during deposition or while on the gold surface. We are confident the molecule remains intact during deposition as demonstrated by identical

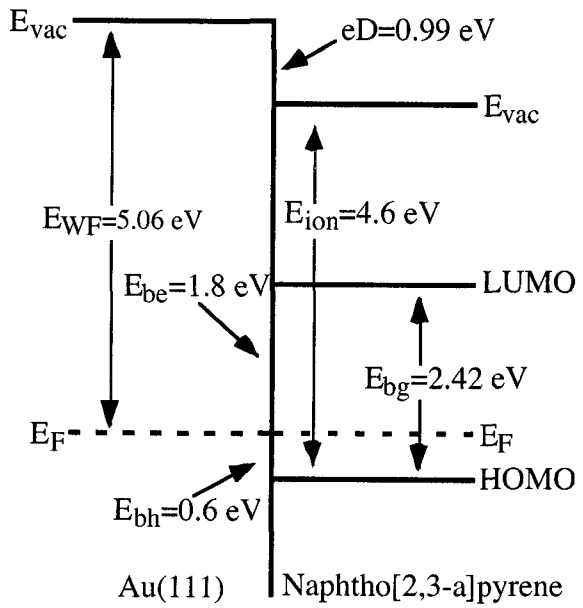

Figure 6.5: Band diagram of the naphtho[2,3-a]pyrene/Au(111) interface.

optical absorbance of evaporated films as well as non-vacuum prepared films. Additionally, the NP molecules are observed to remain intact on the Au(111) as will be demonstrated in STM experiments discussed below.

Unlike previous experiments with organic semiconductor interfaces on Au(111),[*9, 10*] we were only able to resolve one TPD peak with the NP/Au(111) system. TPD experiments were conducted at a number of different initial NP film coverages however all spectra were similar to the one presented in figure 6.6. This spectra was obtained from a 50Å thick film, however with the exception of the signal-to-noise, it is comparable to those obtained at lower initial film coverages. The base of the TPD peak appears fairly wide (>20°C range) and has a comparable width to the monolayer peak of pentacene on Au(111) which is known to be composed of a number of different structural polymorphs.[*10*] Several possibilities could explain the single binding energy environment. First, the fact that multiple peaks were not resolved simply indicates that the multilayer and monolayer binding energies could be almost identical. Second, the similar energies could be the result of the multilayer/bulk crystal structure that is formed by NP. Aromatic molecules demonstrating this multi-binding environment behavior have had similar crystal structures.[*9, 10*] Thus if NP forms a stronger crystalline packing it may have a sublimation energy identical to its binding energy to Au(111). Finally, the desorption mechanism of the asymmetric and symmetric organic adsorbates may differ.

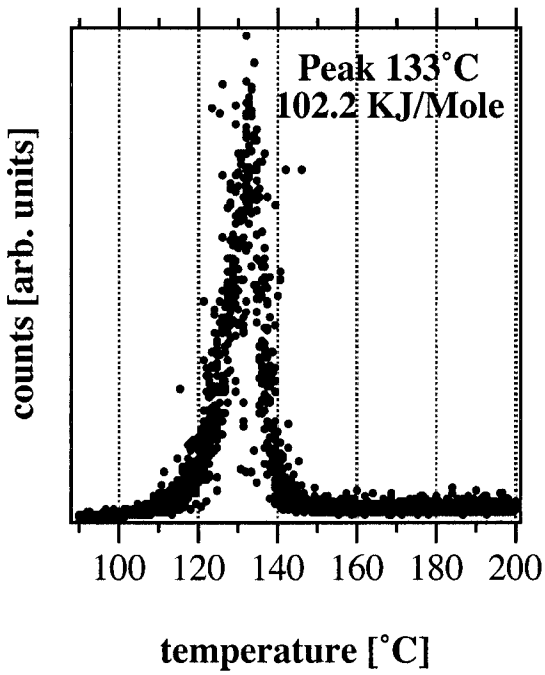

Figure 6.6: Representative temperature programmed desorption peak of naphtho[2,3-a]pyrene on Au(111). The peak temperature of NP is 133°C, which corresponds to a binding energy of 102.2 KJ/mole.

The temperature of the NP desorption peak was determined to be 133°C, corresponding to a binding energy of 102.2 KJ/mole.[*25*] This value is similar to that obtained for pentacene (106 kJ/mole bulk and 110 KJ/mole monolayer), that has a similar electronic and molecular structure[*10*]. However the higher vapor pressure of NP compared with pentacene (~100°C deposition verse 142°C for pentacene) suggested a stronger interaction with the Au(111).

Scanning tunneling microscopy was utilized to image the surface structures of NP on Au(111). The organic film was not found to lift the Au(111) $23 \times \sqrt{3}$ reconstruction since the elevated herringbone reconstruction can be seen through the organic film in the STM image in figure 6.7a. The reconstruction traverses across the small ordered NP domain in the $[1\bar{1}2]$ direction. Reconstruction elbows are present at the top of the figure where the ordered domain terminates. Disordered mobile NP molecules, moving faster than the time scale of the imaging process, cause the noisy region around the ordered domain.[*26*] A second STM image that is zoomed in on the boundary region between the ordered and the mobile areas is shown in figure 6.7b. The bright or high spots in the image represent the NP molecules. Careful inspection of these imaged molecules shows the characteristic shape of one of the enantiomers of the two-dimensionally chiral NP molecules, the shape of a backwards 'P'. All of the NP molecules in this image are the same 2-D enantiomer as indicated by the fact that each molecule is superimposable with a

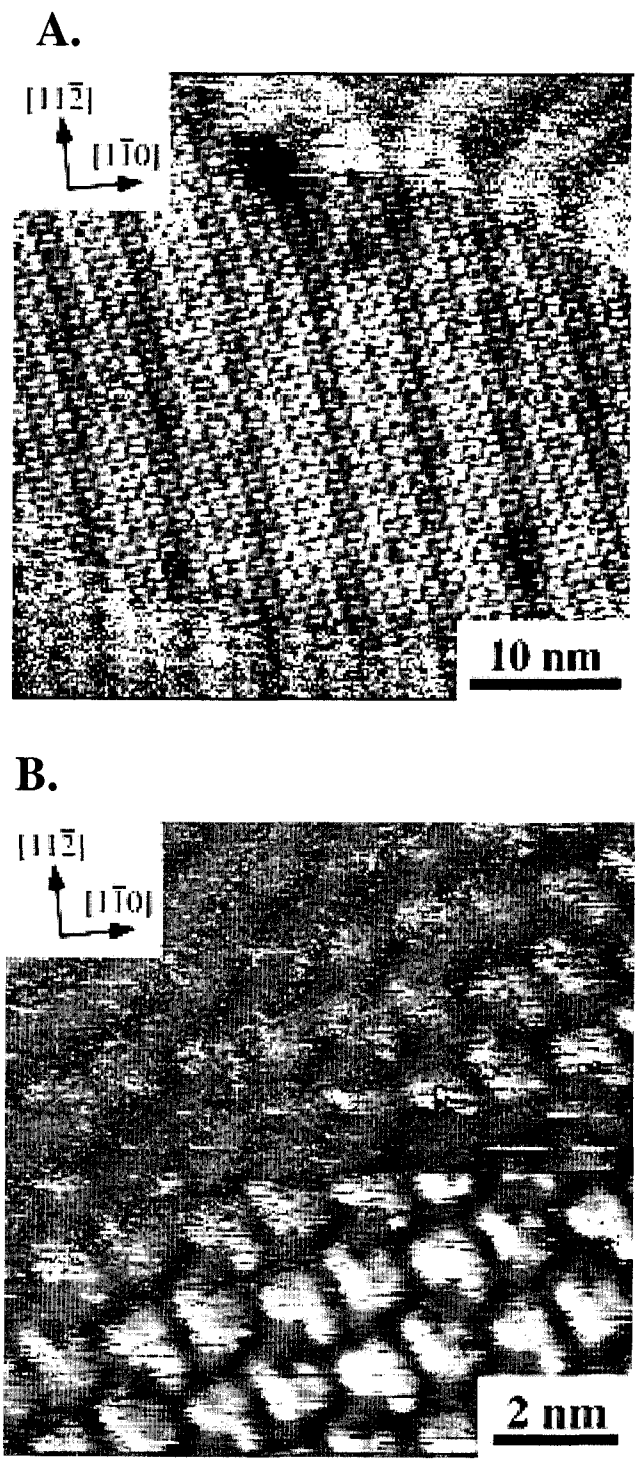

Figure 6.7: (A). STM image of NP domain on Au(111). The 23 × $\sqrt{3}$ reconstruction is visible traveling vertical in the image. (B). Zoom in of the ordered mobile boundary of the chiral NP domain.

simple 180° rotation within the plane of the surface. The fact that only one enantiomer is present in this domain indicates that the two forms of the NP molecule have segregated and formed chiral domains on the Au(111) substrate. The molecules at the top of the STM image in figure 6.7b are noisier than those at the bottom, a result of molecules moving at the edges of the ordered domain. Molecules further away (at the top of the image) spend less time ordered in the structure; therefore they are noisier or more faint than those at the bottom, which have an increased residence time in the chiral domain.

A Fourier transform filtered and averaged STM image of the chiral NP domain is presented in figure 6.8a. This STM image has been cleaned up utilizing SPIP software (as described in the experimental section) to help illustrate that chiral pockets are formed on the Au(111). The bright regions of in the image represent the NP molecules. Crossin the image from left to right, the molecular orientation within a row alternates, with one having the naphtho group pointing down and the next pointing up. Space filling models of the NP molecules are shown in figure 6.8b to help the reader more easily see the molecules orientation in this chiral domain. Perpendicular to these rows, the dark regions (where the Au(111) is exposed) have an 'S' shape to them, as apposed to a 'Z' shape which would be characteristic of the mirror image domain. 'Z' shaped domains have also been observed in STM images of NP on Au(111) indicating the formation of enantiomeric segregated domains of two dimensionally chiral molecules. As described

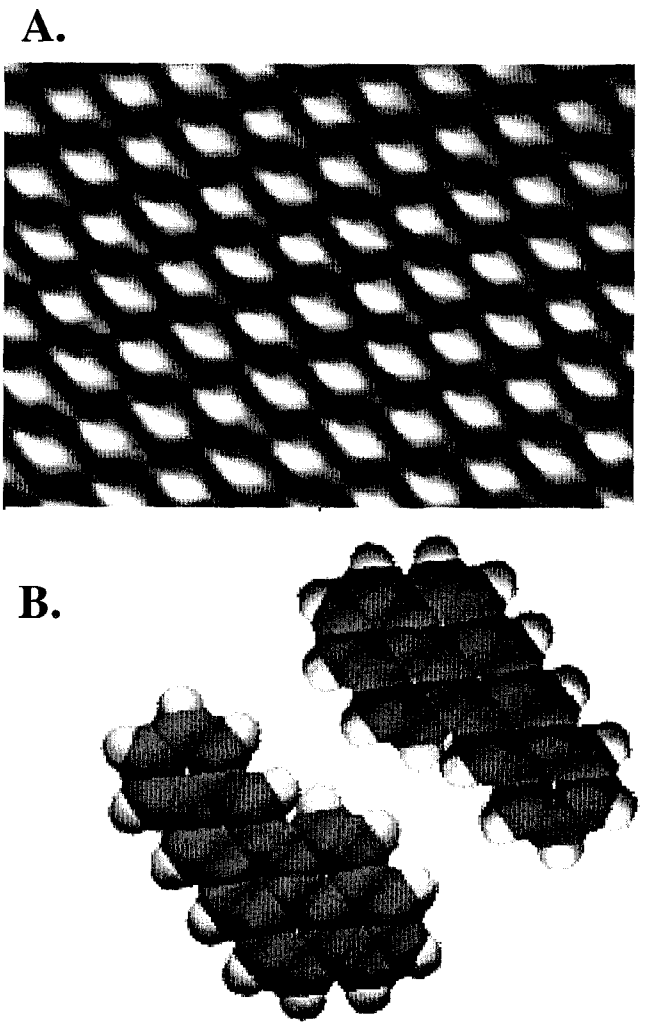

Figure 6.8: (A). Fourier filtered and averaged image of a chiral NP domain on Au(111). Notice 'S' shaped chiral regions between molecules. (B). Space filling models of NP to show orientation of molecules in figure 8a.

above, these chiral pockets of exposed metal surface could easily be influenced by changing the organic packing density, orientation, or molecules generating the film; thus customizing the shape a second molecule must have to fit into the pocket and be catalyzed or sensed.

Additional STM images of the chiral NP domain are presented in figure 6.9a and b. These two high-resolution images reveal the shapes of the individual molecules. The unit cell is drawn as the black square in figure 6.9b. The measured short unit cell distance, along the direction where the NP molecules have an end-to-end nearest neighbor interaction averaged 16.3Å with a standard deviation of ±0.4Å (a = 16.3 ± 0.4 Å). The long unit cell distance averaged 19.4 Å with a standard deviation of ± 1.0 Å (b = 19.4 ± 1.0Å). The unit cell angle between a and b is 50 ± 3°. The angle between the reconstruction direction $[1\bar{1}2]$ and the a unit cell direction was measured to be 86 ± 2°.

A proposed model structure of the chiral domains is presented in figure 6.10. The modeled unit cell contains two molecules and is representative of the chiral plane group p2. The domain is modeled with the terminal rings of the molecules located on atop sites of the gold surface; although we have not directly observed this level of detail, the orientation of the molecules with respect to the reconstruction is consistent. Our previous studies with similar large aromatic molecules, as well as other investigations, suggest that molecules prefer to place the largest possible number of aromatic rings centered directly

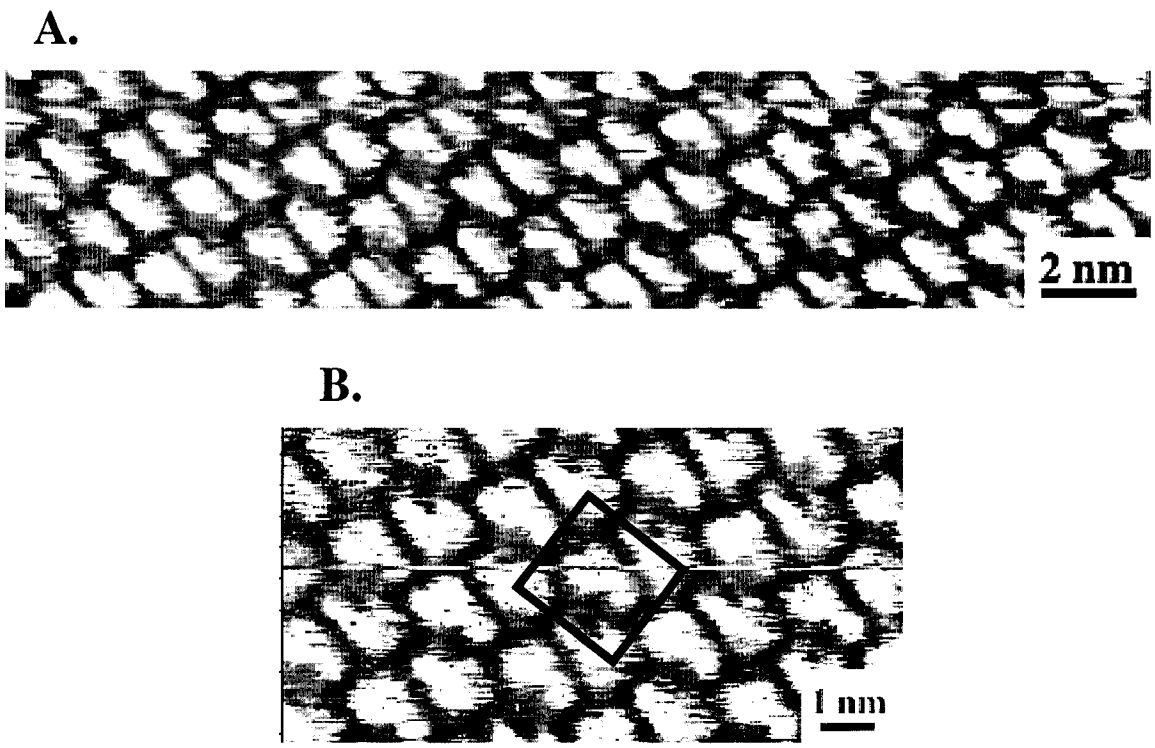

Figure 6.9: (A). STM image of domain containing a single NP enantiomer. (B). Unit cell of chiral domain is outlined by black box.

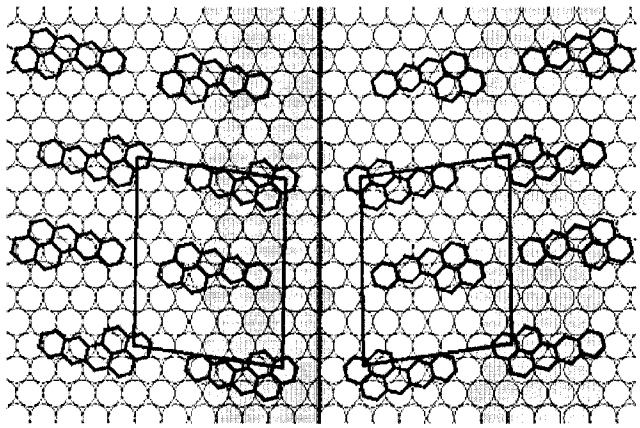

Figure 6.10: Proposed model of enantiomeric domains formed by 2-D chiral naphtho[2,3-a]pyrene.

above Au atoms.[*9-12, 27*] The model unit cell parameters are compared with the experimental measurements in Table 6.1. Furthermore, the model predicts that chiral domains should intersect at an angle of 162° (between adjacent unit cell vectors) that was also observed in STM images. All modeled parameters are shown to be in good agreement with the experimentally measured distances and angles.

A second lower coverage chiral structure has also been observed with STM albeit with lower resolution. It is important to note that this structure is not commonly imaged and high-resolution images like those shown above have not been obtained. However, enough information has been gathered about this structure that a model has been developed that is supported by the thorough analysis and high-resolution images of the previously discussed structure. An STM image of the low coverage structure is presented in figure 6.11a were the upper right of the image is the ordered domain and the lower left is a noisy region of mobile molecules. The NP molecules appear as bright spots in the image with the molecules aligning themselves with the long axis of the molecule just left of vertical. The NP molecules appear to order into a type of superstructure where clusters of two to four end-to-end rows lay next to each other. The fundamental building block of this structure is shown in figure 6.11b. This is a zoom in image of the structure in figure 6.11a, obtained utilizing the correlation-averaging algorithm in the SPIP software package. The pairing of the molecules into rows with the long axis of the molecule

Table 6.1: Experimentally Measured and Modeled Parameters for the Chiral Domains Formed by Naphtho[2,3-a]pyrene Molecules on Au(111).

Parameter	Experimental	Modeled
a	16.3 ± 0.4Å	16.1 Å
b	19.4 ± 1.0 Å	19.9 Å
α	50 ± 3°	50.2°
∠a, Reconstruction	86 ± 2°	81°
∠ Enantiomeric Domains	163 ± 5°	162°

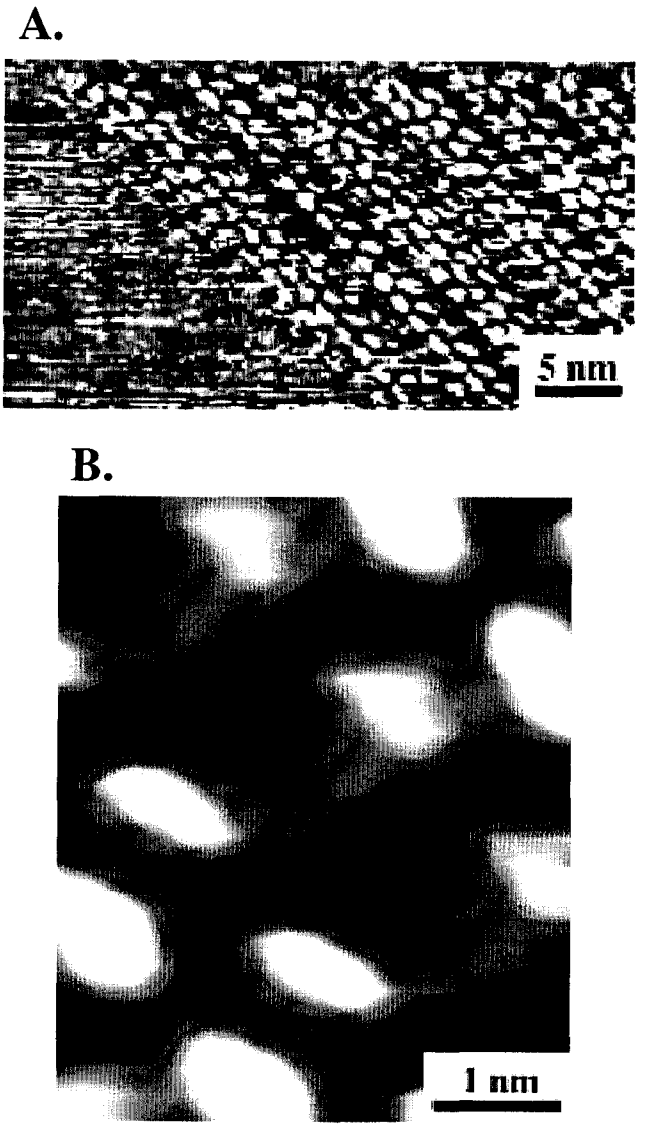

Figure 6.11: (A). STM image of low-coverage NP domain on Au(111). (B). Zoom-in STM image of low-coverage structure obtained utilizing the correlation-averaging algorithm in the SPIP software.

pointing in the row direction is clearly evident. Some of the molecules imaged in both figure 6.11a and b have larger ends, suggesting the direction of the molecule containing the pyrene group. Analysis of a number of images of this structure shows that the paired rows adjacent to each other are slightly offset, thus making the long axis of the unit cell encompass two paired rows. It is also worth stating that the offset is not always observed and the energy difference between separated rows being offset or not is likely to be quite small. The measured distances of this long axis unit cell (over two rows) was b = 40.3 ± 2.7Å. The short axis unit cell distance, which corresponds to the length of the NP molecule, is a = 17.0 ± 0.8 Å. This measurement is the same as the a-axis of the previous structure and is within the standard deviation of the two measurements. The unit cell angle was determined to be 96.2 ± 5.2° and the angle between the a-axis and the Au(111) reconstruction ($[1\bar{1}2]$) was 98 ± 5°. Different domains, thought to be composed of different enantiomers, had an a-axis angle difference of 163 ± 5°, again nearly identical to the enantiomeric domain boundary angle shown in the first chiral structure.

A proposed model for the low coverage paired row chiral structure is presented in figure 6.12. The dark substrate atoms represent the elevated Au(111) atoms of the reconstruction. The modeled unit cell parameters are presented in table 6.2 and compared with the experimentally measured values where there is good agreement. The molecules interact with the gold lattice in the same manner as the higher coverage

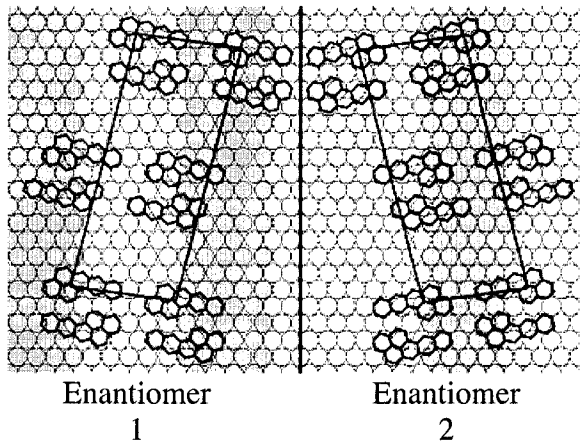

Figure 6.12: Proposed model for second low coverage chiral domain.

Table 6.2: Experimentally Measured verse Modeled Parameters for the Low Coverage Chiral Domain Formed by the Two-Dimensionally Chiral Naphtho[2,3-a]pyrene Aromatic Molecules on Au(111).

Measurement	Experimental	Modeled
a	17.0 ± 0.8Å	16.1 Å
b	40.3 ± 2.7 Å	38.8 Å
∠a,b	96.2 ± 5.2°	96.1°
∠a, reconstruction	98 ± 5°	99°
∠Enantiomeric Domains	163 ± 5°	161°

structure (described above). The homochiral pairing of the molecules in this structure is shown in the model. It is unclear why the molecules form these paired rows, however it is worth noting that this type of interaction has been observed in symmetric aromatic molecules of p-sexiphenyl and low coverages of pentacene on Au(111). [*10, 28*] The modeled parameters for this paired row structure are all in agreement with the experimentally measured distances and angles.

6.5 Summary:

We have characterized the electronic structure of the interface of the low symmetry 2-D chiral aromatic molecule naphtho[2,3-a]pyrene on Au(111) using UPS and XPS. Optical absorbance of a solid state film of NP was used to estimate the HOMO-LUMO band gap of the organic material. The band lineup of NP on Au(11) was presented, showing that a Schottky barrier is formed between these materials, with electron and hole injection barriers of 1.8 eV and 0.6 eV, respectively. A large interface dipole of 0.99 eV was measured at the immediate interface. TPD has been used to determine the binding energy of the NP on the metal surface. One peak was observed with a peak temperature of 133°C corresponding to a binding energy of 102.2 KJ/mole. Two different chiral domains have been observed utilizing scanning tunneling microscopy. High-resolution images have shown that the domains are comprised of only

one 2D enanitomeric form of NP. At higher packing densities, the NP molecules formed ordered domains with nearest neighbor molecules alternating by 180°. A model has been proposed showing the ordered chiral domains as well as the interaction of the NP molecules with the hexagonal Au(111) lattice. A second, lower coverage chiral structure as also been observed. The interaction with the substrate is identical to the high-density film, however the molecules form homochiral-paired rows across the surface. A model has been proposed which is in agreement with experimental measurements.

These chiral domains have spontaneously formed on a hexagonal low index metal surface. The ordered structures have formed without strong interactions between molecules such as hydrogen bonding or chemical bonds with the gold substrate. The dynamics of the chiral domain formation via surface diffusion or molecular "flipping" is currently under study. It is also worth noting that the spaces between the molecules form chiral "pockets / patches" that may be selective for the adsorption of specific 3D chiral molecules. Such chiral recognition may be important for the future development of sensors for optically active molecules or chirally selective catalysis.

References:

[1] J. D. Horvath, A. J. Gellman, J. Am. Chem. Soc. **123**, 7953 (2001).

[2] Q. Chem, C. W. Lee, D. J. Frankel, N. V. Richardson, PhysChemComm **9**, 05986 (1999).

[3] T. Nakanishi, N. Yamakawa, T. Asahi, T. Osaka, B. Ohtani, K. Unosaki, J. Am. Chem. Soc. **124**, 740 (2002).

[4] H. Fang, L. C. Giancarlo, G. W. Flynn, J. Phys. Chem. B **102**, 7311 (1998).

[5] B. Ohtani, T. Shintani, K. Uosaki, J. Am. Chem. Soc. **121**, 6515 (1999).

[6] P. Messina, A. Dmitriev, N. Lin, H. Spillmann, M. Abel, J. V. Barth, K. Kern, J. Am. Chem. Soc. **124**, 14000 (2002).

[7] D. G. Yablon, L. C. Giancarlo, G. W. Flynn, J. Phys. Chem. B **104**, 7627 (2000).

[8] J. V. Barth, J. Weckesser, G. Trimarchi, M. Vladimirova, A. De Vita, C. Cai, H. Brune, P. Gunter, K. Kern, J. Am. Chem. Soc. **124**, 7991 (2002).

[9] C. B. France, B. A. Parkinson, App. Phys. Lett. **82**, 1194-1196 (2003).

[10] C. B. France, P. G. Schroeder, J. C. Forsythe, B. A. Parkinson, Langmuir **19**, 1274 (2003).

[11] C. B. France, P. G. Schroeder, B. A. Parkinson, Nano Lett. **2**, 693 (2002).

[12] P. G. Schroeder, C. B. France, J. B. Park, B. A. Parkinson, J. Appl. Phys. **91**, 3010 (2002).

[13] P. G. Schroeder, C. B. France, J. B. Park, B. A. Parkinson, J. Phys. Chem. B **107**, 2253 (2003).

[14] P. G. Schroeder, C. B. France, B. A. Parkinson, R. Schlaf, J. Appl. Phys. **91**, 9095 (2002).

[15] P. G. Schroeder, M. W. Nelson, B. A. Parkinson, R. Schlaf, Surf. Sci. **459**, 349 (2000).

[16] M. Lackinger, S. Griessl, W. Heckl, M. Hietschold, J. Phys. Chem. B **106**, 4482 (2002).

[17] R. Schlaf, B. A. Parkinson, P. A. Lee, W. Nebesny, N. R. Armstrong, J. Phys. Chem. B. **103**, 2984 (1998).

[18] The variable temperature capabilities of this instrument were not utilized during these experiments. All STM images in this report were produced at room temperature.

[19] The gold film thickness on the mica is estimated at a few microns.

[20] J. V. Barth, H. Brune, G. Ertl, R. J. Behm, Phys. Rev. B **42**, 9307 (1990).

[21] D. R. Lide, Ed., *Hand Book of Chemistry and Physics* (CRC Press, Boca Raton, ed. 74th, 1994).

[22] R. Schlaf, P. G. Schroeder, M. W. Nelson, B. A. Parkinson, P. A. Lee, N. R. Armstrong, J. Appl. Phys. **86**, 1499 (1999).

[23] C. D. Wagner, W. M. Riggs, L. E. Davis, J. F. Moulder, G. E. Muilenberg, *Handbook of x-ray photoelectron spectroscopy* (Perkin-Elmer Corporation, Eden Prairie, MN, 1979).

[24] M. Pope, C. E. Swenberg, *Electronic Processes in Organic Crystals and Polymers* (Oxford University Press, Oxford, 1999).

[25] P. A. Redhead, Vacuum **12**, 203 (1962).

[26] S. Berner, M. Brunner, L. Ramoino, H. Suzuki, H.-J. Güntherodt, T. A. Jung, Chem. Phys. Lett. **348**, 175 (2001).

[27] M. Kasaya, H. Tabata, T. Kawai, Surf. Sci. **400**, 367 (1998).

[28] F. A. Frame, C. B. France, B. A. Parkinson, unpublished (2003).

Concluding Remarks and Future Work:

Pentacene, *p*-sexiphenyl and naphtho[2,3-a]pyrene have been characterized on Au(111). The interfaces of these organics with gold have produced large interface dipoles of nearly one electron volt. This significant dipole has been estimated to be the equivalent of nearly one electron removed from each molecule to the metal substrate in the lower coverages of the organic film. These interface states have been used by Bald and Forrest (see chapter 1) to model electronic characteristics of a similar interface, demonstrating the importance of these junctions. We have studied these interfaces to try and understand the consequences of such a large interface dipole and its effect on the morphology of the organic materials.

A number of unusual and unexpected structures have been observed with these organics on Au(111). The pentacene / metal interface in particular has demonstrated the complexity of the interface. The rich structure that has been formed by this simple symmetric aromatic molecule has been directly observed utilizing a scanning tunneling microscope. The formation of many coverage-dependent structures including a shift in nearest neighbor interactions with coverage from end-to-end to side-by-side is quite peculiar. We have been able to study this interface from a number of important vantage points including electronic, binding energy and structural characterization. Interesting

multilayer structures have also been observed with STM. We have proposed a model that is compliant with experimental measurements however a clear understanding of the reason for the strange structure has not been determined. The computational modeling of this interface, to include the interface dipole and its change with increasing organic film coverage, to obtain information about the electronic states of the organic semiconducting molecule may shed light on the organic molecule-molecule and molecule-metal interactions. While calculations of this magnitude, with the Au substrate and organic adsorbate are presently extremely challenging, they should be pursued in the future.

p-Sexiphenyl on Au(111) has shown the smallest interface dipole we have investigated. Unique alternating molecule structures have been observed with this system. These structures are similar to the bulk structure of p-6P. We know of no other studies that have observed an organic structure similar to this unusual domain. An effort to further understand this system and other structures that are formed are currently underway. In those experiments, interesting and unusual structures have been observed that were not expected from this large 'log' like molecule.

These two symmetric aromatic molecules have produced unexpectedly rich structure on Au(111). Since these results were surprising, an obvious gap in the scientific understanding of these interfaces has been exposed. Further studies should be undertaken beginning with simple aromatic molecules to determine if large interface dipoles are

always formed, can they be tailored and what structural significance do they play. While studies of this magnitude will take time, the knowledge obtained could influence not only the fundamental understanding of interface science but also the commercial application of organic based electronic devices.

Two-dimensionally chiral aromatic molecules adsorbed on Au(111) have been investigated. The electronic structure of this interface has been studied and the largest interface dipole we have measure has been found. The spontaneous segregation of the 2-D enantiomers causes the formation of chiral domains on the Au(111) substrate. High-resolution STM images of these molecules have allowed the unambiguous determination of the chiral nature of the surface. This system has been difficult to study from an experimental standpoint. Intramolecular resolution STM images have been difficult to obtain with this system. The trick for the formation of ordered domains is the use of a slow deposition rate (<0.5 Å/min). Faster deposition rates appear to produce randomly oriented molecules and domains. Annealing the organic films simply causes more random orientation on the surface. Another possible method of increasing the size of ordered domains is for the Au(111) substrate to be cooled during the deposition. This will require extensive growth chamber modification, as we are not currently setup to cool the sample during deposition.

Future investigations of interfaces with low symmetry aromatic molecules should be undertaken. Multiple interfaces should be studied to see if spontaneous segregation takes place in all of the systems. Computational modeling of the interface dipole and the electronic states of the molecules should be performed to determine if the formation of chiral domains is somehow influenced by the charge donation from the molecules to the substrate. A very exciting proof of concept experiment would be to observe the selective binding of a second three dimensionally chiral molecule within the chiral pockets of the enantiomers of the 2-D chiral organic film. While this experiment could be difficult to achieve, I believe it is experimentally possible.

Appendix A: Joseph W. Richards Fellowship from the Electrochemical Society

A research statement submitted to the Electrochemical Society. This report and application was competitively awarded the Joseph W. Richards Fellowship, 2002.

Converting sun light to electrical energy at reasonable cost has long been sought after. Solid state solar cells are capable of generating electrical power through the absorption of photons at an interface of differently doped materials. However, to efficiently collect these electrons, very pure semiconductor materials are required to prevent recombination. The requirement for high purity semiconducting substrates drastically increases the cost, preventing large area arrays of these cells from being practical. When O'Regan and Grätzel[*1*] discovered that nanocrystalline TiO_2 semiconductor particles with dye molecules could convert light to electrical energy with greater than 10% efficiency, much research ensued [*2, 3*]. The low cost of the colloidal semiconductor substrates and organic sensitizing dyes provide the possibility of

generating large area light harvesting devices at more affordable costs. Many important areas of research concerning these cells are underway to investigate the fundamental operating mechanisms of these new electrochemical solar cells [*4*].

Dye sensitized solar cells are essentially an electrochemical cell with light performing the "pumping" action to push electrons through an electrical circuit [*1*](see figure A.1). Electrons are excited to the lowest unoccupied molecular orbital of the dye molecule through the absorption of visible light. These excited state electrons have the energy to inject into the conduction band of the metal oxide semiconductor. The electron is then swept to a back contact and through an electrical circuit where it can perform work at a load. The electron is then returned to the electrochemical cell were it reduces a redox couple in solution. This reduced species can then regenerate the oxidized dye allowing the entire process to repeat. Dyes used in these cells are selected based on their stability and ability to efficiently absorb light over the solar spectrum. Titanium Dioxide can be used as the semiconductor because of its large band gap, which provides stability under illumination [*5*] and is involved in the generation of the cells photovoltage [*6*]. When the energetics of the semiconductor, dye and electrolyte are correct, these electrochemical cells come close to rivaling the efficiency of silicon based solid state devices.

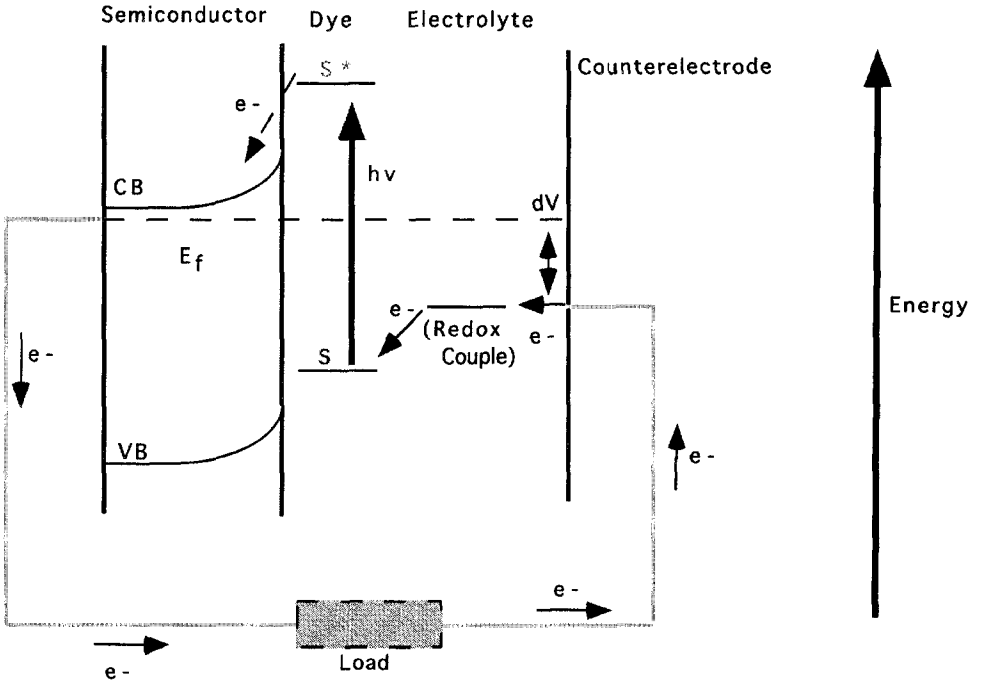

Figure A.1: A schematic of a dye sensitized photoelectrochemical solar cell.

Work has been performed to optimize the different interfaces and maximize the power that these cells can generate. Such research has included preventing back reactions of the injected electron into the oxidized dye or electrolyte [*7-9*], optimizing the preparation of the semiconductor substrate[*10*], and modifying the dye molecules [*11-13*]. Different electrolyte solutions and redox couples have also been investigated including the possibility of solid state electrolyte materials[*14*]. The use of simple organic dyes for the sensitization process have the potential to lead to higher efficiency based on their overall stability, improved photophysics, larger absorption cross section and smaller molecular size.

My thesis research involves the investigation of the semiconductor dye interface, which is responsible for charge separation in these devices. I am interested in developing an organic based dye that could be used to investigate fundamental properties and mechanisms of these devices, as well as function as a robust and efficient sensitizer. The model dye system chosen for these experiments is 3,4,9,10-peryelenetetracarboxylic acid dianhydride (PTCDA), see figure A.2 for a diagram of this molecule. Perylene based dyes have been used commercially as red pigments for over 50 years and are known for their photo and chemical stability [*15*]. They absorb in the visible with large molar extinction coefficients ($\in \sim 10^4 - 10^5\ M^{-1}\ cm^{-1}$). PTCDA was selected because of its

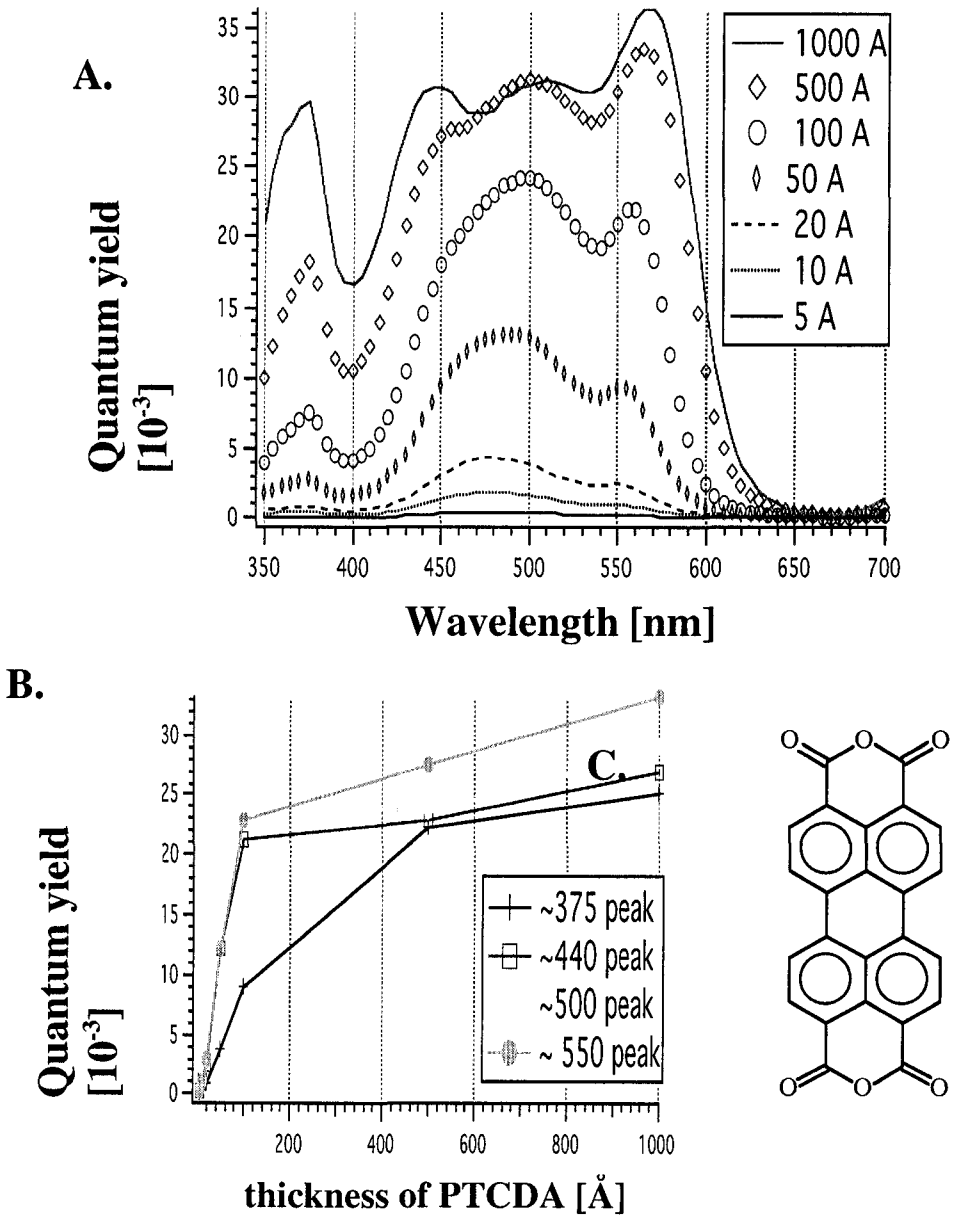

Figure A.2: a) Photoaction spectra of PTCDA with increasing film thickness. b) Graph showing the increase in photoaction peaks with increasing thickness.

known physical properties[*16-18*], ease of chemical modification [*19, 20*] and availability.

Dye sensitzed solar cell devices use nanocrystalline semiconductor particles because of their high surface area. Nanocrystalline particles have non-uniform surfaces, crystalline orientation, structure, and sizes that prevent detailed investigations of the interface properties. Therefore, metal oxide single crystal or polycrystalline films will be used as substrates. These films will provide better control of the semiconductor surface structure and orientation, allowing further insight to these interfaces. The single crystal surfaces also permit multiple surface analysis techniques to be used. However, since the nanocrystalline substrates have such large surface areas, where large amounts of dye can be absorbed, some of the photoelectrochemical experiments may require their use to obtain usable analytical signals.

When organic dyes are deposited onto a substrate surface for use in dye sensitized cells, there is a balance that must be achieved to optimize both light absorption and charge injection into the semiconductor. If the film is too thin, only a fraction of the light is collected. A thicker film absorbs more light but more electron hole pairs are generated further from the dye semiconductor interface. These electrons must traverse the thickness of the film to be collected. Many are lost due to recombination in the dye before they are collected by the semiconductor. Evidence for this is shown in figure A.2,

a repetition of work performed by the Armstrong group at the University of Arizona [*21*]. The photoaction spectra in fig A.2a shows spectra for PTCDA films of varying thickness on fluorine doped SnO_2 films. It is demonstrated in figure A.2b that at a thickness of approximately 100Å of PTCDA, the quantum yield (collected electrons per incident photon) reaches a steady state. Even with a ten fold increase in the thickness of dye on the surface, the number of collected electrons does not significantly increase.

My research is centered on trying to get around this thickness limited increase in the quantum yield. To do this, I am working towards the development of a sensitizer that would allow the excited state electrons generated far from the interface to be harvested at the semiconductor with minimal recombination loss. A chemically bound molecular layer chromophore system that allows for precise control of the number of layers and thus the thickness is being developed. The covalent linkage of the chromophores to the surface and within the sensitizer will be robust and should allow orbital delocaliztion over the film thickness and thus increase conduction of electrons to the semiconductor interface. Figure A.3 shows a model of how this system will work. The initial step is the covalent attachment of a trimethoxypropylamine to the semiconductor surface, figure A.3a. This amine is then covalently linked to the PTCDA dye with an imide linkage, figure A.3b. A diamine 'linker' compound is then attached to regenerate the amine

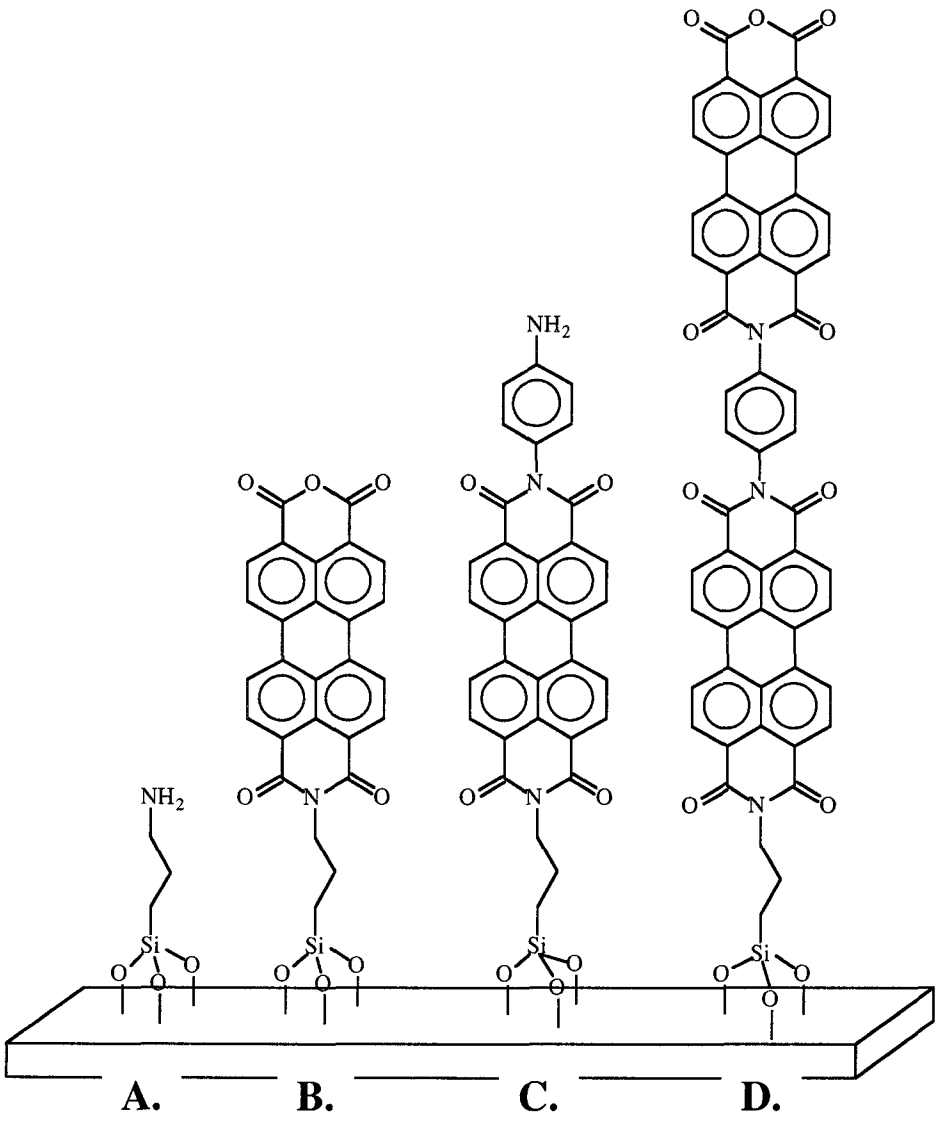

Figure A.3: Growth of chemically bound molecular layer chromophores. a) step 1, substrate silanization b) step 2, imidization of PTCDA chromophore c) step 3, attachment of diamine linker d) step 4, imidizaion of second PTCDA chromophore.
These steps can be repeated to further lengthen the chromophore chain.

terminated surface, figure A.3c. Another anhydride chromophore can then be attached to the surface. By cycling through these growth procedures, a layer-by-layer growth of the desired chromophores can be achieved.

Preliminary results have demonstrated the applicability of this molecular layer system. Figure A.4 shows photoaction spectra of samples with varying numbers of bound perylene chromophores. The step by step increase in the number of dye layers has shown an increase in the quantum yield obtained by these devices. A linear increase in the photocurrent with increasing numbers of molecular chromophore layers can be seen in figure A.5. The limit to improvement with this system has not been reached but the feasibility of this approach has been demonstrated. While these preliminary results are significantly less efficient than those described by Gratzel [*1*], it is important to point out that they were performed on flat metal oxide surfaces and not nanocrystalline films. Recently, an approach to obtain multiple layers of dyes in a solar cell application was attempted by linking dye molecules together by chelating them to a metal atom [22]. This publication demonstrates the importance and applicability of this research. We believe our all organic chemically bound molecular layer chromophore system should be more robust, chemically facile and easily diversified.

During the time of the fellowship support, I anticipate working to optimize the system by varying the metal oxide substrates and diamine linkage molecules. Different

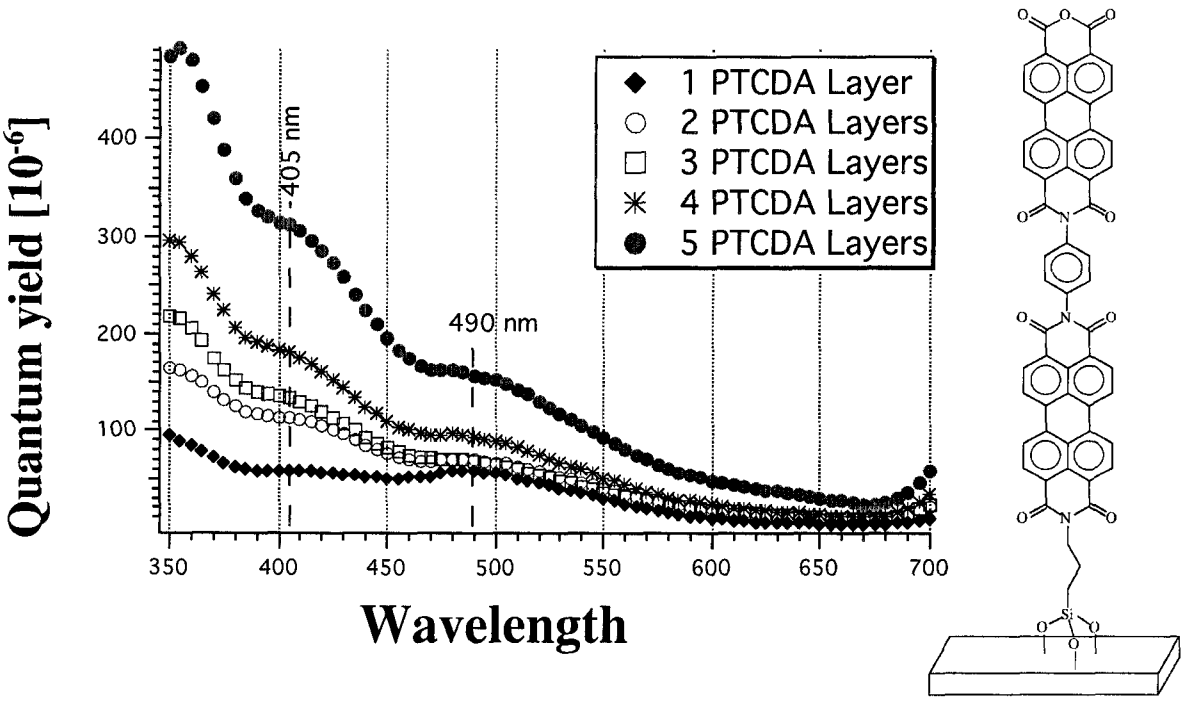

Figure A.4: Photoaction spectra of system with varying layers of perylene

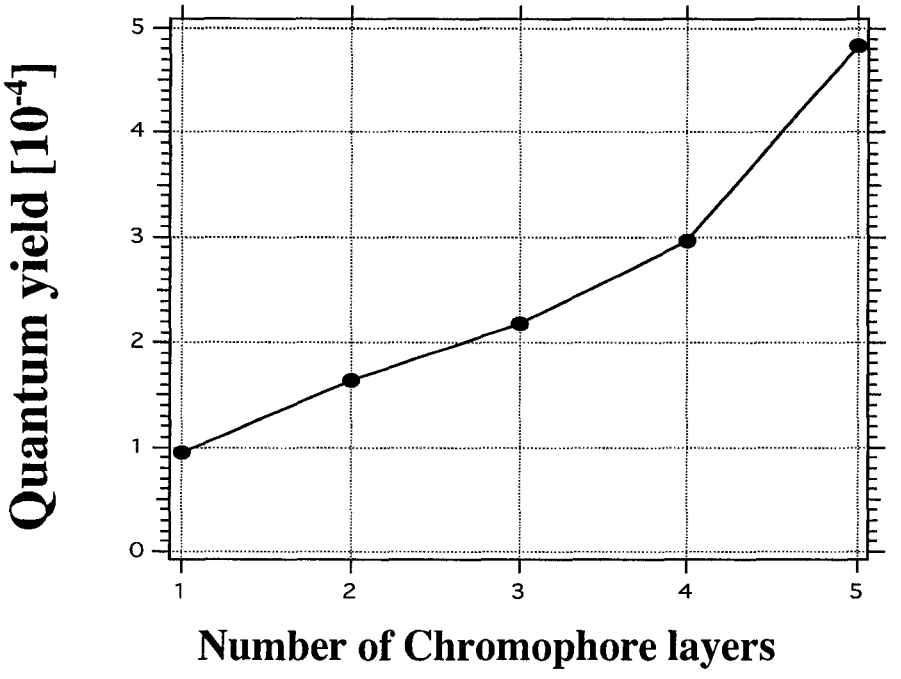

Figure A.5: Graph demonstrating quantum yield increases obtained with increasing chromophore (PTCDA) layer thickness. Data obtained from 405nm peaks in fig A.4.

diamine layers will be attempted in an effort to optimized the energetics of the system. An aromatic amine silane linkage to the surface will be attempted; this should increase the conductivity at the interface between the substrate and chromophore chains. Increasing the conductivity should minimize the number of electrons lost before collection at the semiconductor. Imide linkages are not the only type of linkage that can be attempted with this system. Perylene chromophores with two carboxylic acid groups on opposite ends of the molecule will be used to form an amide linkage with diamine linkers. These variations will be performed to further our understanding of this electrochemical system.

As stated in Electochemical Society publications, the society is interested in the advancement of the fields of electrochemical science and technology and solid state science and technology. This research problem has direct applications in both fields. Work on the photoelectrochemical dye sensitized cell will provide fundamental information in electron transfer events at surfaces. This knowledge could lead to advancements in fields such as photochromics and photocatalysis applications and possible application in new light harvesting technologies. This research is worthy of the support of the Electrochemical Society and I look forward to submitting a report on the advancements of this project if awarded this summer fellowship.

References:

[1] B. O'Regan, M. Gratzel, Nature **353**, 737 (1991).

[2] T. Gerfin, M. Gratzel, L. Walder, in *Molecular level artificial photosynthetic matericals* G. J. Meyer, Ed. (John Wiley & Sons, Inc., New York, 1997), vol. 44, pp. 345 - 393.

[3] A. Hagfeld, M. Gratzel, Acc. Chem. Res. **33**, 269 (2000).

[4] A. Hagfeldt, M. Gratzel, Chem. Rev. **95**, 49 - 68 (1995).

[5] H. Gerishcher, in *Solar Energy Conversion Solid State Physics Aspects* B. O. Saraphin, Ed. (Springer-Verlag, New York, 1979), vol. 31, pp. 115 - 172.

[6] D. Cahen, G. Hodes, G. Michael, J. F. Gillemoles, I. Riess, J. Phys. Chem. B **104**, 2053 (2000).

[7] J. S. Salafsky, W. H. Lubberhuizen, E. van Faassen, R. E. I. Schropp, J. Phys. Chem. B **102**, 766 (1998).

[8] B. Gregg, F. Pichot, S. Ferrere, C. Fields, J. Phys. Chem. B **105**, 1422 (2001).

[9] H. Ghosh, J. Phys. Chem. B **103**, 1999 (1999).

[10] N. Park, J. van de Lagemaat, A. J. Frank, J. Phys. Chem. B **104**, 8989 - 8994 (2000).

[11] M. K. Nazeeruddin, A. Kay, I. Rodicio, R. Humphry-Baker, E. Muller, P. Liska, N. Vlachopoulos, M. Gratzel, J. Am. Chem. Soc. **115**, 6382 - 6390 (1993).

[12] A. Ehret, L. Stuhl, M. T. Spitler, J. Phys. Chem. B **105**, 9960 (2001).

[13] Z.-S. Wang, F.-Y. Li, C.-H. Huang, Chem. Commun., 2063 (2000).

[14] U. Bach, D. Lupo, P. Comte, J. E. Moser, F. Weissortel, J. Salbech, H. Spreitzer, M. Gratzel, Nature **395**, 583 (1998).

[15] W. A. Fisher, *Pigment Handbook Volume I: Properties and Economics.* T. C. Patton, Ed., Pigment Hankbook (John Wiley & Sons, New York, 1973), vol. 1.

[16] V. Bulovic, P. E. Burrows, S. R. Forrest, J. A. Cronin, M. E. Thompson, Chem. Phys. **210**, 1 (1996).

[17] J. R. Osterick, A. Dodabalapur, L. Torsi, A. J. Lovinger, E. W. Kwock, T. M. Miller, M. Galvin, M. Berggren, H. E. Katz, J. Appl. Phys. **81**, 6804 (1997).

[18] R. Kaiser, M. Friedrich, T. Schmitz-Hubsch, R. Sellam, T. U. Kampen, K. Leo, D. R. T. Zahn, Fresenius J. Anal. Chem. **363**, 189 (1999).

[19] S. Ferrere, A. Zaban, B. Gregg, J. Phys. Chem. B **101**, 4490 - 4493 (1997).

[20] H. Tian, P.-H. Liu, W. Zu, E. Gao, D.-J. Wu, S. Cai, J. Meter. Chem. **10**, 2708 (2000).

[21] J. Danziger, J. P. Dodelet, N. R. Armstrong, Chem. Mater. **3**, 812 (1991).

[22] Z.-S. Wang, C.-H. Huang, F.-Y. Li, S.-F. Weng, K. Ibrahim, F.-Q. Liu, J. Phys. Chem. B **105**, 4250 (2001).

Appendix B: Joseph W. Richards Fellowship Final Report

Interfaces between Organic Semiconductor Materials and Metal Electrodes

A final report submitted to the Electrochemical Society in completion of fellowship requirements

Published: C.B. France and B.A. Parkinson, Interface, **4**, 64, (2002)

Interesting structural organization of organic semiconducting compounds on metal electrodes could influence the electrical properties of new technologically significant devices. We have been investigating the molecular ordering of small molecule organics on Ag(111) and Au(111) films deposited on mica substrates.[*1*] These metal substrates are prepared in ultra-high vacuum (UHV) and used to simulate a contacting electrode. The metal substrates were prepared with Ar ion sputtering and annealed to produce pristine, terraced surfaces. The molecular semiconductors pentacene and *p*-sexiphenyl (p-6P) have been evaporated onto the metal film in UHV then analyzed

with a UHV scanning tunneling microscope (STM), temperature programmed desorption (TPD) and photoemission techniques.

The interface between Au(111) and pentacene has proved to be more interesting than anticipated, exhibiting a surprisingly large number of coverage dependant ordered structures.[2-4] Low coverages produced 4 polymorphs, while monolayer films produced 4 different row structures. Multilayer pentacene films generated a unique widely spaced periodic row structure, with a 61 ± 5 Å spacing. Ultraviolet photoemission spectroscopy has also been used to determine the energy level alignment of the pentacene and Au(111) interface.[5] A large interface dipole barrier (0.95 eV) was formed at this heterojunction interface. Two different binding environments for pentacene on Au(111) have been determined utilizing TPD. Monolayer or thinner films show a strong interaction with the Au substrate while thicker films have a smaller binding energy as the pentacene interactions are not dominated by the interface with the Au(111).

Investigations of p-6P on Au(111) have also provided useful insights into the organic semiconductor/metal interface. Similar to previous reports, photoemission spectroscopy revealed that the Au(111)/p-6P interface has a substantial (0.73 eV) interface dipole.[6] TPD of thick p-6P films (50Å) revealed the presence of at least two different binding environments. In Figure B.1, peak A and B have desorption

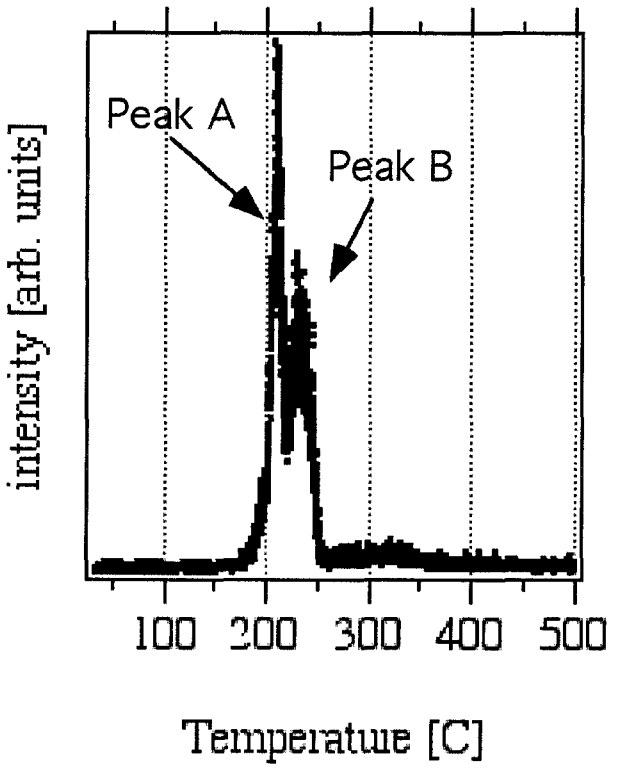

Figure B.1: Temperature programmed desorption of a 50Å *p*-sexiphenyl film on Au(111), heating rate of 15 C/min. Peak A with a peak temperature of 211.2C (136.4 KJ/Mole) and peak B with a peak temperature of 234.6C (143.3 KJ/Mole).

temperatures of 211°C and 234°C correlating to a binding energy of 126 and 143 KJ/mole respectively. Scanning tunneling microscopy of near monolayer shows an alternating structure that is similar to the crystalline packing of this material[7], see STM image in Fig. B.2. The Au 23 × $\sqrt{3}$ reconstruction is observed through the p-6P film. A proposed model of this organic film is depicted in Fig. B.3, where the Au substrate atoms are represented as circles and the darker colored atoms show the locations of the elevated atoms in the Au reconstruction. Darker p-6P molecules represent molecules lying with their plane parallel with the substrate while lighter p-6P molecules are tilted upright. The measured and model unit cell distances agree within 1% deviation, 33.8 × 14.3Å and 32.5 × 14.4Å respectively.

In summary, the formation of a substantial interface dipole has been confirmed between Au(111) and p-6P. At least two different binding environments have been determined to exist utilizing TPD. Thin film investigations using STM have shown an interesting herringbone structure where each unit cell has one p-6P molecule lining flat on the Au(111) and another tilted on edge. Edge-to-face interactions are maximized in this film structure and are similar to bulk p-sexiphenyl.[7]

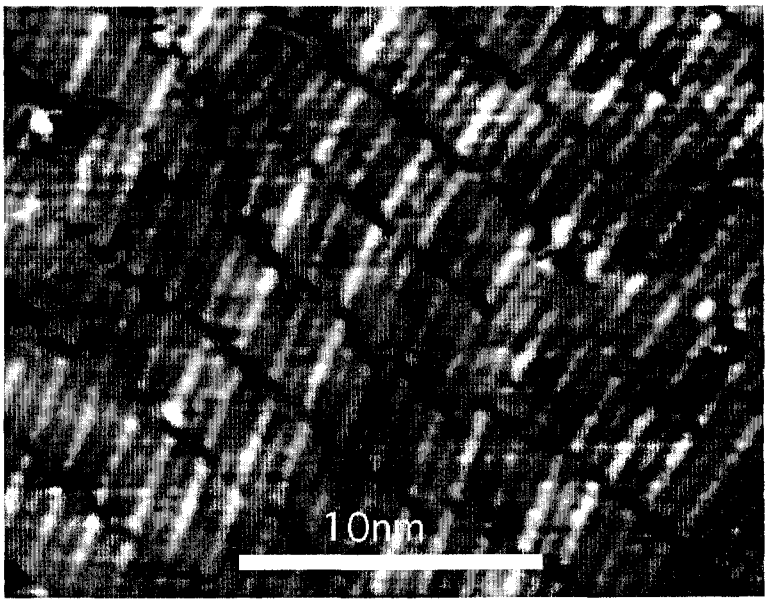

Figure B.2: A 25.4 × 19.7 nm STM image of p-6P on Au(111). The Au(111) reconstruction was imaged through the p-6P film and three elevated unit cells can be observed in the image. (-0.5 V sample bias, 0.1 nA, max z-height 0.105 nm)

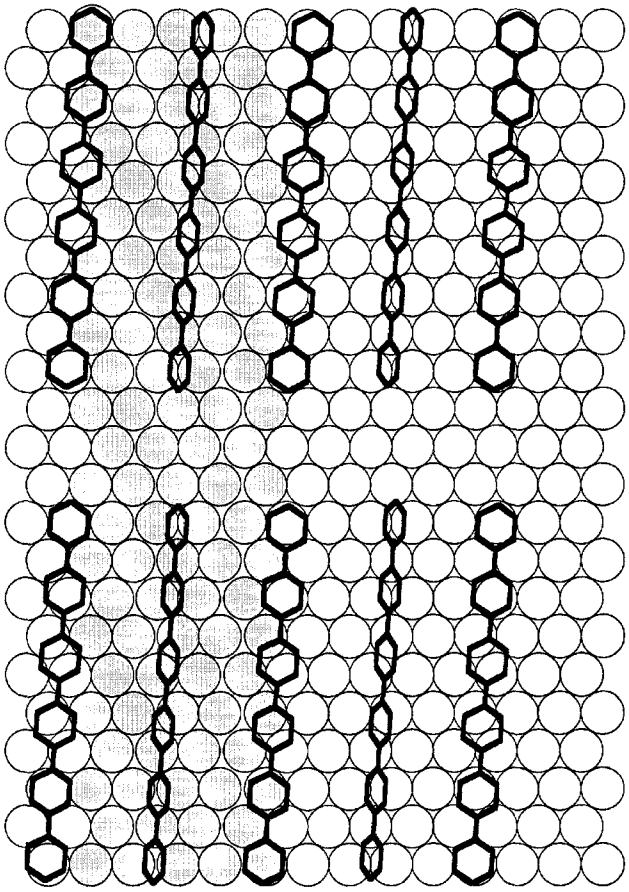

Figure B.3: A Proposed model of the p-6P film on Au(111). The Au dark substrate atoms represent the 23 × √3 reconstruction. The dark p-6P molecules signify molecules with their plane parallel to the substrate while lighter molecules represent tilted molecules.

References:

[1] S. Buchholz, H. Fuchs, J. Rabe, J. Vac. Sci. Technol. B **9**, 857 (1991).

[2] P. G. Schroeder, C. B. France, J. B. Park, B. A. Parkinson, J. Appl. Phys. **91**, 3010 (2002).

[3] C. B. France, P. G. Schroeder, B. A. Parkinson, Nano Lett. **2**, 693 (2002).

[4] C. B. France, P. G. Schroeder, J. C. Forsythe, B. A. Parkinson, Langmuir **19**, 1274 (2003).

[5] P. G. Schroeder, C. B. France, J. B. Park, B. A. Parkinson, J. Phys. Chem. B **107**, 2253 (2003).

[6] E. Ito, H. Oji, M. Furuta, H. Ishii, K. Oichi, Y. Ouchi, K. Seki, Synth. Met. **101**, 654 (1999).

[7] K. Baker, A. Fratini, T. Resch, H. Knachel, W. Adams, E. Socci, Polymer **34**, 1571 (1993).

Appendix C: Potential-Induced Transitions Research Proposal

A Systematic Investigation of Organic Adsorbates and their Potential-Induced Transitions at Electrically Biased Interfaces

A proposal submitted as a degree requirement for Chemistry Doctoral work at Colorado State University

C. Brian France
Department of Chemistry
Colorado State University
Fort Collins, Colorado 80523

Abstract

Organic molecules have shown complex adsorption behaviors on metal electrode surfaces. Sharp transitions between these adsorption states have been observed as a function of the electrode's applied potential. The existence of these potential induced phase transitions have been demonstrated with different organic adsorbates and metal electrodes including liquid-phase metals and single crystal noble metal surfaces. Previous research has demonstrated the existence of these transitions but no thorough investigations have been undertaken. We propose to systematically investigate these potential induced phase transitions through the careful selection of organic adsorbate molecules, metal electrode substrates, supporting electrolyte and pH. The objectives of this proposal include the identification of organic adsorbate/metal substrate systems that demonstrate this transition phenomenon and determine the potentials at which they take place. Structural analysis of the organic films before and after potential induced transitions will be achieved through the use of in situ scanning tunneling microscopy (STM) and atomic force microscopy (AFM). Dynamic investigations will be undertaken to determine the rate in which the phase transitions take place and to directly observe the transitions. This research will allow for the development of a fundamental set of rules governing potential induced phase transitions and provide new methodologies for the development of technological devices requiring ordered organic films. This inexpensive potential control of adsorbate ordering will have implications in new classes of electronic devices requiring molecular ordering.

Background and Significance

The design of molecular based technological devices such as transistors[1], switches and memories[2], sensors, biomimetic surfaces[3] and electronic interfaces[4] require the preparation and characterization of well-ordered monolayers and multilayers of organic molecules on solid substrates. The opportunity to control assemblies of organic molecules by utilizing potential-driven phase transitions/reorientations would facilitate and greatly simplify the development of new device technologies. Organic monolayers on electrified metallic substrates have demonstrated the propensity to undergo phase transitions induced by applying a potential to the substrate. These transitions in molecular ordering will lead to the dynamic control of macroscopic properties, from electronic conductivity, friction and surface wettability, to biocompatibility. Substrate potential induced transitions have been observed in several systems, however no thorough investigations have been undertaken to understand this phenomena. This proposed research is aimed at systematically investigating the ordering of organic adsorbates at electrified metallic interfaces. This effort will determine if there is a relationship between molecular structure and the substrate bias range allowing for a potential-induced order-disorder, reorientation and/or adsorption-desorption events. Molecular ordering of these phases, their film capacitance and rate of transition will be investigated as a function of substrate potential or charge density.

It has been reported that aqueous electrolyte with dissolved surfactants, in contact with mercury electrodes, can produce distinct adsorbed states at different substrate potentials.[5] These range from dilute films to dense compact layers, differing in molecular orientation and packing. Sharp transitions have been observed for a number of organic adsorbates on mercury electrodes, these interfacial processes or phase transitions have been associated with steps in the capacity-potential curves.[5] These "non-ideal" adsorption behaviors show sharp transitions between full coverage and complete desorption. Utilization of liquid metals like Hg, Ga or InGa, have the problem of non-covalent binding organic molecules interacting only through weak physisorption. Capacitance studies utilizing low melting point metals like Bi, Pb, Sn and Zn have produced similar results of weak interactions.[6] In an effort to increase interactions between organic and metal, platinum group elements were used in electrochemical investigations. These substrates are typically utilized as catalyst and adsorption of organics frequently resulted in irreversible chemisorption. Group IB metals (copper, silver and gold) allow for reversible adsorption and frequently interact with the character of weak chemisorption which involves the overlap of substrate metallic states with the molecular orbitals of the adsorbate.[6] An additional advantage of the group IB metals as substrates is the number of established methods for applying many complimentary scientific techniques for the investigation of organic monolayers.

As discussed above, surfactant molecules include some of the first organic adsorbates investigated on metal electrode surfaces. Discovery in this field continues and recent studies have moved from utilizing liquid metal electrodes toward gold single crystal surfaces. In addition to the increased adsorbate-substrate interaction, these substrates have the advantage of a well characterized and ordered surface which allows for structural characterization of the films on the electrode surface[7]. Burgess and coworkers have performed experiments using the surfactant dodedcyl sulfate, demonstrating that under electrochemical control, the adsorbate can be made to undergo a phase transition between a hemimicellar and condensed state.[8] (See table C.1 for structures of adsorbates described here and below.) These ionic surfactants were investigated with electrochemical capacitance measurements to identify the potential of the phase transition, then in situ scanning tunneling microscopy (STM) and atomic force microscopy (AFM) were used for the direct observation of the film ordering. Non-ionic surfactants, 4-pentadecylpyridine, have had potential-controlled transitions observed with infrared spectroscopy.[9] The potential driven phase transition between hemimicellar and condensed state was again observed. In addition, molecules that "desorbed," were found to form molecular aggregates in the vicinity of the electrode surface. The use of chemically bound ionic surfactant molecules and gold electrodes have recently demonstrated the ability to reversibly switch between a hydrophobic and a hydrophilic

surface.[10] Switching was achieved through conformational changes in the surfactant molecules. Potential-dependent adsorption-desorption and reorientation of dendritic polymers has also been demonstrated at electrified interfaces.[11] A second generation 4-pyridyl modified poly(amidoamine) (PAMAM) dendrimer was used to show a potential dependent dynamic adsorption state change including partial desorption and reorientation.

The first small molecule organics found to exhibit complicated adsorption on noble metal single crystal electrodes with potential induced phase transitions were DNA bases and other similar molecules capable of intermolecular hydrogen bonding. The initial investigation into the self-assembly of these DNA bases utilized primarily electrochemical and, to some extent, in situ STM techniques.[12] Molecular ordering in these systems was initially observed on the electrode surface. Later experiments including studies performed on cytosine[13], thymine[14], and guanine[15], all demonstrated that potential induced phase transitions were taking place. A small amount of structural characterization of these phases was obtained with in situ AFM and STM. Other small organic molecules demonstrated complex multi-phase adsorption on electrode surfaces. These systems included coumarin on Au(111) and Au(100)-(hex)[16] and uridine on Au(111)[17]. Elaborate investigations of uracil adsorption on Au(111) and Ag(111) with studies determining phase transition kinetics[18] and in-depth

electrochemical[19] parameters were performed, while minimal structural determinations were undertaken[20].

One of the more interesting and well studied potential induced transitions is that of 2,2'-bipryidine (22BPY) on Au(111). After investigating pyridine, 22BPY was first studied on Au(111) in electrochemical experiments by Yang and co-workers in 1994[21]. A multi-state adsorption was determined through electrochemical capacitance-potential curves. Second harmonic generation (SHG) spectroscopy was utilized to show that when the interface is negatively charged, the 22BPY molecule assume a flat orientation where the plane of the molecule is parallel with the gold surface. When the potential is positive the molecule assumes a vertical orientation where the two nitrogen atoms face the metal substrate. Further investigation into this model system by Cunha and Tao, utilized STM to directly observe the 22BPY molecules and their transitions on the electrode surface.[22] Molecules (22BPY) were found to be randomly oriented at, positive, low charge densities but began to align as the charge increased to a critical value. Chains of vertically oriented molecules were observed on the surface and described as "a roll of coins." Dynamic experiments were also performed where the surface charge density was changed during an STM experiment and the transition from a disordered to ordered film and back again was observed. This disorder to order transition was observed at a gold substrate potential of –0.1V vs SCE (0 $\mu C/cm^2$) to 0.14V (13.0$\mu C/cm^2$). Further

information was also obtained from this system by Dretschkow and coworkers[23], electrochemical capacitance-potential data was taken of 22BPY on Au(111) in both neutral and acidic solutions. Neutral conditions provided similar results to those already discussed, however, under acidic conditions an entirely new structure was observed at negative potentials while one of the nitrogen atoms was protonated and the second was not. Dynamic in situ STM investigations monitored the 22BPY in acidic solutions while sweeping the substrate potential from negative charge densities, through a region with no observed molecular order, to an ordered positive charge density structure. Desorption potentials under acidic conditions were also determined by direct observation of the film at high positive charge densities, showing the film persisted at higher than anticipated biases.

Recent interest in potential induced transitions by the Bourguet group at University of Pittsburgh has examined simple alkanes and porphyrin assembles on Au(111). Large hexadecane molecules were found to undergo a reversible order-disorder transition at both positive and negative charge densities.[24] The transitions were observed utilizing in situ STM. The transition is not believed to be caused by the removal of alkane molecules but rather, through incorporation of aqueous ions into the organic film preventing stable imaging of the organic species. In another study, a potential induced variation in the binding energy was observed for the large aromatic

molecule tetra-pyridyl porphine.[25] Films with varying degrees of order could be produced through the potential control of the substrate. Low coverage films showed molecules sticking to the Au(111) substrate without order and were immobile. The application of a positive potential reduced the binding energy of the prophyrin molecules to the surface, and allowed for an "annealing" effect were the molecules could reorient to form an ordered structure. When a more negative potential was applied, the films binding energy to the substrate was increased and the organic film formed a stable ordered structure. This report in particular demonstrates the need to obtain a fundamental understanding of these transitions because previous reports indicated that an ordered porphyrin film could not be achieved on Au(111). Prior to this study, ordered porphyrin films could only be obtained on a gold surface pacified with an iodine monolayer.[26-28]

While all of these studies are of fundamental importance in that they demonstrate that potential induced phase transitions are a more common event than anticipated, they fail to provide a thorough understanding of the phenomena. The objective of this proposed research is to establish a fundamental set of rules that relate the structural properties of the adsorbate molecules and the surface states of the metal substrate to the potential induced phase transitions of these systems. Experimental determination of the adsorbate phase transition potentials through the systematic variation of the organic adsorbate molecules, electrolyte, pH and electrode surface properties (both the metallic

Table C.1 Molecules Demonstrating Phase Transitions on Electrified Substrates

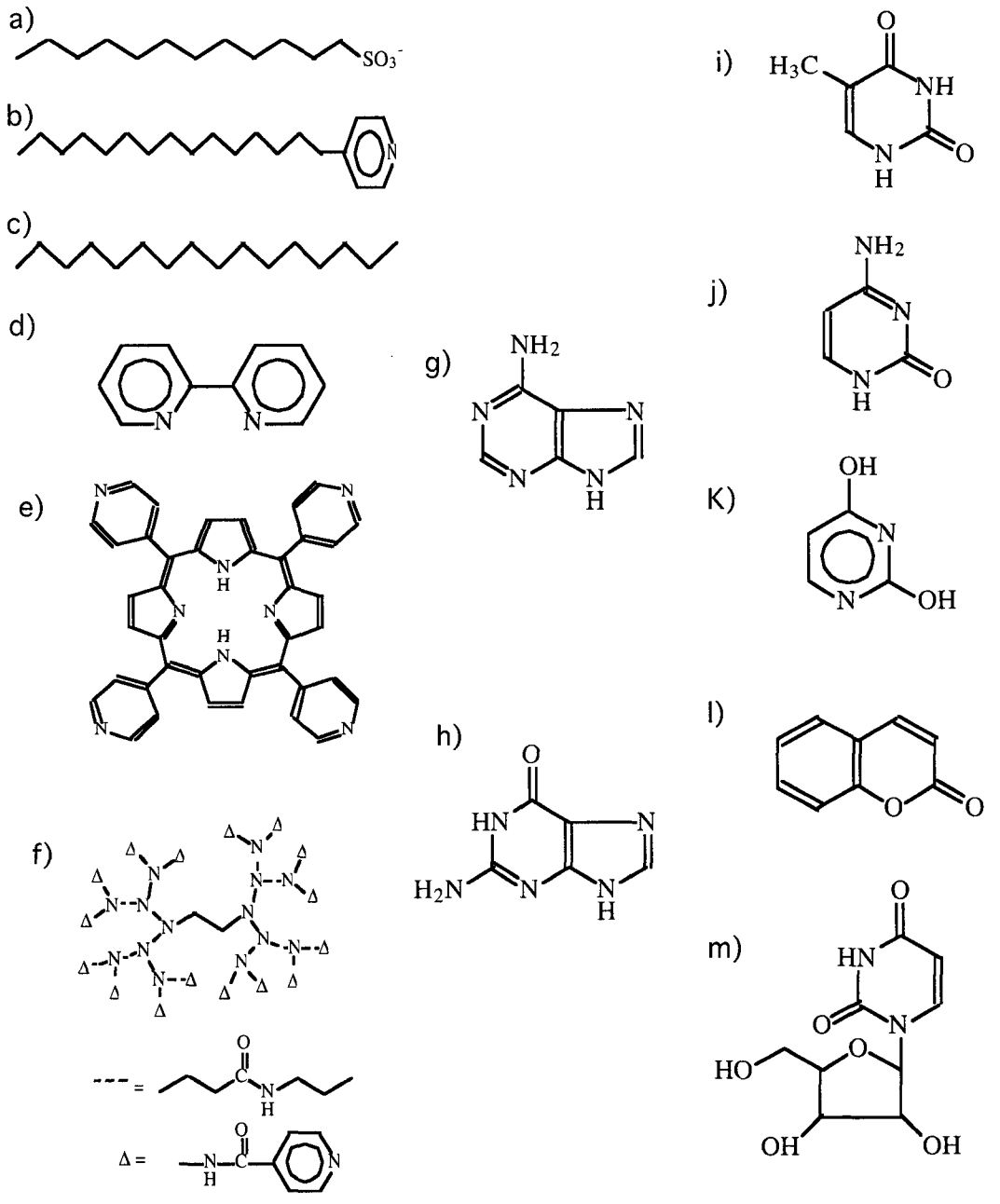

a) dodecyl sulfate (SDS) b) 4-pentadecylpyridine c)hexadecane d)2,2'-bipyridine e) 5,10,15,20-tetra(4-pyridyl)-21H,23H-porphine (TPyp) f)4-pyridyl modified PAMAM G2 dendrimer g) adenine h) guanine i) thymine j) cytosine k) uracil l) coumarin m) uridine

make up and crystallographic orientation) will allow us to establish these rules and predict molecular ordering and transition potentials. These rules would be invaluable toward designing molecular systems with applications in molecular switching, nanotechnology, and biocompatible materials.

Research Design:

The vast majority of the potential induced phase transitions that have been discussed in the background information consist of an ordering or rearrangement of the organic film as the electrode potential is changed. Utilizing a series of systematically altered organic adsorbates comprised of varying amounts of aromatic, aliphatic, ionic and heteroatom make up will be used to determine the fundamental rules of potential induced phase transitions. Determination of phase transition potentials in relation to molecular functional groups will allow for the prediction of transition potentials and eventually to the design of molecules having a desired transition at a predetermined potential. Electrochemical experiments will provide information about the potentials at which these phase transitions take place and the rate at which they are happening. In situ scanning probe microscopy will be performed to determine the molecular ordering of the organic film. Both complimentary techniques, Atomic Force Microscopy (AFM) and Scanning Tunneling Microscopy (STM) will be utilized. All of these techniques can be utilized in-

Table C.2 Preliminary Organic Model Systems

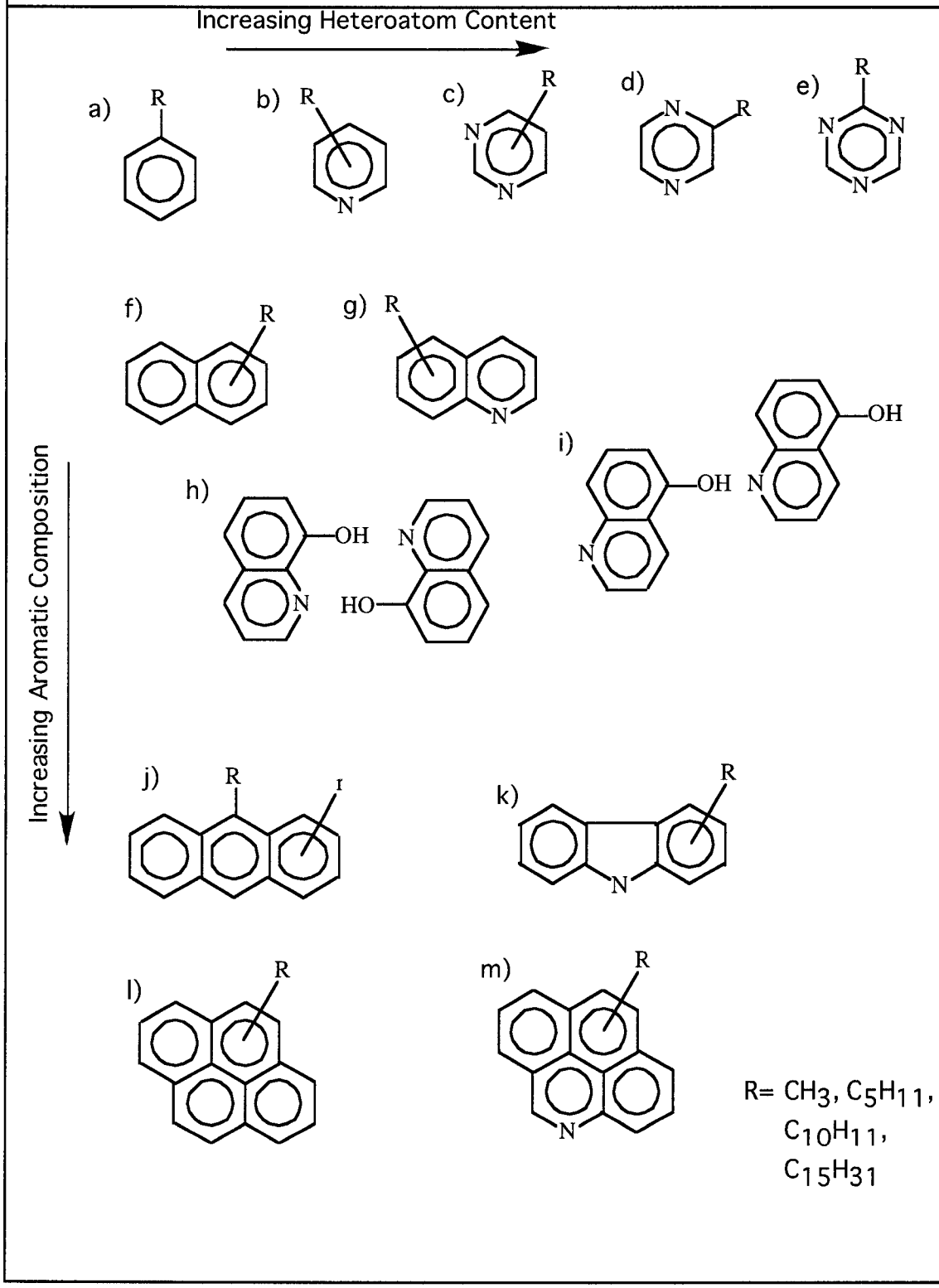

situ, allowing for in-depth, dynamic analysis of these systems: which will provide unprecedented understanding of the potential induced phenomena.

Table C.2 shows a few of the organic adsorbate systems that we propose to investigate. This table is not an all-exclusive list but provides an initial collection of interesting molecules that have similarities to previously studied systems that, we believe, should guarantee the presence of potential induced transitions. Table C.2 is presented in a fashion that from the upper left corner, molecules to the right have an increasing amount of heteroatom content while molecules below have an increasing aromatic composition. In initial experiments, the "R" functional group represents an aliphatic chain as designated in the lower right of table C.2. These chains will allow for the determination of how alkane chain length can effect the potential induced transitions while maintaining constant aromatic and heteroatom content. Increase of the aromatic size of the molecules will show how changes in polarizability effect the transitions. Molecular weight, boiling and melting points of these systems will also be analyzed to determine if any relation to the transition potentials exists. Future experiments will change the "R" group from a simple alkane to allow for the investigation of other phase transition altering functional groups. Ionic groups will determine how the existence of charge on the molecule affects transition potentials. Electron withdrawing and donating groups will show how dipole moments effect the transitions. Some of these systems will also incorporate functional

groups that will allow hydrogen bonding to exist between molecules. This increased interaction between molecules can be adjusted in such a way that many molecules can be hydrogen bonded together (table C.2 h) or just two (table C.2 i). These slight changes in molecular make up will allow for a fundamental set of rules to be developed by way of understanding the relationships between potential of transition and molecular structure. These rules will then be used to not only control the potential at which the transition takes place but the structure of the film itself.

The first objective of this proposed research will be to determine electrochemically, the potential at which these phase transitions take place. The transition potentials can be determined by observing how the electrode/film capacitance changes as a function of applied potential. These types of measurements can provide not only the potential at which a transition takes place but generate an estimate of the organic film coverage (i.e. a diffuse or compact film). During these experiments, differences in transition potentials as a result of changing metal substrate (composition and crystallographic orientation) and molecular make up will be investigated. These changes can be made quickly allowing for interesting trends to be observed and investigated in further detail.

Once phase transition potentials are determined, the second objective of structural analysis utilizing in-situ STM and AFM will be performed. Images of the ordered

surface adsorbates with molecular resolution will be obtained. Both techniques are capable of molecular resolution of the adsorbates but STM in particular has demonstrated spectacular resolution of in-situ systems in recent years[29-32]. The STM images are a convolution of both electronic and height effects. This is caused by the fact that electrons tunnel through the surface adsorbates between the tip and substrate, while the current of this process is monitored to provide the image. Facile tunneling through molecular orbitals or highly conductive adsorbate structures result in increased current through these areas and are imaged as a height increase and can be misinterpreted as such. We suspect that variations in the electronic energy levels of the adsorbate are quite possible while altering the potential of the substrate and thus the way the adsorbate and substrate interact. Atomic force microscopy is not susceptible to these electronic effects and will provide "true" height information albeit at a lower resolution than STM. Thus, when an electronic effect is suspected utilizing STM, AFM will be used to confirm the true topographic effects. If an electronic effect is determined, molecular orbital calculations will be utilized to provide additional insight into the nature of the electronic effect and thus the interaction between the adsorbate and substrate as well as adsorbate-adsorbate interactions. These calculations have been previously used to interpret images generated by STM through the determination of the molecular orbitals providing the most probable paths for electron tunneling[33].

The final objective will be the determination of the rates and dynamic observation of the potential induced phase transitions. During the structural analysis, dynamic investigations will be undertaken. Imaging the system while changing the potential of the substrate to induce a phase transition will allow molecules to be observed while rearranging into their new orientations. This will provide unequivocal proof of the transition and the potentials at which they take place. Rate constants of the event will likely not be determined with this experiment as AFM and STM techniques produce images on the time scale of minutes, they are not well suited for used in kinetic measurements. Current transients produced by stepping the potential from one state through the transition into another will provide more accurate kinetic information. This dynamic piece of understanding about the system will allow for fundamental rules of potential induced phase transitions to be determined, allowing for predictions of transition potentials, structures formed and the rates of change to be achieved.

Our hypothesis to obtaining a way to control the potentials at which phase transitions take place involves the interaction of the molecules with one another and the substrate. We believe that to obtain an ordered phase that can withstand a large potential difference, without desorbing or other changes, the interactions between the adsorbates or the adsorbates with the substrate must be strong. The determination of which is more important will be revealed during this proposed research, we believe both interactions

will play an important roll. The heteratoms with lone pair electrons (nitrogen containing compounds in table C.2) should increase the interaction with the metal substrate. While hydrophobic and van der Waals interactions of longer alkane chains will increase the adsorbate-adsorbate interactions and prevent them from being removed from the metallic surface. Predictions of the structural changes of phase transitions are out of the scope of current scientific knowledge as too few experiments have been performed in the field of dynamic phase transition structural analysis. This proposed work is a pioneering effort and demonstrates its importance.

Initial experiments will begin using gold metallic substrates with the (111) crystallographic surface. Extensive use of this substrate in the literature demonstrates the ease with which the substrate can be prepared, known crystallographic structure and structural changes that take place with applied potential. Future experiments will utilize other metallic electrodes with different compositions and crystallographic orientations. The procedures to produce many other metallic substrates are widely available in the literature and referees herein. The electrolyte solution will initially be a purified water solution with $KClO_4$ or $NaClO_4$, deaerated by bubbling nitrogen to remove any oxygen. The choice of this electrolyte was made because the ions have minimal interaction with the metal substrate. This fact will be very important in these experiments were we believe the interaction with the adsorbate and substrate will be critical. Simply using

purified water may also be an option in some experiments as long as no current is allowed to flow. The pH in these initial experiments will be approximately 7 but as described above, the electrolyte solutions will not be buffered. Later experiments will utilize pH as a variable to allow for the protonation of heteroatoms that are present on the aromatic rings (see table C.2). The protonation of heteroatoms will decrease the electron density available for the molecules to interact with the metal and thus decrease the interaction between the metal and organics. The presence of the positive charge on the molecule will also effect the potential at which transitions take place.

The organic adsorbates that will be initially investigated are those that are readily and commercially available. These include some a), b), g), h), i), k), j) and k) molecules from table C.2. The benzene systems will be a good calibration system as its structure has previously been identified.[32] The phenyl alkanes will then be investigated to look at how the increasing interaction between adsorbates, through alkane chains, effects any observed potential phase transitions. Systems with increasing amounts of aromatic and heteroatom content will then be undertaken. The experiments will be performed following the objectives outlined above.

This proposed research can reveal many fundamental principles concerning potential induced phase transitions. The development of a fundamental set of rules will provide the ability to predict the potential of phase transition of a designed molecule, the

structure it will form and the rate at which the change will take place. The thorough understanding of this phenomenon will lead to new methods of producing organic films with desired orientations by way of the application of a simple electrical potential.

References:

[1] Cassagneau, T., J. H. Fendler and T. Mallouk "Optical and electrical characterizations of ultrathin films self-assembled from 11-aminoundecanoic acid capped TiO_2 nanoparticles and polyallylamine hydrochloride", *Langmuir,* **16**, 241 (2000).

[2] Wong, E. W., C. P. Collier, M. Behloradsky, F. Raymo, J. F. Stoddart and J. R. Heath "Fabrication and transport properties of single-molecule-thick electrochemical junctions", *J. Am. Chem. Soc.,* **122**, 5831 (2000).

[3] G. Roberts Langmuir-Blodgett Films. New York, Plenum Press (1990).

[4] Baldo, M. A. and S. R. Forrest "Interface-limited injection in amorphous organic semiconductors", *Phys. Rev. B,* **64**, 85201 (2001).

[5] Buess-Herman, C. (1992). Dynamics of adsorption and two-dimensional phase transitions at electrode surfaces. Adsorption of molecules at metal electrodes. J. Lipkowski and P. Ross. New York, VCH publishers, Inc.: 77.

[6] Lipkowski, J. and L. Stolberg (1992). Molecular adsorption at gold and silver electrodes. Adsorption of molecules at metal electrodes. J. Lipkowski and P. Ross. New York, VCH Pulbishers, Inc.: 171.

[7] Aloisi, G., M. Cavallini and R. Guidelli (1998). Surface structure and electrochemistry: new insight by scanning tunneling microscopy. Electrochemical Nanotechnology. W. J. Lorenz and W. Plieth. Weihneim, Wiley-VCH: 101.

[8] Burgess, I., C. A. Jeffrey, X. Cai, G. Szymanski, Z. Galus and J. Lipkowski "Direct visualization of the potential-controlled transformation of hemimicellar aggregates of dodecyl sulfate into a condensed monolayer at the Au(111) electrode surface", *Langmuir,* **15**, 2607 (1999).

[9] Zamlynny, V., I. Zawisza and J. Lipkowski "PM FTIRRAS studies of potential-controlled transformations of a monolayer and a bilayer of 4-pentadecylpyridine, a model surfactant, adsorbed on a Au(111) electrode surface", *Langmuir,* **19**, 132 (2003).

[10] Lahann, J., S. Mitragotri, T.-N. Tran, H. Kaido, J. Sundaram, I. Choi, S. Hoffer, G. A. Somorjai and R. Langer "A reversibly switching surface", *Science,* **299**, 371 (2003).

[11] Sagara, T., K. Nagata, H. Tsuruta and N. Nakashima "Dynamic dendrimer at electrified interface: potential dependent adsorption-desorption and reorientation of a 4-pyridyl-modified PAMAM dentrimer", *Chem. Commun.*, 2116 (2002).

[12] Tao, N. J., J. A. DeRose and S. M. Lindsay "Self-assembly of molecular superstructures studies by in situ scanning tunneleing microscopy:DNA bases on Au(111)", *J. Phys. Chem.*, **97**, 910 (1993).

[13] Wandlowski, T., D. Lampner and S. M. Lindsay "Structure and stability of cytosine adlayers on Au(111): an in-situ STM study", *J. Electroanal. Chem.*, **404**, 215 (1996).

[14] Hölzle, M. H., D. Krznaric and D. M. Kolb "Phase transitions in thymine adlayers on silver single crystal elctrodes", *J. Electroanal. Chem.*, **386**, 235 (1995).

[15] Tao, N. J. and Z. Shi "Monolayer guanine and adenine on graphite in NaCl solution: A comparative STM and AFM study", *J. Phys. Chem.*, **98**, 1464 (1994).

[16] Hölzle, M. H. and D. M. Kolb "Two-dimensional phase transitions in electrochemically formed adlayers on gold", *Ber. Bunseges. Phys. Chem.*, **98**, 330 (1994).

[17] Scharfe, M., A. Hamelin and C. Buess-Herman "On the occurrence of two-dimensional phase transitions of uridine at the aqueous solution-gold single crystal interface", *Electrochima Acta.*, **40**, 61 (1995).

[18] Guidelli, R., M. L. Foresti and M. Innocenti "Two-dimensional phase transitions of chemisorbed uracil on Ag(111): modeling of short- and long-time behavior", *J. Phys. Chem.*, **100**, 18491 (1996).

[19] Wandlowski, T. "Phase transitions in uracil adlayers on Ag, Au and Hg electrodes - substrate effects", *J. Electroanal. Chem.*, **395**, 83 (1995).

[20] Hölzle, M. H., T. Wandlowski and D. M. Kolb "Structural transitions in uracil adlayers on gold single crystal electrodes", *Surf. Sci.*, **335**, 281 (1995).

[21] Yang, D., D. Bizzotto, J. Lipkowski, B. Pettinger and S. Mirwald "Electrochemical and second harmonic generation studies of 2,2'-bipyridine adsorption at the Au(111) electrode surface", *J. Phys. Chem.*, **98**, 7083 (1994).

[22] Cunha, F. and N. J. Tao "Surface charge induced order-disorder transition in an organic monolayer", *Phys. Rev. Lett.*, **75**, 2376 (1995).

[23] Dretschkow, T., D. Lampner and T. Wandlowski "Structural transitions in 2,2'-bipyridine adlayers on Au(111)- an in-situ STM study", *J. Electroanal. Chem.*, **458**, 121 (1998).

[24] He, Y., T. Ye and E. Borguet "The role of hydroohobic chanins in self-assembly at electrified interfaces: observation of potential induced transformations of two-dimensional crystals of hexadecane by in-situ scanning tunneling microscopy", *J. Phys. Chem. B*, **106**, 11264 (2002).

[25] He, Y., T. Ye and E. Borguet "Prophyrin self-assembly at electrochemical interfaces: role of potential modulated surface mobility", *J. Am. Chem. Soc.*, **124**, 11964 (2002).

[26] Kunitake, M., N. Batina and K. Itaya "Self-oranized porphyrin array on iodine-modified Au(111) in electrolyte solutions: In situ scanning tunneling microscopy study", *Langmuir,* **11**, 2337 (1995).

[27] Ogaki, K., N. Batina, M. Kunitake and K. Itaya "In situ scanning tunneling microscopy of ordering processes of adsorbed porphyrin on iodine-modified Ag(111)", *J. Phys. Chem.,* **100**, 7185 (1996).

[28] Kunitake, M., U. Akiba, N. Batina and K. Itaya "Structures and dynamic formation processes of prophyrin adlayers on iodine-modified Au(111) in solution: in situ STM study", *Langmuir,* **13**, 1607 (1997).

[29] Shimooka, T., S. Yoshimoto, M. Wakisaka, J. Inukai and K. Itaya "Highly ordered anthracene adlayers on Ag single-crystal surfaces in perchloric acid solutions: In Situ STM study", *Langmuir,* **17**, 6380 (2001).

[30] Gewirth, A. and B. Niece "Electrochemical applications of *in situ* scanning probe microscopy", *Chem. Rev.,* **97**, 1129 (1997).

[31] Yau, S.-L., Y.-G. Kim and K. Itaya "High-resolution imaging of aromatic molecules adsorbed on Rh(111) and Pt(111) in hydrofluoric acid solution: In Situ STM study", *J. Phys. Chem. B,* **101**, 3547 (1997).

[32] Wan, L.-J. and K. Itaya "In Situ scanning tunneleing microscopy of benzene, naphthalene, and anthracene adsorbed on Cu(111) in solution", *Langmuir,* **13**, 7173 (1997).

[33] Forrest, S. R. "Ultrathin organic films grown by organic molecular beam deposition and related techniques", *Chem. Rev.,* **97**, 1793 (1997).